The Dissertation Committee for Brian Christopher Carroll certifies that this is the approved version of the following dissertation:

Droplet Generation and Mixing in Confined Gaseous Microflows

Committee:

_____
Carlos Hidrovo, Supervisor

_____
Roger Bonnecaze

_____
Alexandre da Silva

_____
Robert Moser

_____
Li Shi

Droplet Generation and Mixing in

Confined Gaseous Microflows

by

Brian Christopher Carroll, B.S.M.E.; M.S.E.

Dissertation

Presented to the Faculty of the Graduate School of

The University of Texas at Austin

in Partial Fulfillment

of the Requirements

for the Degree of

Doctor of Philosophy

The University of Texas at Austin

December 2012

We have a habit in writing articles published in scientific journals to make the work as finished as possible, to cover up all the tracks, to not worry about the blind alleys or describe how you had the wrong idea first, and so on. So there is not any place to publish, in a dignified manner, what you actually did in order to get to do the work.

Richard Feynman, Nobel Lecture, December 11, 1965

PREFACE

My initial objective, naïve in its origin and ambitious in its breadth, was to solve with absolute completeness many of the complex problems facing gas-liquid microfluidics. Although significant accomplishments were made, there are now more unanswered questions today than when I began four years ago. A complete understanding of two-phase microflows did not transpire, but this work does answer the most critical and decisive questions. The seemingly impossible task of creating individual micro-droplets of liquid, colliding two together at high speed, and doing it all in a simple 2D microfluidic chip using a high speed gas flow has been accomplished. Previously unobservable droplet mixing dynamics have been captured using a novel arrangement of high repetition lasers, spectral filtering optics, differential fluorescence, wide-field microscopy, high speed image acquisition, custom image processing, and specifically tailored statistical analysis. The 1μm spatial and 25μs temporal resolution afforded by this optical diagnostic system is unsurpassed. The stability and flow control of the newly developed microfluidic test bed has led to gas-liquid droplet generation rates and mono-dispersed size distributions never before achieved in a confined microchannel. This work has opened the door into the new possibilities that two-phase microfluidics offers, from both a fundamental research and commercial applications perspective. I am proud to have taken part in this work and forever grateful to my advisor for giving me this opportunity.

Droplet Generation and Mixing in Confined Gaseous Microflows

Brian Christopher Carroll, Ph.D.

The University of Texas at Austin, 2012

Supervisor: Carlos Hidrovo

Fast mixing remains a major challenge in droplet-based microfluidics. The low Reynolds number operating regime typical of most microfluidic devices signify laminar and orderly flows that are devoid of any inertial characteristics. To increase mixing rates in droplet-based devices, a novel technique is presented that uses a high Reynolds number gaseous phase for droplet generation and transport and promotes mixing through binary droplet collisions at velocities near 1m/s. Control of multiple gas and liquid streams is provided by a newly constructed microfluidic test bed that affords the stringent flow stability required for generating liquid droplets in gaseous flows. The result is droplet production with size dispersion and generation frequencies not previously achievable. Limitations of existing mixing diagnostic methods have led to the development of a new measurement technique for measuring droplet collision mixing in confined microchannels. The technique employs single fluorophore laser-induced fluorescence, custom image processing, and meaningful statistical analysis for monitoring and quantifying mixing in high-speed droplet collisions. Mixing information is revealed through three governing statistics that that separate the roles of convective rearrangement and molecular diffusion during the mixing process. The end result is a viewing window into the rich dynamics of droplet collisions with spatial and temporal resolutions of 1μm and 25μs, respectively. Experimental results obtained across a decade

of Reynolds and Peclet numbers reveal a direct link between droplet mixing time and the collision convective timescale. Increasing the collision velocity or reducing the collision length scale is the most direct method for increasing droplet mixing rates. These characteristics are complemented by detaching droplets under inertial conditions, where increasing the Reynolds number of the continuous gaseous phase generates and transports smaller droplets at faster rates. This work provides valuable insight into the emerging field of two-phase gas-liquid microfluidics and opens the door to fundamental research possibilities not offered by traditional oil-based architectures.

TABLE OF CONTENTS

CHAPTER 1

INTRODUCTION

The electronic miniaturization of the past decades is mirrored by recent trends in fluidic applications, where miniaturization and integration of multiple laboratory processes and functions is performed on a fluidic chip not much larger than today's computer processers. Stimulated by new materials and fabrication methods, the field of microfluidics is rapidly maturing and offers new opportunities for technical innovation and academic research. Microfluidics is a multidisciplinary science that addresses the behavior, control, and manipulation of fluids (both liquids and gases) that are geometrically constrained to the micron and sub-micron scale and employs fluid volumes that are often difficult to detect by the naked eye. The first microfluidic device was demonstrated 30 years ago by researchers at Stanford University (Tuckerman and Pease 1981) as a potential option for point source heat rejection. The first commercially successful microfluidic application is the ink jet printer that quietly resides on our home and office desks.

Ink jet printing is only a precursor to the overarching use of microfluidics. It is truly diverse in every respect, with applications ranging from microelectronic thermal management (Tuckerman and Pease 1981), environmental toxicity monitoring (Piorek et al.), DNA sequencing (Robinson et al. 2010), pharmaceutical drug testing (Brouzes et al. 2009), and materials processing (Gradl and Peukert 2010). Application development has largely been facilitated by technological advancements in optical and other detection technologies, enabling researchers to probe device functionalities with unprecedented accuracy, precision, and sensitivity. In this respect, microfluidics has emerged as a truly interdisciplinary science. The ability to miniaturize an entire laboratory has spawned nomenclature such as Lab-on-a-Chip (*LOC*) and Micro Total Analysis Systems (μTAS) that intend to capture the scaling down of multiple processes to a chip-like format. Like

any developing technology, there are many questions that remain unanswered, issues that remain unresolved, and many possibilities that remain undiscovered.

1.1 Droplet Microfluidics

Microfluidics is most readily differentiated between continuous flow and droplet-based applications. Continuous flow devices operate using two or more liquid streams that can be miscible, for mixing, or immiscible, for laminations. Droplet microfluidics, on the other hand, uses discrete liquid volumes that are generated and transported by a continuous phase fluid. This division of fluids into independently controlled and discrete packets for manipulation provides many advantages over continuous flow systems. Microfluidic processes are reduced to a set of basic discrete operations, which allows for a hierarchical and cell-based design approach to be used. Applications such as point-of-care medical diagnostics, on-chip DNA analysis, automated drug delivery, and protein crystallization has solidified droplet microfluidics as an essential laboratory tool.

1.2 Device Throughput

The majority of microfluidic devices in service today utilize an oil-based continuous phase and an aqueous dispersed phase (droplets). The continuous phase is responsible for the generation, encapsulation, and transport of droplets. It serves as a conveyor belt, continuously moving droplets throughout the device. Device throughput, meaning the volumetric rate at which droplets enter and leave the system, is determined by droplet volume and generation rate and is related to how fast this conveyor belt is moving. When soft lithography fabrication techniques are used, the speed of the conveyor belt is limited by the pressure resolve of the device. Using a lower viscosity continuous phase fluid could greatly increase device throughput, reduce energy consumption, accelerate system processing times, and simplify manufacturing processes.

1.3 Gas-Liquid Droplet Generation

Prerequisite to orchestrating droplet collisions is the ability to create droplets from a continuous liquid supply. Generating predictable droplets in a gaseous microflow is significantly more difficult compared to oil-liquid systems. Broad size statistics is a salient and fundamental feature of liquid atomization where droplets can take an order of magnitude difference in diameter and generation rates show multiple frequency contents (Lefebvre and Chin 1985). The highly mono-disperse size statistics mandated by modern droplet-based devices requires substantial finesse and creativity. The problem is compounded even further when the continuous an discrete fluid phases have vastly different properties, such as air and water. The high velocity potential afforded by gaseous microflows increases the complexity even further and enriches the observed dynamics. Gas-liquid droplet flows in confined geometry are often described as unpredictable, unwieldy, and contamination prone. There are a number of applications, however, that necessitate fast mixing and high throughput capability while remaining relatively simple, cheap, passive, portable, and disposable. The ability to generate mono-dispersed droplets in a confined, gaseous microflow is therefore of significant academic and commercial importance.

1.4 Mixing at the Microscale

Mixing is an essential process in modern microfluidic systems and this seemingly simple task remains a major challenge when fast mixing is required. The topic is forefront at any microfluidics conference or periodical and complete books are devoted to the subject (Nguyen 2008). The ability to analyze non-equilibrium conditions and probe the kinetics of bio-molecular reactions has been limited by the speed at which mixing takes place. The low Reynolds (*Re*) numbers typical of most microfluidic operating regimes signify laminar and orderly flows that are devoid of any inertial characteristics. The turbulent flow regime exploited at the macroscale for fast mixing is difficult and impractical to implement, although turbulence has been achieved for continuous flow

microfluidic mixing devices (Takahashi et al. 1995). Many important structural events, such as nucleotide-flipping (Robinson, et al. 2010) and calmodulin (CaM) dynamics (Park et al. 2007) occur on timescales much less than a millisecond. The ability to probe and study these short-lived phenomena requires significant advances in droplet mixing.

The two most successful passive mixing techniques are hydrodynamic flow focusing and chaotic advection. Hydrodynamic flow focusing reduces the mixing length scale by geometric confinement and is only applicable to continuous flow devices. It represents a physical length scale reduction and the flow field remains orderly and laminar. As shown in Figure 1, two sheath fluids are used to controllably shear a sample stream to a desired width. The governing physics of this process are well understood and are easily modeled using a fluid resistance network (Zhang et al. 2008). Mixing times near 1μs have been achieved with focused widths near 50nm (Knight et al. 1998, Hertzog et al. 2004).

Chaotic advection is a termed first coined by Aref in his seminal paper (1984). His publication precipitated a new strategy for microscale mixing a decade later and the term is now common place amongst the microfluidic community. In contrast to hydrodynamic flow focusing, chaotic advection reduces the diffusion length scale by particle motions that, when viewed from a Lagrangian perspective, appear random and chaotic. Chaotic advection is achievable with both continuous flow (Stroock et al. 2002, Mao et al. 2010) and droplet based micromixers (Song et al. 2003, Song and Ismagilov 2003, Tice 2003, Song et al. 2006), as shown in Figure 1. For continuous flow mixers, geometric obstacles and channel texturing are used to facilitate chaotic motions in the flow that would otherwise be fully developed. Chaotic advection in segmented and droplet-based mixers is realized through a combination of channel geometry and localized interactions between the discrete and continuous phase and channel walls. These interactions produce rolling, stretching, and folding behaviors that continuously increase the miscible fluid's interface area, thereby reducing the length over which diffusion must occur. The process is analogous to the classic lid driven cavity problem where the flow field is perturbed by constant, periodic, or aperiodic forces occurring at interface boundaries. In fact, the lid

driven cavity represents a simple and well characterized system for understanding the otherwise complex flow field that results as droplets are transported inside microchannels (Wang et al. 2008). Although mixing times near 1ms have been achieved with chaotic advection (Mao, et al. 2010), the majority of demonstrations remain in the 100ms-1s range for nano-liter fluid volumes (Stroock, et al. 2002, Song, et al. 2003, Simonnet and Groisman 2005, Xia et al. 2005).

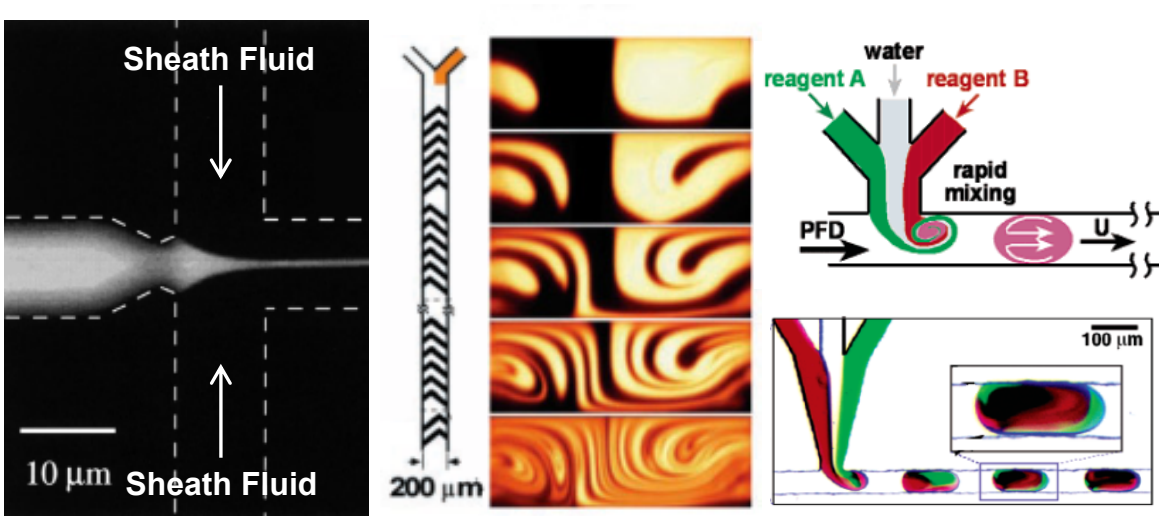

Figure 1. A hydrodynamic flow focusing device where sheath fluids are used to shear a sample stream to less than 1µm for mixing times less than 1µs (Knight, et al. 1998) (left). Chaotic advection mixing device using alternating herringbone channel texturing to promote random particle motions and increase mixing rates (Stroock, et al. 2002) (middle). Droplet-based chaotic advection device where the local droplet flow field is disturbed by shear forces at the oil-water interface (Song, et al. 2003) (right).

1.5 Collision-Based Mixing

Transporting droplets at high rates also complements a new inertial mixing technique. If two droplets are collided together in a controlled collision, the kinetic energy carried by each droplet is dissipated through viscous interactions. The flow field following the collision effectively stirs the droplet contents and provides conditions for diffusion to occur rapidly. Before the coalescence process can occur, however, the continuous phase

that surrounds each droplet must be displaced. This is an energy intensive process when the ambient phase is another liquid, particularly oil, where thin-film lubrication approximations apply. Draining this lubricating film takes time and delays the coalescence process (Jose and Cubaud 2012). Droplets colliding in air, however, coalesce upon contact within a given inertial range.

The design capitalizes on a rapid mixing technique presented by Simpson et al. where micro-droplets are collided in an unconfined, gaseous environment at high speed to yield mixing times near 200μs (1983, 1986). Referring to the simplified schematic in Figure 2, liquid droplets of *Solute 1* and *2* are detached and accelerated by a high speed gas flow from two opposing legs of a T-junction. Each droplet obtains kinetic energy KE_1 and KE_2 and surface energy SE_1 and SE_2. At the common junction, the droplets collide and coalesce. The kinetic and surface energy following collision is KE_3 and SE_3, each of which is less than the respective energy prior to collision. This abrupt change in kinetic and surface energy is viscously dissipated through complex velocity fields and bulk volumetric rearrangement. The result is near millisecond mixing for nanoliter sized droplets. Mixing through droplet collisions in a confined gaseous microflow is what distinguishes this method from other techniques in use today.

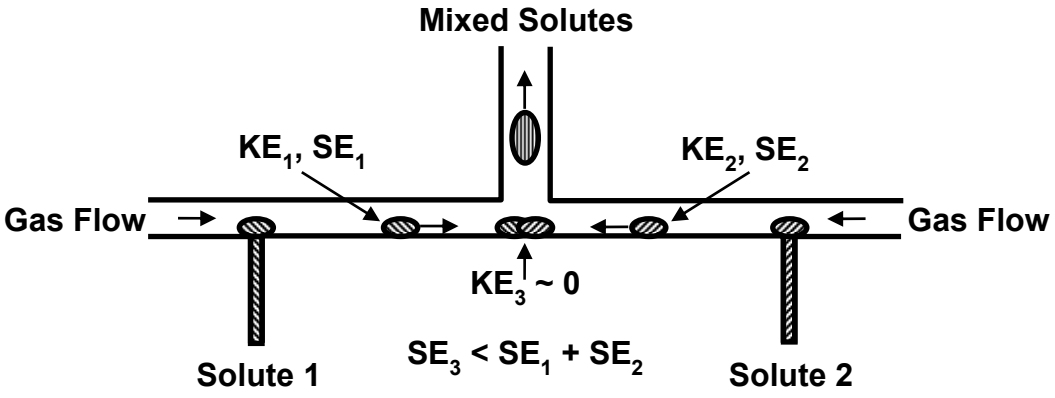

Figure 2. Shown above is a simplified schematic of an inertial mixing droplet collider. Two droplets with kinetic energy KE_1 and KE_2 and surface energy SE_1 and SE_2 collide at a channel junction. The kinetic energy following collision is essentially zero while the surface energy is about $2^{1/3}$ times less for equally sized spherical droplets. Droplet contents are quickly rearranged as the rapid decrease in kinetic and surface energy is viscously dissipated inside the droplet.

1.6 Dissertation Organization

This manuscript is organized in chapters that correspond to the major research efforts. Each section concludes with a summary that succinctly describe the research accomplishments. This work begins with the development of an inertial micromixer. A description of the microfluidic test bed used for gas-liquid droplet dynamics follows that describes on how the control and manipulation of nano-liter droplets is achieved from a hardware perspective. Device operation is described and performance predictions are made. Droplet generation using a gaseous microflow appears next and results show how droplet aspect ratio, volume, and generation rate are influenced over the range hydrodynamic conditions of practical importance. The optical diagnostic procedure for acquiring mixing information is described next, which includes a brief overview of fluorescent fundamentals. The development of a new set of spatial statistics is proposed that is specifically tailored for droplet mixing in highly inertial conditions. This work concludes with an experimental investigation of high speed droplet collision mixing. A number of cases are selected for in-depth discussion to highlight the information that is

achievable using this diagnostic system. Experimental results are compared to model predictions and attempts are made to bridge the apparent differences.

CHAPTER 2

DROPLET GENERATION

One of the most important droplet-based microfluidic operations is the droplet generation and entrainment process. For the high throughput capability required by the next generation of LOC and μTAS devices, rapid and controllable droplet formation is paramount. The Reynolds (*Re*) number is almost always less than unity in traditional oil-water droplet-based systems due to the highly viscous continuous phase oil. As such, the detachment process is overwhelmingly governed by the interaction between viscous and surface tension forces that lead to a well characterized Capillary (*Ca*) number dependence (Graaf et al. 2005, Graaf et al. 2006, Bui and Zhu 2007, Liu and Zhang 2009). This balance leads to well-defined droplets or slugs that inevitably lack any trailing tail features or liquid film development. This is a direct result of the surface energy of the discrete phase relative to the continuous phase which provides droplet formation and transport without direct contact with the channel walls. The continuous phase provides lubrication during transport and there always remains a thin continuous phase film separating the droplet from the channel walls. The images shown in Figure 3 provide visual confirmation of the different detachment characteristics for oil-liquid versus gas-liquid flows in a microfluidic T-junction. In high speed (>1m/s) gas-liquid droplet flows, the picture is much different and to date not well defined. Formation of liquid droplets under a high speed gas flow displays a new realm of force interactions because the inertia that would normally be neglected in oil-based flows becomes an important driving force. Additionally, the surface tension of the liquid phase also increases with incorporation of a gaseous flow. These richer dynamics lead to unusual liquid topology, which can range between asymmetrical droplets, long trailing tail slugs, thin films, and free-surface stratified flow.

Generating droplets from a continuous liquid supply stream is not a new endeavor. With the exception of early inquiry by Plateau (1873), Savart (1833), and Rayleigh (1878, 1879), technical progress and scientific understanding of droplet breakup is historically application driven. Landmark examples include agricultural fertilization, liquid fuel propulsion, and pharmaceutical development. Atomizing a liquid is a simple process. All that is required is a large velocity difference between the liquid to be atomized and the surrounding environment. This is accomplished by forcing a liquid stream through a small orifice using a large pressure difference. This brute force method for generating droplet sprays works well in fuel injectors and paint sprayers, but controlled, monodisperse droplet generation requires more sophistication and finesse. In the 1970's when ink jet printing technology was in its infancy, linear and non-linear perturbation analyses became commonplace in an effort to understand, predict, and suppress a common problem in circular jet breakup – satellite drop formation (Bogy 1979). These satellite droplets were not a new discovery. In Rayleigh's seminal work, he called these pervasive liquid vessels "spherules" (Rayleigh 1878). The resurgence of research and development during the past decade has largely been facilitated by the burgeoning microfluidic sciences, where droplet based architectures have quickly replaced continuous flow systems.

Unlike the spherical droplets observed and studied by Rayleigh, droplets formed in a microchannel are confined by the channel walls and typically take shapes that are rarely spherical. Slugs, pears, and pills are shapes the better capture confined droplet generation. Using a gaseous continuous phase complicates things further since the to-be-dispersed phase wets the channel walls. Adjectives such as unpredictable, unwieldy, and contamination prone are often used to describe gas-liquid droplet flows. However, there are a number of emerging applications that necessitate fast mixing and high throughput capability while remaining relatively simple, cheap, passive, portable, and disposable. Replacing the highly viscous continuous phase that is traditionally used to generate, encapsulate, and transport liquid droplets with a lower viscosity gaseous phase offers many advantageous over liquid-liquid counterparts. The result is a liquid film that is

produced at the liquid injection site yielding unpredictable and often hysteretic behavior, particularly in regards to droplet frequencies. Lefebvre et al. studied these characteristics in laminar atomization flows and identified the root cause of this unfavorable behavior as capillary instability (Lefebvre 1989). Since there is no viscous continuous phase to dampen capillary instabilities, it is difficult to maintain steady droplet generation rates and monodisperse size distribution. This is evidence by the lack of experimental data in the scientific literature concerning gas-liquid droplet generation in comparison to the exceptionally large body of work encompassing oil-liquid droplet generation in confined geometries.

Gas-liquid droplet generation does show the same regimes as its oil-liquid counterparts, such as the squeezing, dripping, and jetting detachment modes, but the operational window is much narrower in comparison. The squeezing regime is governed by mass conservation requirements. Characteristics of this regime are droplets that fill the height and depth of the channel completely. Droplet length is determined by the mass flow rate ratio of the two phases. The result is large droplets detaching at frequencies less than 1Hz and large pressure requirements. The series of images in Figure 4 illustrate this type of detachment regime. The scaling laws derived in the Theoretical Modeling section suggest mixing time is reduced by decreasing the size of the droplet and increasing its velocity, which contradict the traits offered by the squeezing regime.

Increasing the flow rate of the continuous phase transitions the squeezing to the dripping regime. As the name suggests, this regime is analogous to water dripping from a kitchen faucet. It is characterized by a wetted orifice that detaches droplets smaller than the channel dimensions. Since the capillary instabilities are maintained at the injection orifice, the detachment process occurs at or just following the injection site. A typical dripping process in co-axial flow geometry is shown in Figure 5. Operation in this regime provides small droplets at frequencies near 100Hz. The biggest advantage, however, is that single droplets can be generated when operated in pulse mode. For studying mixing dynamics in colliding droplets, single shot operation is highly advantageous.

The jetting regime is the third and final droplet generation regime for Newtonian liquids. It is most probable with increasing velocity of the continuous phase, higher flow rate and viscosity of the discrete phase, and lower interfacial tension between each phase. A steady capillary jet of fluid surrounded by an immiscible continuous phase is intrinsically unstable. However, it can be locally stable and used to produce droplets of various sizes. Calvo developed an elegant analytical model of unconditional jetting using dispersion relations and developed a map based on Capillary (*Ca*) number and viscosity ratio (2008). For air, the critical *Ca* number is ~ 0.2 and implies that liquid velocities in excess of 15m/s are required for locally stable jetting conditions. The relatively large velocity provides sufficient inertia to push the capillary instabilities downstream resulting in a long thin thread of liquid that inevitably breaks up into droplets. The viscosity of the liquid plays a crucial role in stabilizing the interface by mitigating the growth of capillary perturbations. This conjures pictures of honey dripping from a spoon, making a long, thin, viscous thread that is difficult to break even after vigorously shaking the spoon. Since instabilities are propagated by surface tension, longer jetting threads result as the surface tension between the two phases decreases.

Jetting is easily observed in everyday life by simply increasing the flow rate on a dripping faucet. In fact, the numbers of journal papers that focus on the transition from dripping to jetting in relation to a simple faucet seem to grow each year without bound as

this seemingly straightforward problem is mathematically complex to model and experimentally difficult to quantify. A concise mathematical expression that describes the transition point between dripping and jetting and encompasses all relevant flow parameters remains non-existent. See, for instance, the comprehensive review by Eggers (Eggers and Villermaux 2008). The characteristics of jetting are small droplets generated at frequencies in excess of 1 kHz. The smallest droplets (Jeong et al. , Anna and Mayer 2006) and the highest frequency (Herrada et al. 2008) to date has been achieved using the jetting regime. The major limitations using this technique for droplet generation is the excessive channel length requirement, polydisperse size distribution due to satellite drop formation, substantial driving pressure requirements, and most important, its sensitivity to external perturbations that negatively affect thread development and droplet generation consistency. The series of images below show the generation of a liquid jet, the growth of perturbations, and the breakup of the thread. Even with optically isolated tables, it is difficult to eliminate all sources of perturbations in order repeatably and consistently generate droplets using the jetting regime.

In the work to follow, experiments are conducted to understand how detached droplet volumes are influenced by the gas *Reynolds* number and microchannel aspect ratio. Modified non-dimensional numbers are formulated to reveal the dominate droplet detachment mechanism across a decade of gas *Reynolds* numbers. The major limitation of T-junction geometries, wetting of the discrete phase, is then discussed and techniques are presented that suppress droplet filming and increase the utility of gas-liquid droplet generation. Finally, droplet volume and generation rate data is given that covers a range of device geometries. Never before have mono-dispersed droplets been formed in a confined gaseous microchannel flow with such repeatability.

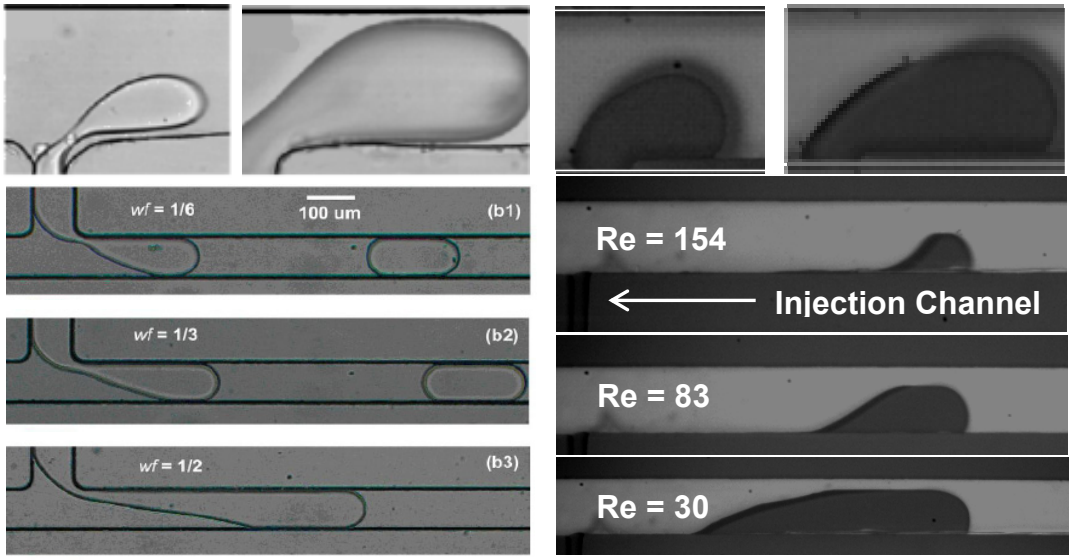

Figure 3. Water droplets detaching into an oil flow under highly viscous conditions (Christopher and Anna 2007) (top left). Experimental results of water droplet detachment into a gaseous flow (top right). Note that the droplet is in direct contact with the channel walls compared to the oil-based flow shown to the left. The influence of oil-water flow rate ratio on detached water droplet geometry (Xiang and LaVan 2009) (lower left). Experimental results showing influence of air Re number on detached water droplet geometry (lower right). Even under small air Re number, the detached droplet never fills the channel width as compared to the oil-based flow.

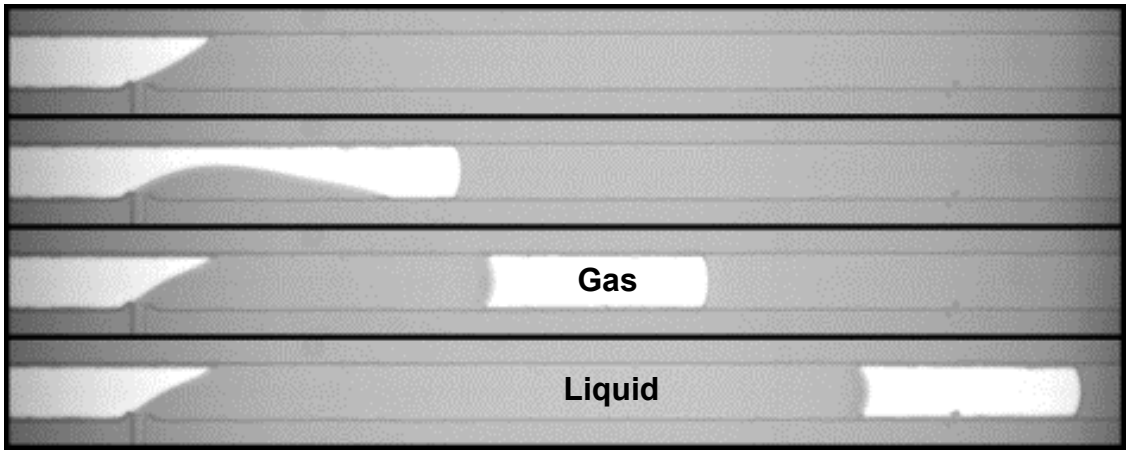

Figure 4. Series of experimental images showing liquid slug generation in a gaseous microflow. Operating in the squeezing regime yields slugs that characteristically fill the channel cross-section. Slug size is determined by the liquid/gas flow rate ratio.

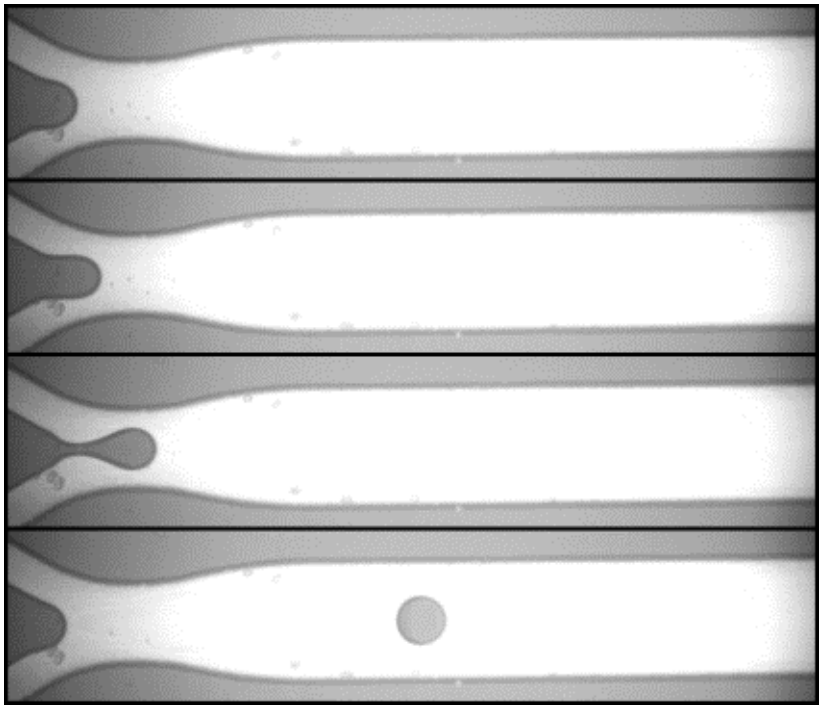

Figure 5. High-speed experimental images of gas-liquid droplet generation in a coaxial flow geometry. The main channel is 300μm and the size of the liquid injection channel is 20mm. Note the wetting of the liquid at the injection site. This is a characteristic of the dripping regime.

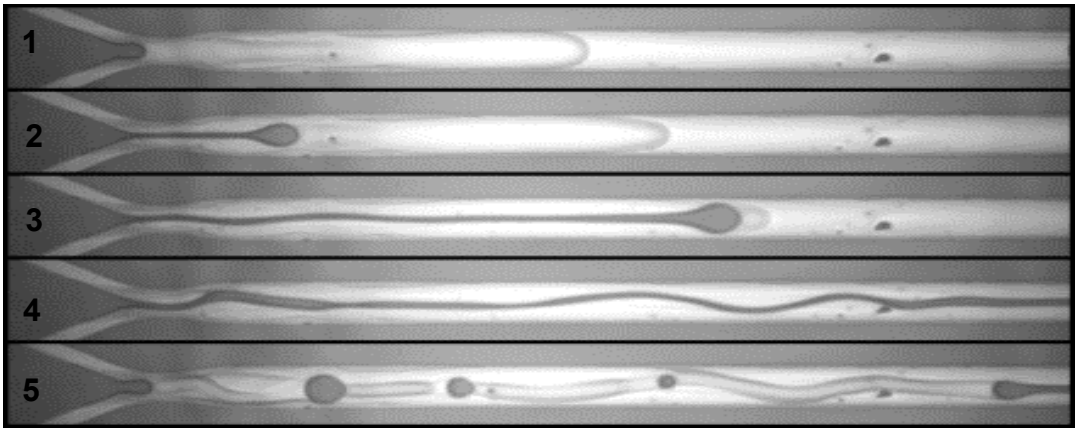

Figure 6. A sequence of experimental images showing the growth and breakup of a capillary thread due to instabilities. Liquid is injected into a coaxial gas flow (1), liquid jetting forms a capillary thread (2), and instability begins to develop (3), propagate (4), and break the thread (5).

2.1 Droplet Detachment Mechanism

The flow regime of interest in order to achieve the dripping regime using T-junction geometries ranges from $10 < Re_{Dh} < 200$, where Re_{Dh} is the Reynolds number for air based on the average air velocity, channel hydraulic diameter, and air viscosity. This dynamic range should identify a transitional region where inertia supersedes viscous dominated detachment. Results of droplet height, length, and volume were obtained for four different microchannel devices and three different channel aspect ratios. Figure 7 shows a representative device used for detachment studies. The channel height and depth for each microchannel are 105x59μm, 100x50μm, 100x50 μm, and 188x44μm with corresponding aspect ratios (*AR*) of 1.75, 2, 2, and 4.25, respectively. Figure 8 and Figure 9 show detached droplet length and height for each experiment. Droplet height is confined by the height of the microchannel and therefore does not show as large of a change as compared to droplet length. Detached droplet aspect ratio, defined as droplet length over droplet height, is shown in Figure 10. The microchannel with an aspect ratio of 4.25 consistently produced with the smallest aspect ratio.

Droplet morphology is captured by the high speed images shown in Figure 11, which are for a device with an aspect ratio of 2. As the Re_{Dh} increases, the detached shape transforms from a slug to a more spherical like droplet. Note that the height of the droplet does not change as significantly as droplet length. The detachment of a single droplet in a Re_{Dh} of 118 is shown by the images in Figure 12. The droplet grows primarily in the lateral direction during the initial stages of detachment. Once the air flow is reduced, lateral growth gives way to longitudinal growth. The droplet continues growing in length until the surface tension pinning the droplet at the injection site is overcome by stresses induced by the high speed air flow.

To predict the dominant mechanism leading to detachment, simple scaling analyses are performed using the detached height and length data. The schematic in Figure 13 provides the relevant channel and droplet dimensions. By non-dimensionalizing the measured droplet length by the channel hydraulic diameter, the data for each device collapses largely onto a single curve. This trend is consistent with previous measurements (Hidrovo et al. 2005). The non-dimensional droplet height, however, does not show this behavior for large aspect ratios. Note that the non-dimensional droplet height can exceed unity since the channel hydraulic diameter is less the channel height H for all devices tested.

The flow field of interest for droplet detachment is in the x-y plane. The initially fully developed flow must accelerate around the emerging droplet. Drag forces induced by the air flow compete with the surface tension force holding the droplet at the injection site. The sources of the drag force can be viscous, inertial, or hydrodynamic pressure difference. The viscous force shears the droplet while inertial drag pushes the droplet. The hydrodynamic pressure force results from the pressure drop as the air flows through the small gap between the top of the droplet and channel wall.

The dominant detachment mechanism can be verified by taking the ratio of the viscous, inertial, and hydrodynamic pressure forces to the surface tension force securing the droplet. A ratio near unity indicates a balance between the detachment force and

droplet pinning force. Assuming an x-y flow field with negligible lateral pressure gradient, the mass and x-direction momentum equations are:

$$\frac{\partial u}{\partial x}+\frac{\partial v}{\partial y}=0 \qquad \mathbf{1}$$

$$\rho\left(u\frac{\partial u}{\partial x}+v\frac{\partial u}{\partial y}\right)=-\frac{dp}{dx}+\mu\left(\frac{\partial^2 u}{\partial x^2}+\frac{\partial^2 u}{\partial y^2}\right) \qquad \mathbf{2}$$

The air flow upstream of the droplet is fully developed but the flow in the narrow gap between the droplet and adjacent wall is not. Therefore, the inertia terms appearing on the left side of the momentum equation cannot be neglected. The terms on the right side of the momentum equation represent the force contributions due to axial pressure drop, normal viscous force, and tangential viscous force. The relative magnitudes of each term in the momentum equation can be quickly assessed by scaling arguments. The assumed velocity and length scales in the gap are as follows:

$$\begin{aligned} u &\sim U\,H\big/(H-h) \\ x &\sim l \\ y &\sim H-h \end{aligned} \qquad \mathbf{3}$$

In the above equation, U is the average velocity in the channel, H is the channel height, and l and h are droplet length and height, respectively. The y-velocity scale is found by scaling the mass conservation equation the known scales to yield:

$$v\sim\frac{UH}{l} \qquad \mathbf{4}$$

Substituting these scales into the momentum equation yields the following:

$$\rho\frac{U^2}{l}\left(1-\frac{h}{H}\right)^{-2}\sim\frac{\Delta p}{l},\mu\frac{U}{l^2}\left(1-\frac{h}{H}\right)^{-1},\mu\frac{U}{H^2}\left(1-\frac{h}{H}\right)^{-3} \qquad \mathbf{5}$$

The dominating geometric parameter is clearly the ratio of droplet height to channel height. For this reason, the first viscous term can be neglected. This leaves three contenders to balance the droplet pinning force.

During the growth process, the droplet wets the channel walls and remains attached to the surface. The force securing the droplet to the injection site is:

$$F_P = \sigma \cos(\theta_R - \theta_A)(W + 2h) \quad \textbf{6}$$

The angles in parentheses, θ_R and θ_A, are the receding and advancing droplet contact angles. These are readily evident in the images shown in Figure 11 and range from $30^o < \theta_R < 40^o$ and $100^o < \theta_A < 110^o$. This force acts along the contact line of the droplet and channel wall.

Using the measured gas flow rates, channel dimensions, and droplet length and height, the dimensionless parameters that scale the contributions of gas phase inertial changes, viscous stresses, and hydrostatic pressure differences are calculated. The ratio of the inertial force of the gas to the surface tension pinning force gives a modified Weber (We_{Mod}) number:

$$We_{Mod} = \frac{\rho U^2 \left(\frac{H}{H-h}\right)^2 lW}{\sigma \cos(\theta_R - \theta_A)(W + 2h)} \quad \textbf{7}$$

We_{Mod} is plotted against Re_{Dh} in Figure 16. This ratio is greater than unity for all channel aspect ratios considered past a Re_{Dh} of 50.

The ratio of the viscous force imposed by the gas to the surface tension pinning force gives a modified Capillary (Ca_{Mod}) number:

$$Ca_{Mod} = \frac{\mu U \left(\frac{H}{H-h}\right) \frac{lW}{H-h}}{\sigma \cos(\theta_R - \theta_A)(W + 2h)} \quad \textbf{8}$$

Data for Ca_{Mod} across the range of Re_{Dh} is shown in Figure 17. At low $Re_{Dh,}$ Ca_{Mod} is of order unity and decays as Re_{Dh} increases. The exception is the channel with the smallest aspect ratio, which remains above 1 across the flow range considered. However, Ca_{Mod} is less than We_{Mod} for all tested devices once a Re_{Dh} of 60 is exceeded. This indicates a transition from viscous dominated drag to inertial drag.

The last force of interest is the pressure difference that results due to viscous losses and inertial gains in the narrow gap. The result is a net pressure force acting in the flow direction. Assuming a fully developed flow, the pressure through the gap is estimated as:

$$\Delta p = f \frac{l}{D_{h,Gap}} \frac{1}{2} \rho U_{Gap}^2 \qquad \textbf{9}$$

The value of the friction factor f depends on the shape of the channel cross-section. For a round tube, $f\,Re_{Dh}$ is 64 while for a duct of infinite depth is 96. A duct with an aspect ratio of 4 gives an $f\,Re_{Dh}$ of ~73. The gap aspect ratio (gap height / channel depth) for these tests was approximately 1.5 for all devices except for the 4.25 aspect ratio channel, which showed a gap aspect ratio of approximately 3. The $f\,Re_{Dh}$ used for this analysis was 57 for AR = 1.75, 2 and 73 for AR = 4.25. The ratio of pressure to surface tension forces is then:

$$\frac{Pressure\ Force}{Surface\ Tension\ Force} = \frac{\Delta p h W}{\sigma \cos(\theta_R - \theta_A)(W + 2h)} \qquad \textbf{10}$$

The pressure force to surface tension ratio for the range of Re_{Dh} tested is shown in Figure 18. The important thing to note here is that this ratio is larger than unity for all detached droplets but decreases as Re_{Dh} increases much like Ca_{Mod}. This indicates that the dominant detachment mechanism at low Re_{Dh} but transitions to inertial drag mechanism as Re_{Dh} increases. This is captured by the plot in Figure 19 which shows the inertia and pressure detachment ratios for the 100x50mm microchannel. The transition from pressure to inertial detachment occurs near Re_{Dh} of 100. These results display the same trends as shown by Hidrovo et. al. (2005), but in their study the inertial transition occurred near $Re_{Dh} \sim 200$ for a channel aspect ratio near 11. The pressure to inertial transition is also

captured visually by inspection of the still images in Figure 11, where the elongated slugs become nearly spherical droplets once *ReDh ~ 100* is exceeded.

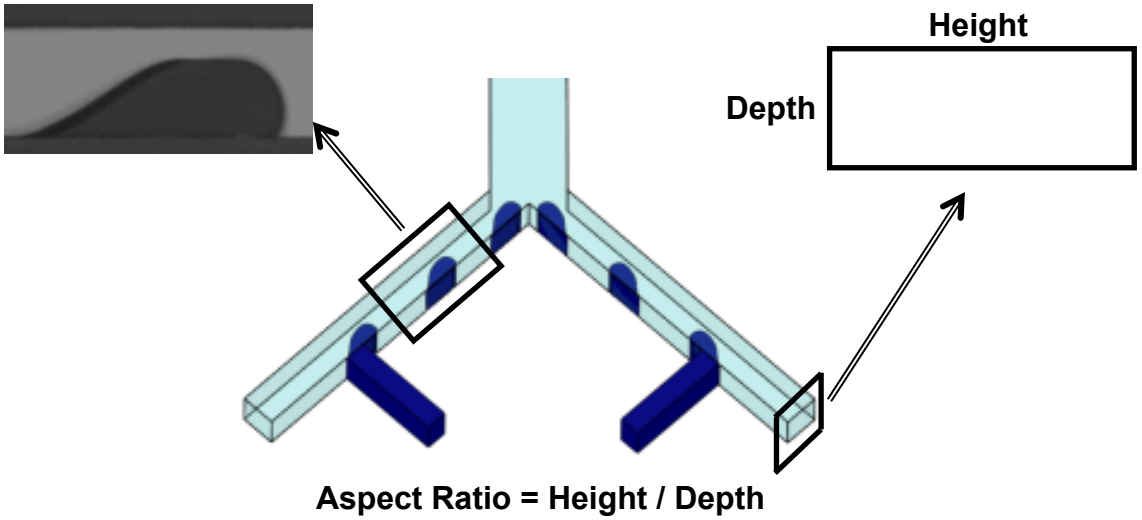

Figure 7. CAD image (not to scale) of the gas-liquid microfluidic device used for droplet detachment and droplet collisions studies. Four different devices were tested with the following aspect ratio: 1.75, 2.0, 2.0, and 4.25.

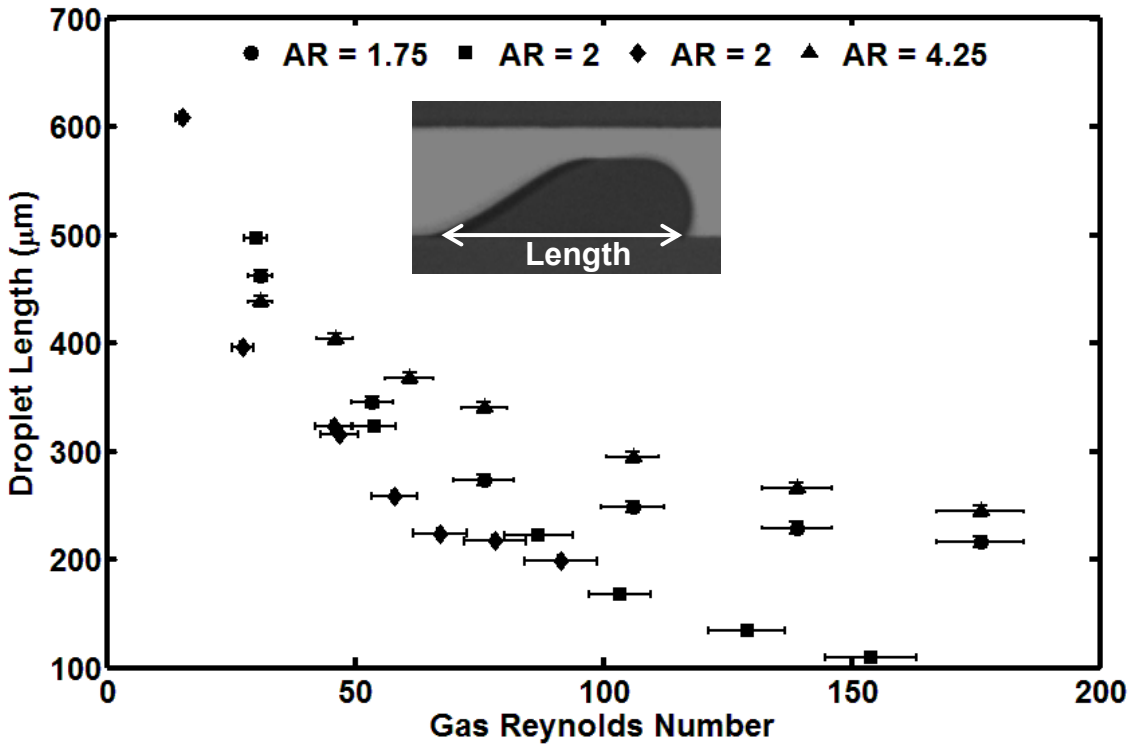

Figure 8. Experimental data of detached droplet length versus air Reynolds number for three different channel aspect ratios and four different devices.

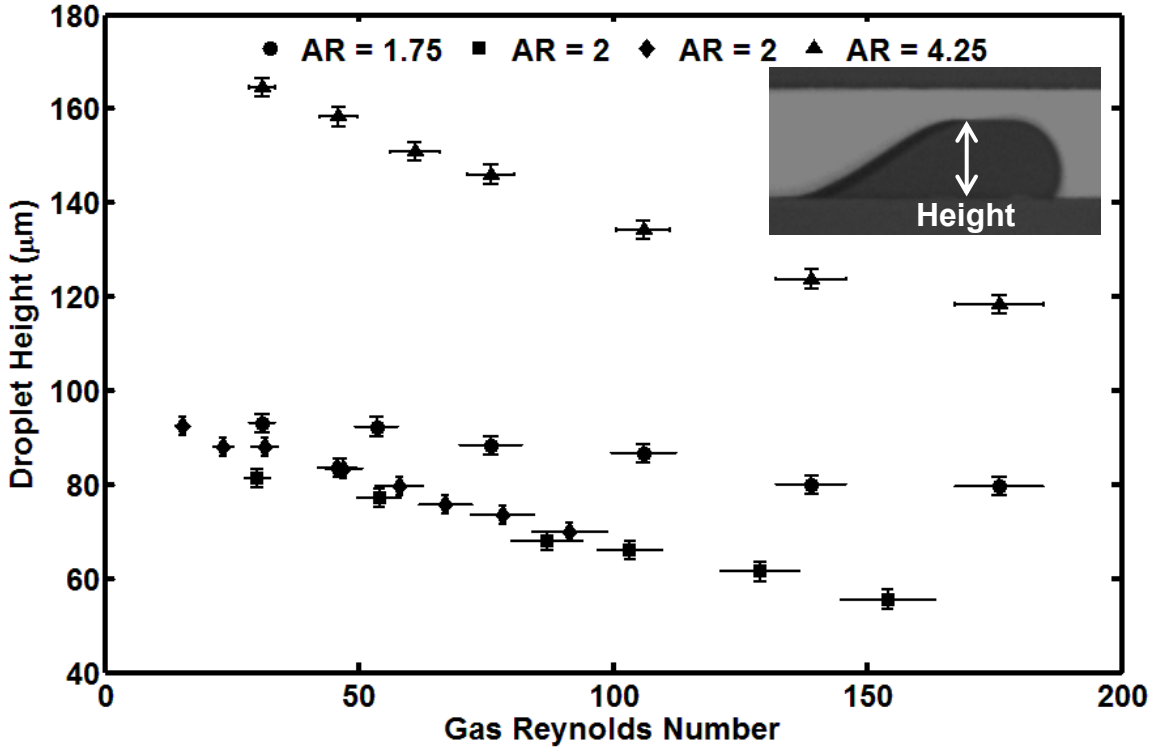

Figure 9. Experimental data of detached droplet height versus air Reynolds number for three channel aspect ratios (channel height / channel depth) and four different devices.

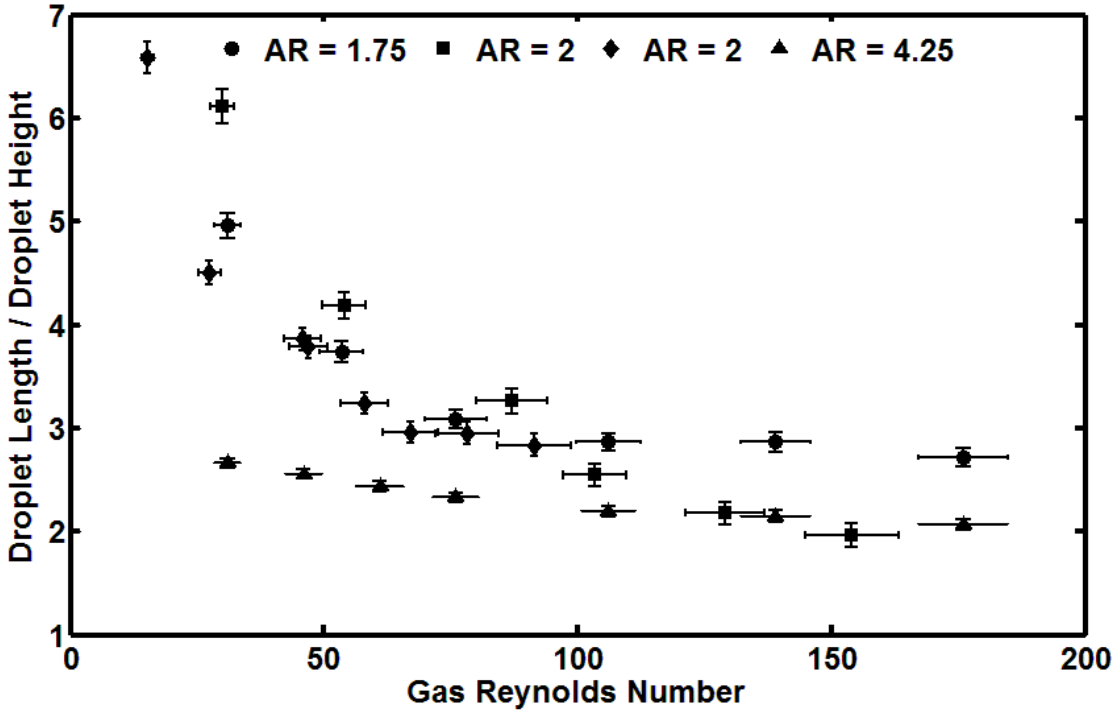

Figure 10. Experimental data showning how the ratio of droplet length to height decreases with increasing air Reynolds number for three different channel aspect ratios and four different devices.

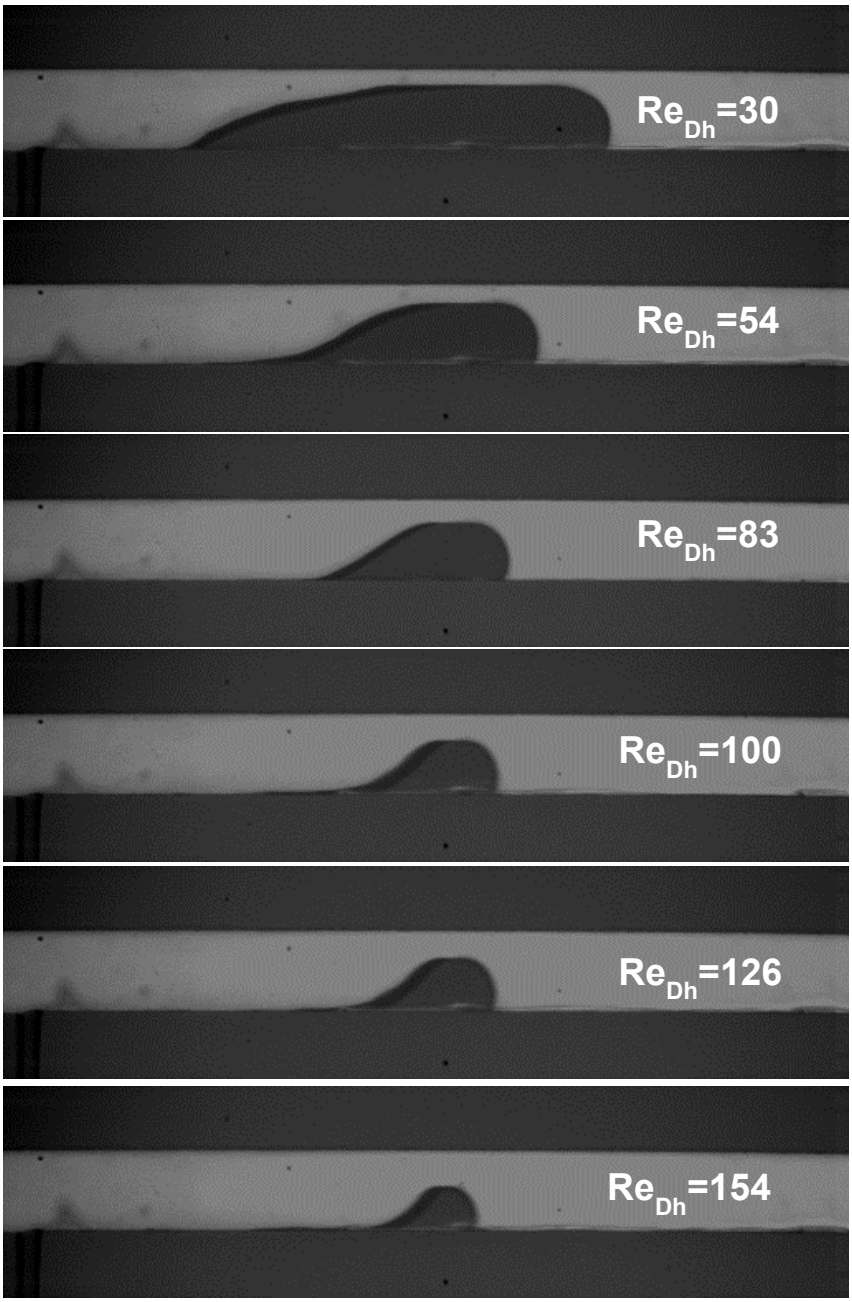

Figure 11. High speed camera images of droplet geometry for different gas Reynolds numbers (Re_{Dh}) for a channel 100μm high and 50μm deep. Note that the elongated slugs become spherical droplets as the gas *Reynolds* number is increased. The detachment mechanism transitions from pressure to inertia dominated past Re_{Dh} ~ 100.

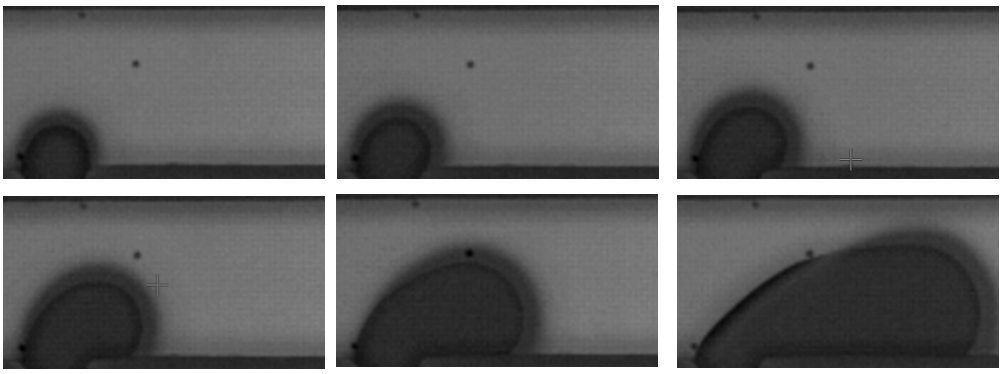

Figure 12. High speed camera images of droplet growth and detachment for Re_{Dh} = 118. Time between image frames is 1ms.

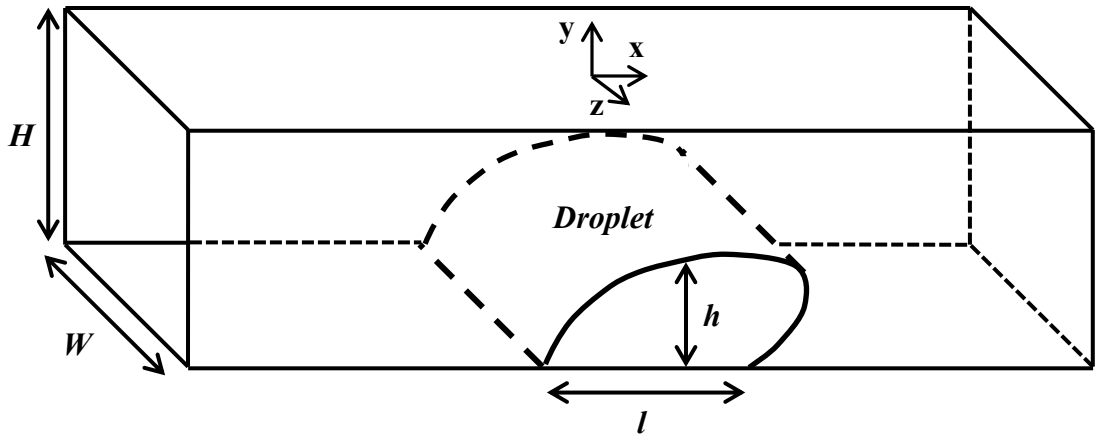

Figure 13. Schematic of rectangular microchannel with a detached droplet/slug on the lower wall. The channel dimensions are: height, *H,* and depth, *W*. The droplet dimensions are height, *h*, and length, *l*. The Cartesian coordinate system used for the detachment analysis is also indicated.

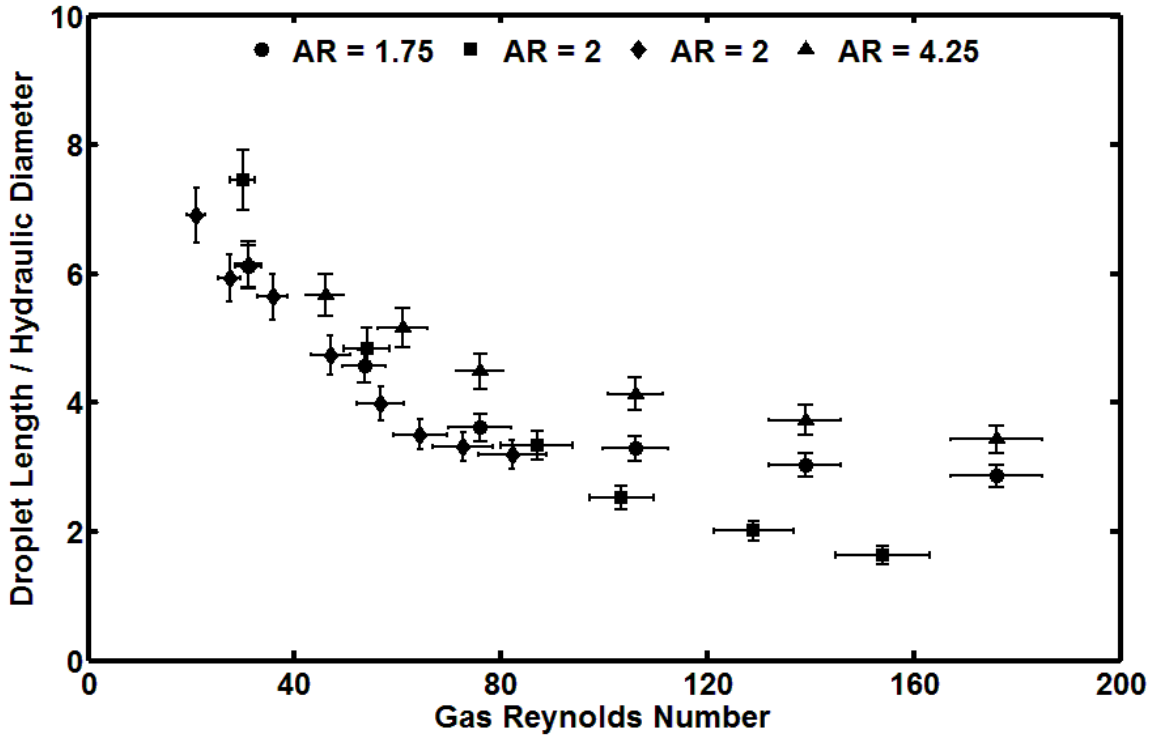

Figure 14. Experimental data of detached droplet length versus air Reynolds number for three different channel aspect ratios and four different devices. Data has been non-dimensionalized by channel hydraulic diameter.

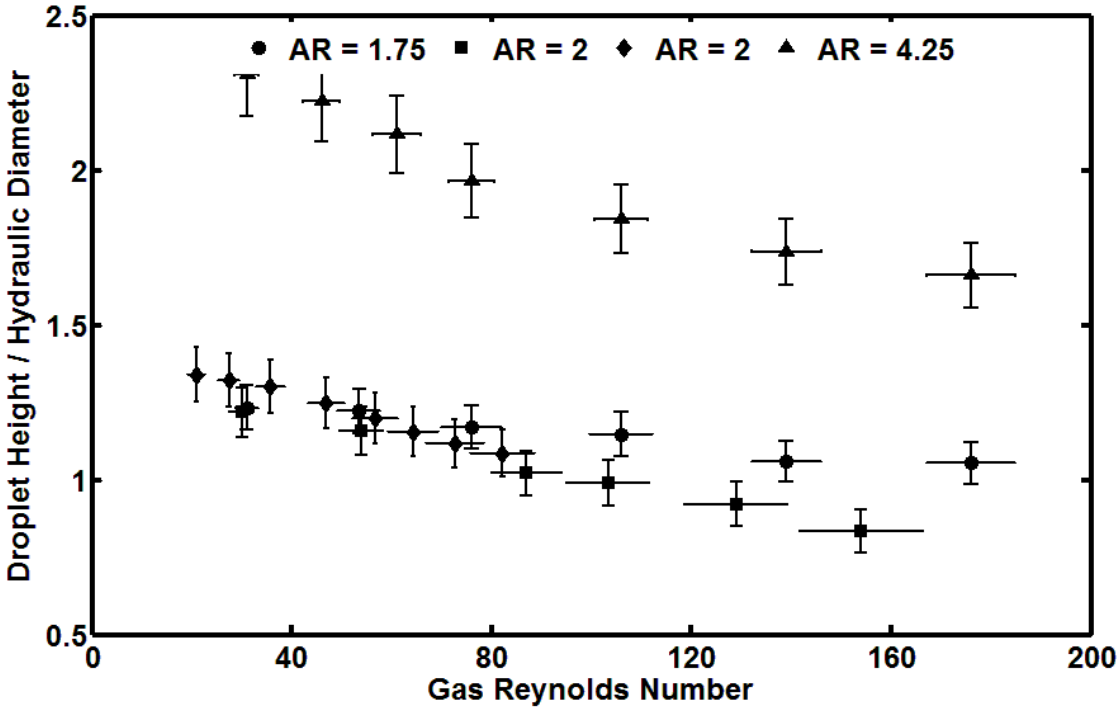

Figure 15. Experimental data of detached droplet height versus air Reynolds number for three different channel aspect ratios and four different devices. Data has been non-dimensionalized by channel hydraulic diameter. Note that the droplet height ratio can exceed unit using this non-dimensionalization.

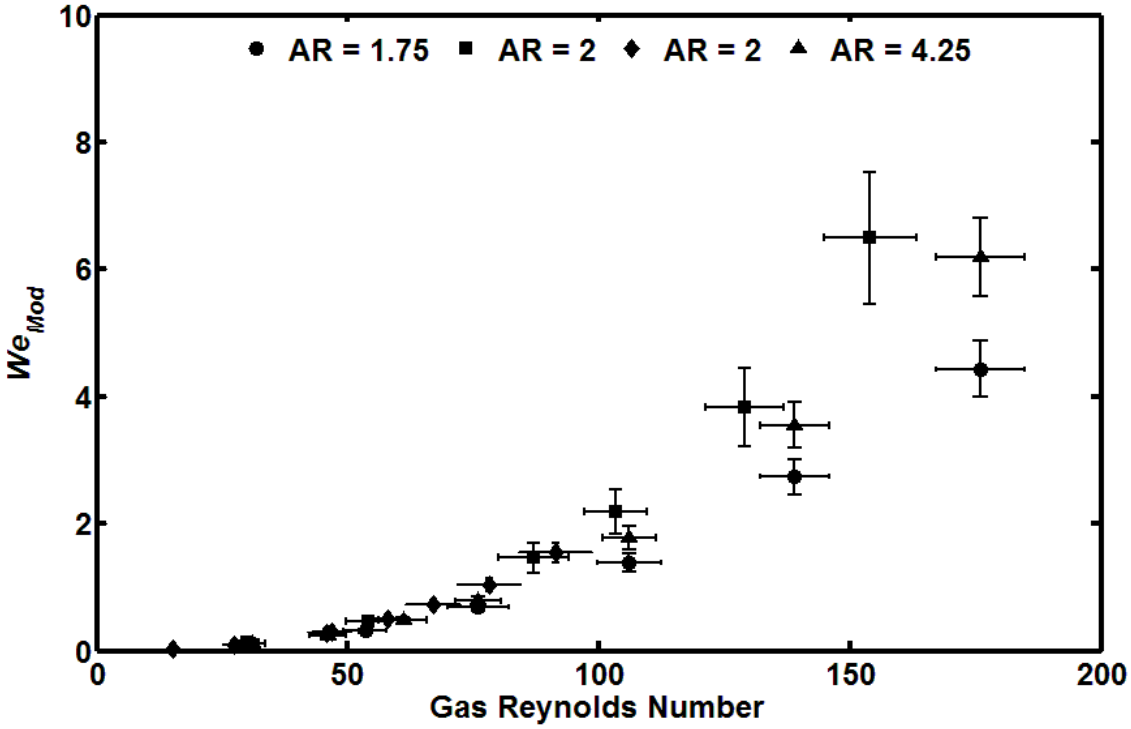

Figure 16. Plot showing how the ratio of gas-phase inertial force to droplet surface tension, We_{Mod}, changes with increasing Re_{Dh}. The ratio exceeds unity past a Re_{Dh} 80 and indicates a transition to inertial droplet detachment.

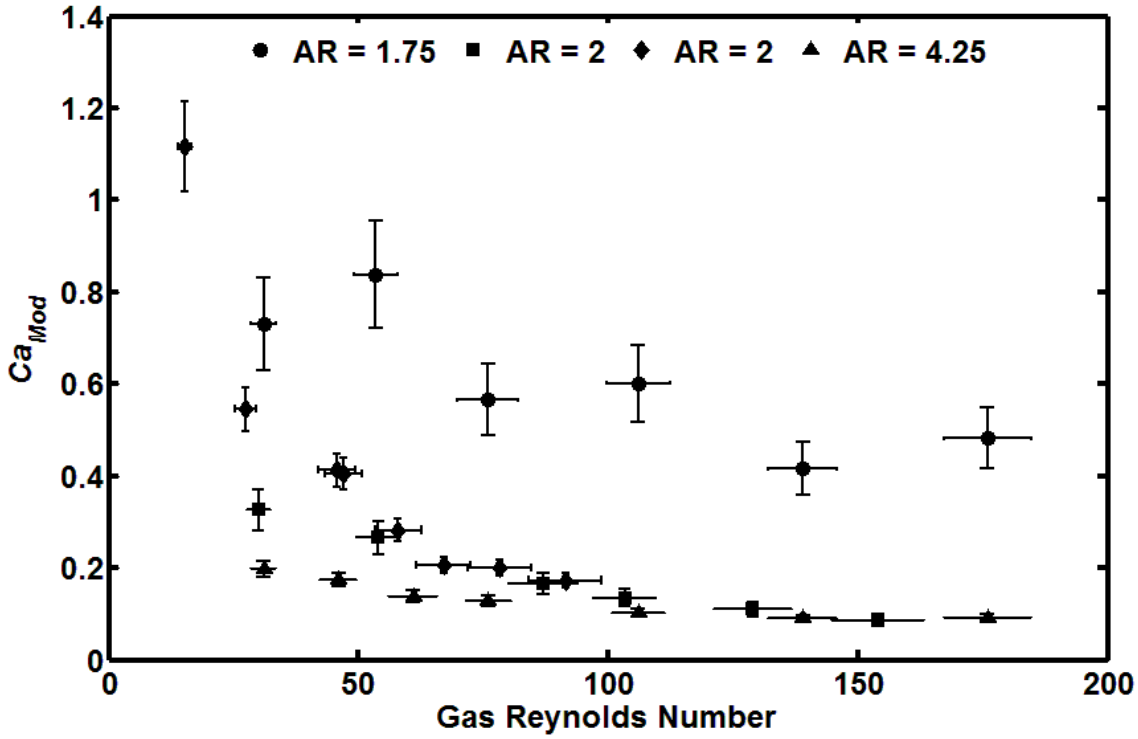

Figure 17. Plot showing how the ratio of the imposed gas-phase viscous force to droplet surface tension, Ca_{Mod}, changes with increasing Re_{Dh}. The ratio is less than unity for all channel aspect ratios considered.

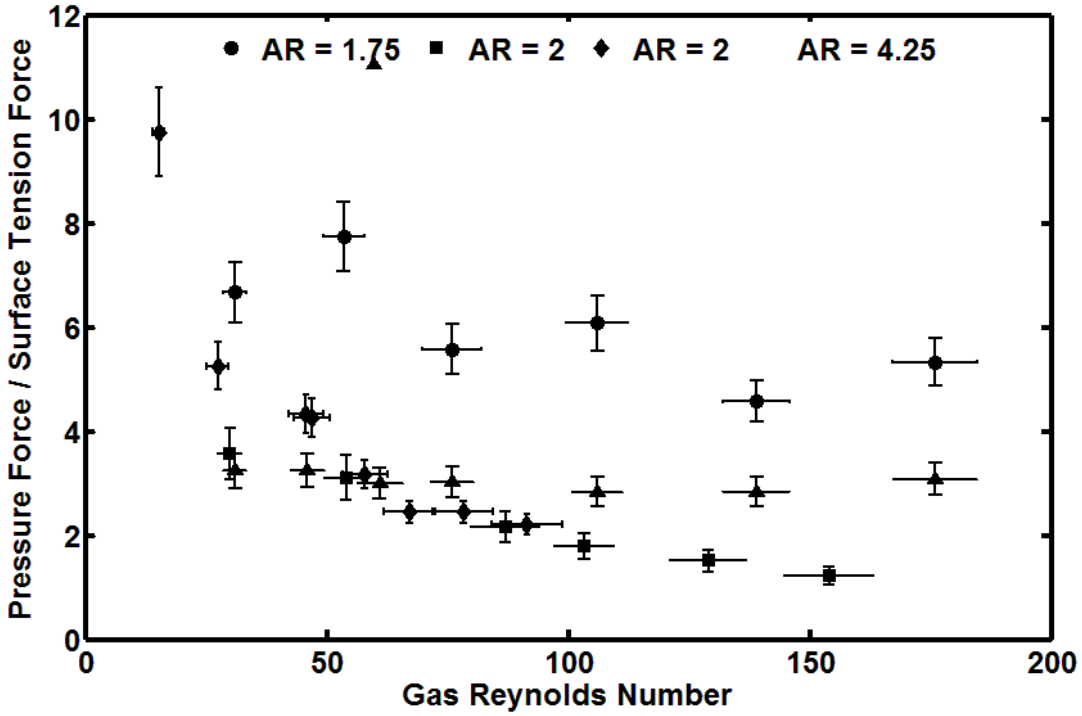

Figure 18. Plot showing how the ratio of pressure drop across the droplet to the surface tension securing the droplet at the injection site changes with increasing Re_{Dh}. The ratio is largest for the channel with the smallest aspect ratio and decreases for all channel sizes with increasing Re_{Dh}.

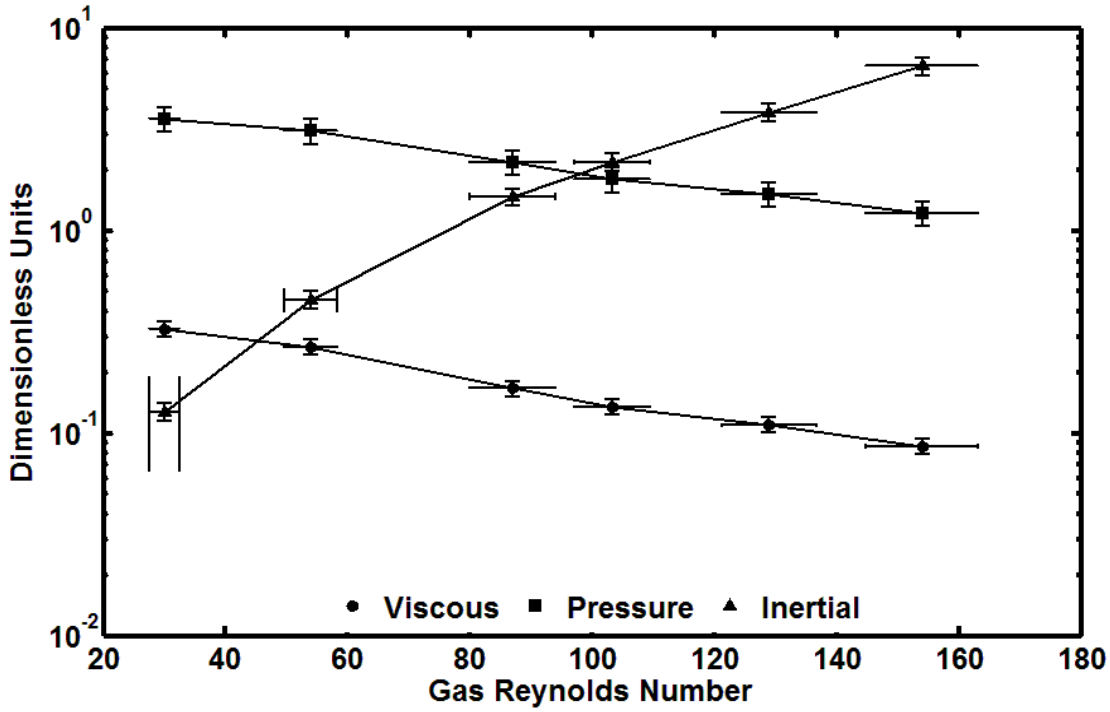

Figure 19. Comparison of viscous, pressure, and inertial force detachment ratios for the 100x50μm channel (connecting lines added for clarity). The mechanism of detachment transitions from pressure to inertial near Re_{Dh} of 100. Note that the influence of viscous forces decreases with increasing *Reynolds* number and does not become a dominant detachment mechanism across the *Reynolds* number ranges considered.

2.2 Film Suppression

The foregoing results were obtained for extremely low liquid flow rates (<10μL/hr). As the liquid flow rate is increased to levels of practical importance, droplet formation becomes usurped by liquid film development. This is most striking difference between oil-liquid and gas-liquid droplet generation: wetting of the channel walls by the dispersed phase. This is readily observed by the sequence of fluorescent images in Figure 20 where a droplet emerging from a T-junction injection site leaves thin film in its wake. This behavior circumvents droplet formation and remains a major challenge for gas-liquid microfluidics.

The origin of the film may be related to changes in the Laplace pressure of the emerging droplet. Once the emerging droplet overcomes the capillary pressure of the injection channel and enters the main channel, there is a rapid release of liquid. This is supported by the image and plot in Figure 21. The image is a combination of eight separate images taken during the filming detachment of a single droplet. Each color corresponds to the change in volume between each image and the time stamp denotes the difference in time between each frame. The plot below shows the time history of the droplet volume change for the eight separate images. This sequence shows how the instantaneous flow rate changes during the detachment process. As the droplet emerges from the injection channel, there is little change in the droplet volume during the first 8 seconds. The curvature of the liquid gas-interface is nearly uniform, positive, and on order of the 15μm injection width. Considering this as the dominate curvature gives a pressure jump of 0.7psi, which is 14% of the upstream driving gas pressure (~5psi). Within the next 3ms, droplet volume begins to increase rapidly. The interface curvature near the top of the emerging droplet increases during this time and eventually becomes flat. This decrease in Laplace pressure causes liquid to quickly issue from the injection site it is the upstream driving pressure and not the flow rate that is controlled. The result is a slug-type droplet followed by a trailing film.

The most unsettling feature of filming in gas-liquid microflows is the persistence of the film. In order to repeatably produce a pair of colliding droplets downstream, the droplet film formation must be suppressed. There are potentially three techniques in which film mitigation can be accomplished: chemical surface treatments, channel geometry modification, and controlled instability generation. Chemical surface modifications reduce the surface energy of substrate material, making the exposed channel walls hydrophobic. Geometric modifications employ obstacles and flow area changes to limit or confine film development. Lastly, instabilities can be generated that effectively break the film at or near the injection site. In an effort to maintain the biocompatibility of the PDMS substrate material, chemical surface modifications were

not explored to a reportable degree. Only geometric alterations and perturbation methods are discussed below.

A number of geometric variants were designed, fabricated, and tested. The two most successful geometric changes were a raised liquid injection site and incorporation of a secondary gas injection site. An image of the raised injection site geometry is shown in the upper portion of Figure 22. The sudden contraction and expansion of the gas flow passage effectively suppresses liquid film development. Compared to the images and plot in Figure 21, the volume filling process for the raised injection geometry is nearly linear with time. The slight pressure recovery just following the injection site limits the liquid jet that would otherwise issue from the injection site.

The second successful geometric variant used for film suppression was a secondary gas injection channel. The design is similar to air-assist atomization devices described by Lefebvre for gas turbine applications (1989). A liquid film is formed from a standard T-junction injection site. Approximately five to ten channel diameters downstream a secondary gas flow is injected. The liquid film is unable to maintain continuity across the gas injection site and consequently breaks up into one or more droplets. The most interesting feature of this design is that the ratio of primary to secondary airflow rate determines the deflection of the detached droplet. When the primary gas flow rate is greater than the secondary gas flow rate, the droplet is detached to the same wall as the film. When the primary gas flow rate is greater, the droplet is detached to the opposite wall. This is shown in the sequence of images in Figure 23. For conditions where both flow rates are equal, the droplet is detached from the wall and is entrained down the center of the channel, as shown in Figure 24. This type of flexibility is not offered traditional T-junction or flow focusing devices and to date has not been demonstrated.

The last technique that successfully mitigates filming conditions is controlled instability generation. In this case, the instability is manifested by driving the liquid solenoid valve at varying frequencies to produce a pulsing flow rate. The pulsating flow rate limits the surge of liquid that would issue from the ejection site as the Laplace

pressure suddenly decreases as the liquid is ejected. The result is a droplet that forms just downstream as the film ruptures in response to the sudden flow rate reduction. The series of images in Figure 25 illustrates the film rupture process. The driving frequency and pulse width of the solenoid is 35Hz and 25ms, respectively. Shortly after a trailing film droplet is ejected into the channel, the solenoid valve closes. Starved of flow, the film is unable to maintain continuity and ruptures and releases a droplet.

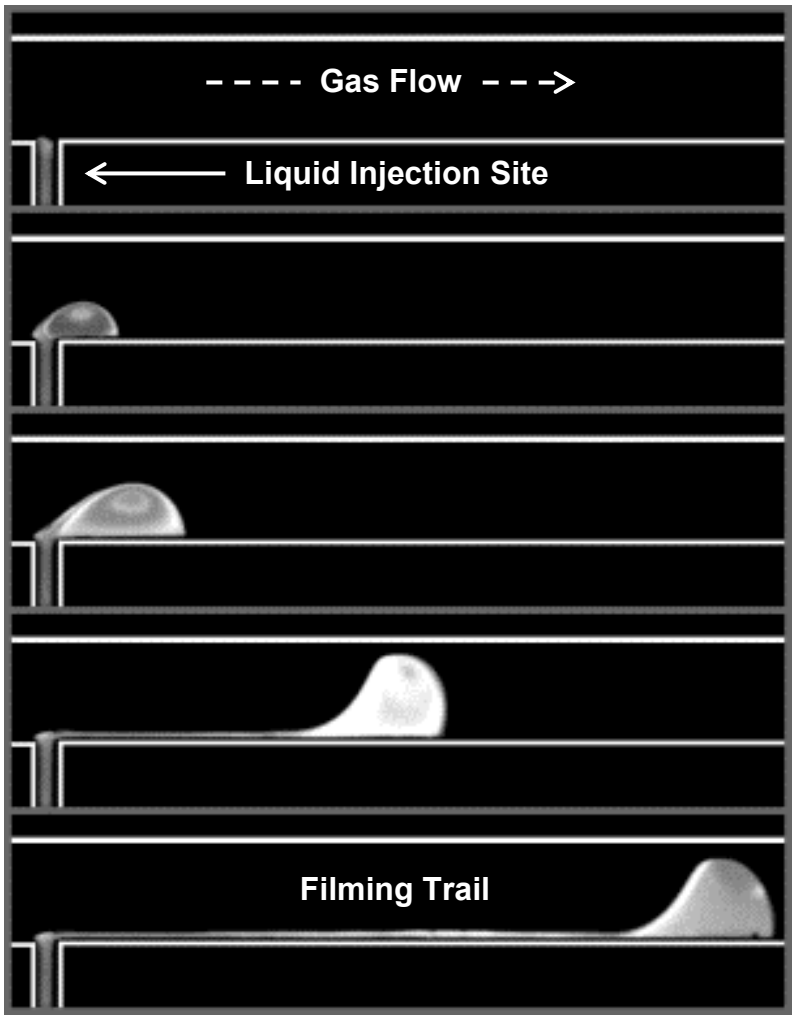

Figure 20. Series of experimetal images showing film formation during the detachment process. Fluorescence is used for increased contrast and channel boundaries have been added for reference.

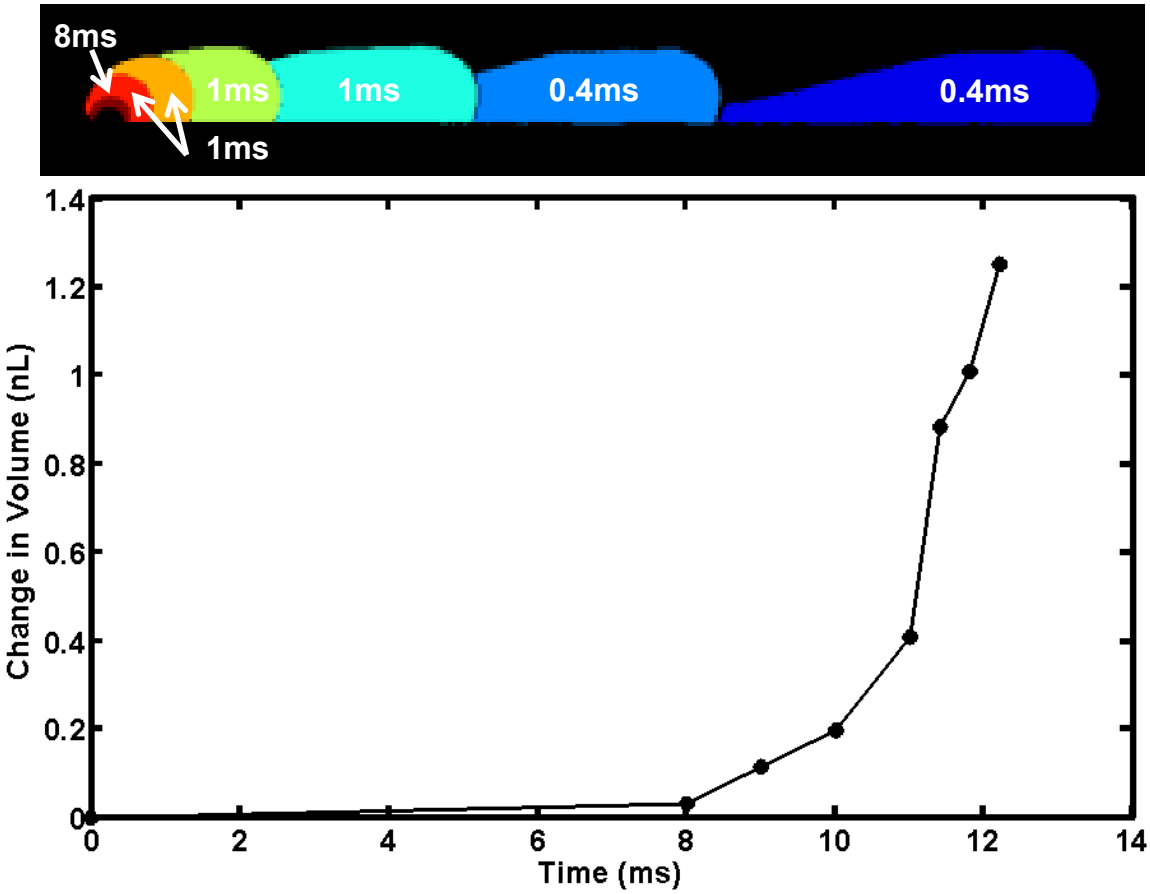

Figure 21. A series of experminetal images of the droplet growth process at a T-junction. Eight serperate images have been combined and pseudo colored according to difference in volume between each previous image. The plot shows the change in droplet volume with time. Note that the volume of liquid issuing from the injection site is not constant with time but rapidly accerlerates due to the decrease in Laplace pressure at the liquid-gas interface once the liquid emerges from the injection site.

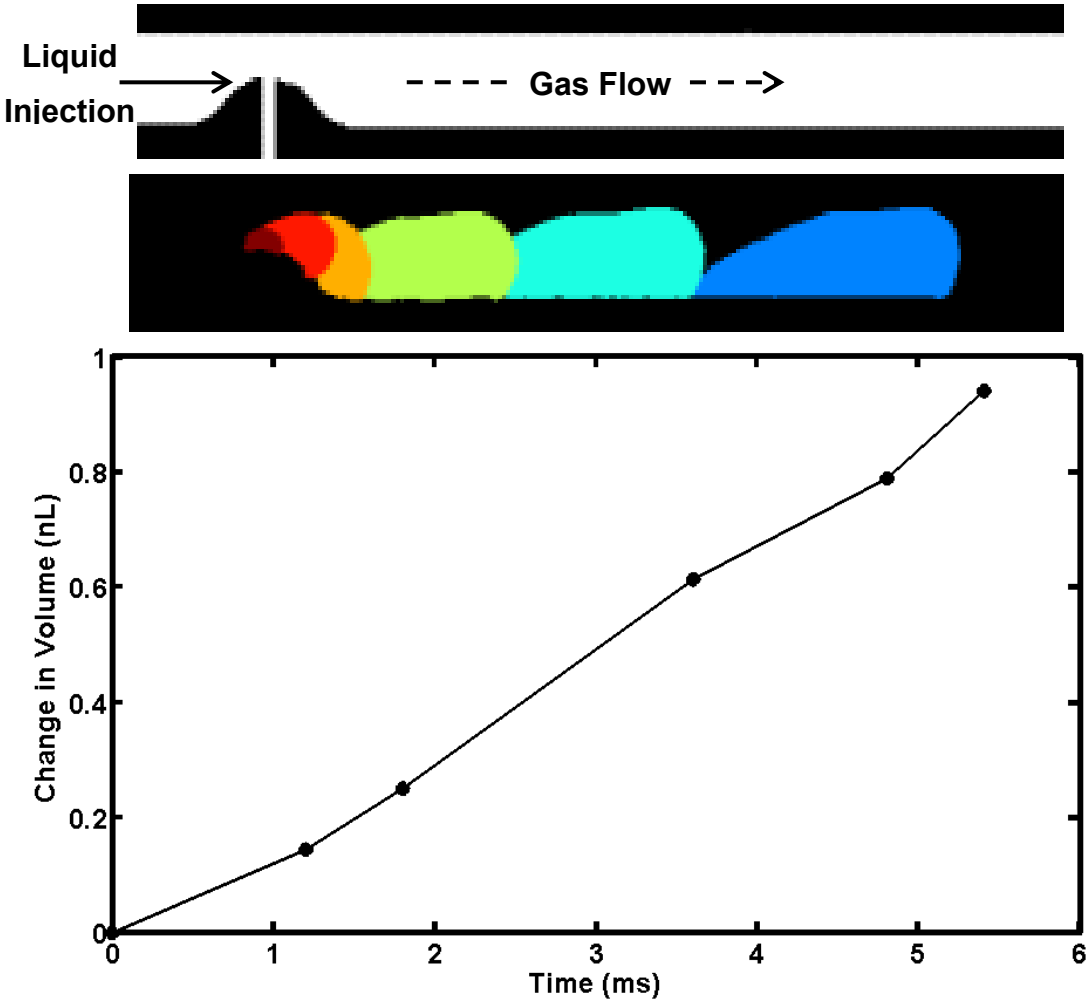

Figure 22. The top image shows the modified liquid injection geometry used to suppress film formation. The lower image is a combination of seven images that have been pseudo colored to show the change in droplet volume between each previous image. The plot shows the change in droplet volume with time. Note the nearly constant volume filling which helps supress film formation.

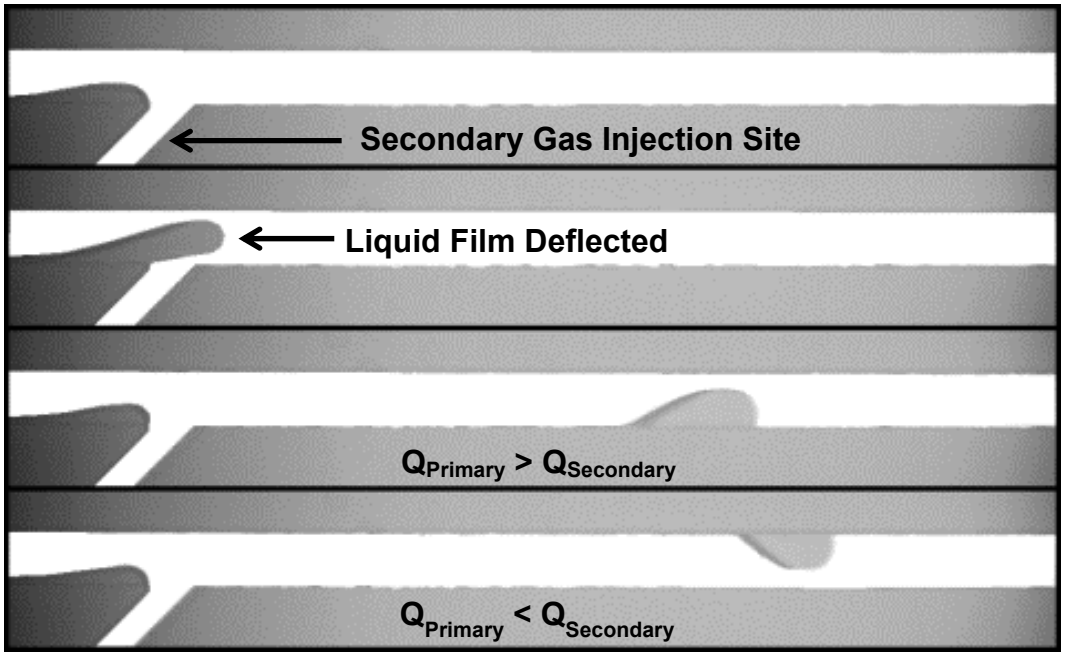

Figure 23. A series of images showing how the secondary gas injection geometry effectively breaks the liquid film. By varying the ratio of the primary and secondary gas flow rate, the newly detached droplet can be steered to the same or opposite wall as the approaching liquid film.

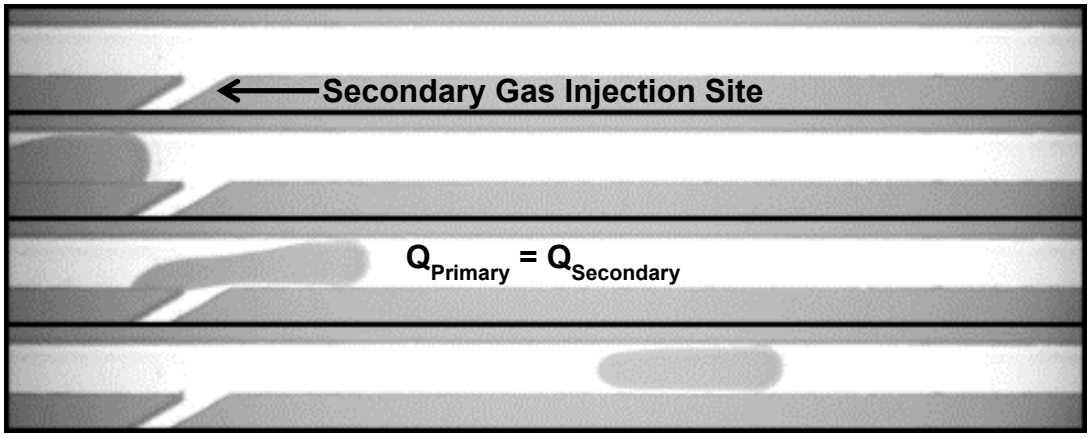

Figure 24. A series of images showing how the secondary gas injection geometry effectively breaks the liquid film. Using equal primary and secondary gas flow rates detaches and entrains the droplet down the center of the channel.

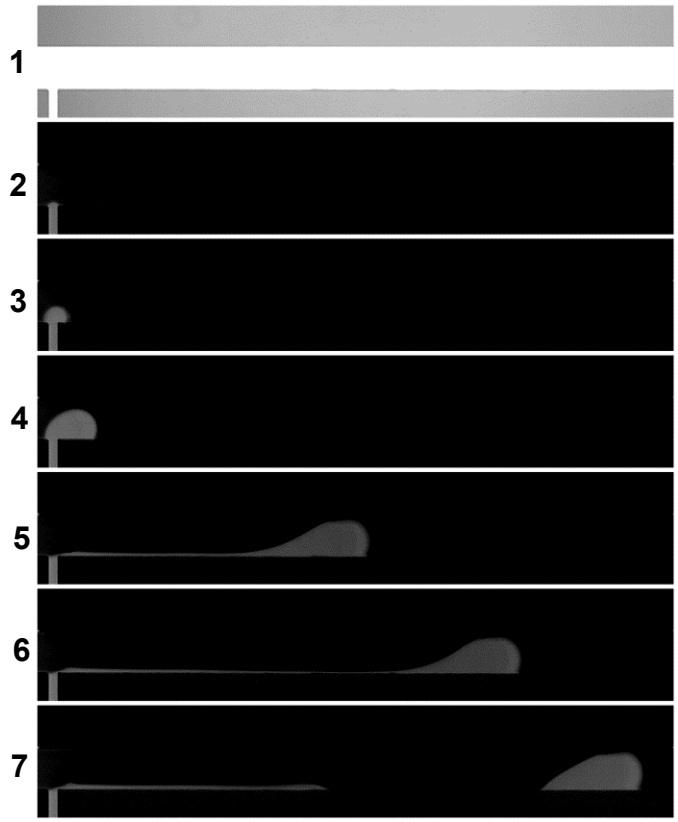

Figure 25. Series of images showing how the film is suppressed using a pulsed liquid solenoid valve. White light image showing the T-junction geometry (1), fluorescent images showing the emergence of liquid at injection site (2 – 4), liquid issues from injection site and leaves a film (5 – 6), and rupturing of film when solenoid valve closes (7).

2.3 Droplet Volume and Generation Rates

Droplet volumes and detachment frequencies have been recorded for both T-junction and flow focusing geometries. Unlike oil-liquid droplet generation, there is a narrow operating window where droplets can be generated. The operating window is based on the ratio of gas to liquid driving pressures. The most direct method for controlling the detached droplet volume and frequency was by changing the gas and liquid driving pressures while maintaining the same pressure ratio. Regardless of the detachment

geometry, increasing the *Reynolds* number of the gaseous flow reduced the volume of the detached droplet and increased the rate at which droplet were generated.

The technique used to measure droplet volume and frequency was based on image processing using custom MATLAB™ script and function files. The program files scan through thousands of image frames to locate and measure droplet size and frequency of occurrence. The series of images in Figure 26 illustrate the image processing operation. The first image shows the flow focusing channel geometry and the second image shows a droplet. The droplet is identified by removing the image background, as shown in the third image, and converting the intensities to binary values, as shown in the fourth image. The number of non-zero pixels, size of each pixel, and depth of the microchannel determine the droplet volume. Frequency information is revealed by calculating the time between each droplet. The plot in Figure 27 show representative results of this analysis. This was obtained for a flow focusing geometry shown in Figure 26.

Size and frequency dispersion is based on the ratio of the standard deviation to the average value. Results obtained to date show that size and frequency dispersion was minimized by using flow focusing geometries. The smallest dispersion measured across all devices and data sets was 0.2% and was obtained using the converging-diverging flow focusing geometry in Figure 5 and Figure 26. Size dispersion begins to increases as the pressure ratio increases. The highest frequency obtained for flow focusing devices was 72 Hz. In general, higher frequencies are obtainable using T-junction devices that employ film suppression techniques. The highest droplet frequency, 527Hz, was achieved using the secondary gas injection geometry shown in Figure 23. The dispersion in frequency, however, was over 10%. The largest throughput was 18μL/min and was achieved using a standard T-junction geometry with the liquid solenoid valve operating at 10Hz with a 25ms pulse width.

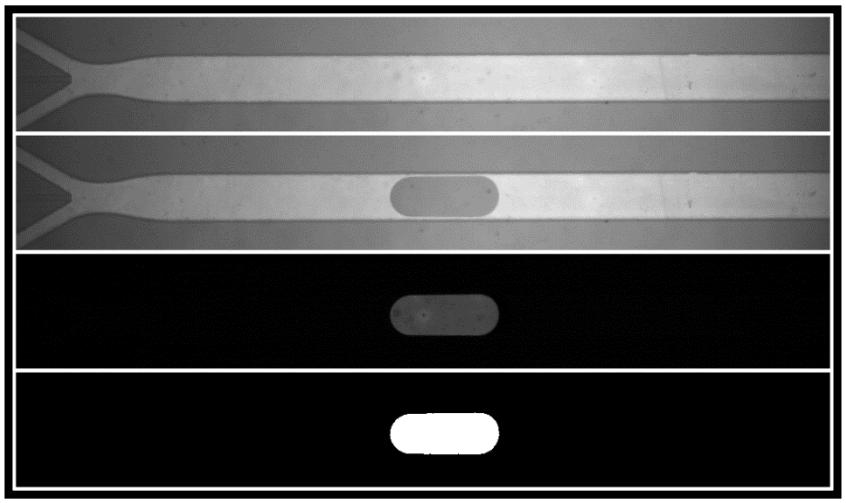

Figure 26. A series of images that highlight the image processing operations used to find droplet volume and frequency statistics. The first image is used for background removal. The result is a high contrast image that helps locate the presence of a droplet, as shown in the third image. The last image is the binary image that results from intensity thresholding.

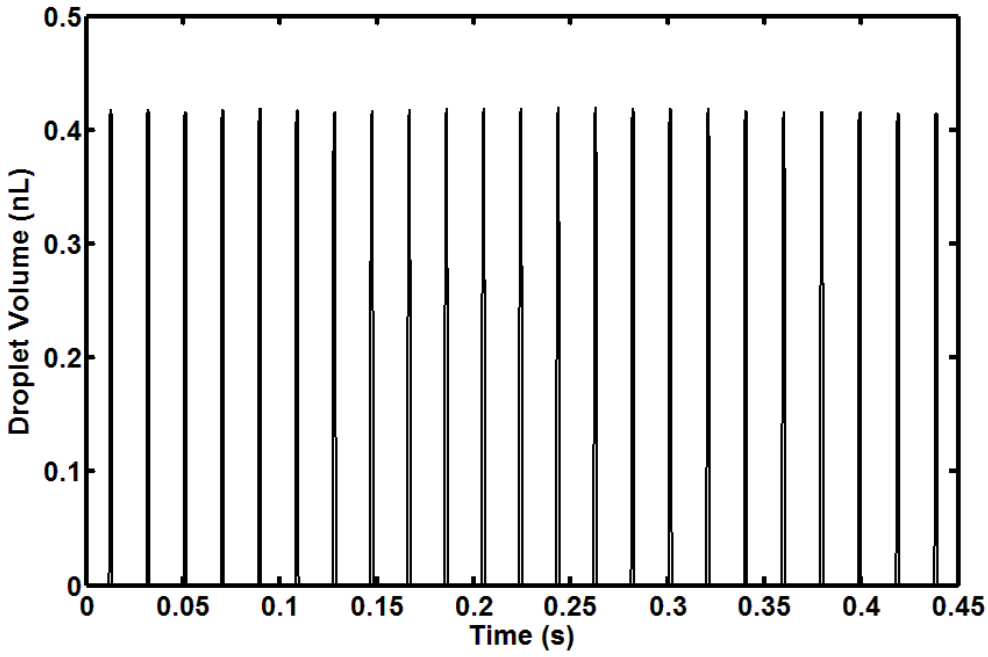

Figure 27. A plot showing the results of the image processing operation for measuring droplet volume and generation frequency. Spikes in the signal indicate the passing of a droplet. The peaks of the signal and the time of occurrence are used extracted volume and frequency statistics.

2.4 Summary of Research Accomplishments

- Experimentally determined the dominate detachment mechanism for creating droplets in a high speed gas flow transitions static pressure forces to inertial forces near a gas Reynolds number of 100.
    - A paper detailing this work is currently under consideration in the *Journal of Fluids Engineering*
- Developed a film mitigation technique for T-junction detachment geometries based using a variable frequency solenoid valve. Also verified single-shot operation for creating single droplets on demand.
- Repeatably generated nano-liter droplets, with less than 1% size dispersion, in a confined microchannel using a gaseous continuous flow. There are no results available in the published literature that describes such small size dispersion for gas-liquid flows.

CHAPTER 3

DEVELOPMENT OF AN INERTIAL MICROMIXER

This chapter describes the merits, mixing predictions, and fabrication processes of a new class of microfluidic devices that provides millisecond mixing times of nano-liter droplets through inertial interactions. The over-arching goal leading to its development is the need of an innovative mixing technique that is passive and non-energy intensive, portable and robust, easily integrated into existing systems, and capable of autonomous operation. Device fabrication must be simple (2D) and straight-forward (soft lithography) and employ chemically inert materials (polydimethylsiloxane). When viewed according to any single facet of operation, device functionality of this droplet collision micromixer is not unique. Generating liquid droplets in unconfined environments using a high speed gas flow was thoroughly investigated, clearly demonstrated, and unquestionably perfected by Lefebvre et al. for polydisperse applications (Rizkalla and Lefebvre 1975, Lefebvre and Chin 1985, Lefebvre 1989) and later by Ganan-Calvo for monodisperse applications (Ganan-Calvo 1998, Ganan-Calvo and Barrero 1999, Ganan-Calvo 2008). Interest and work on liquid droplet detachment in confined microchannel geometries using an immiscible liquid continuous phase has been well represented over the past decade in journals and conferences pertaining to microfluidics. See, for instance, the work of Stone and colleagues (Stone and Leal 1990, Anna et al. 2003, Link et al. 2004, Garstecki et al. 2006). Prior to the commercial fruition of microfluidics, Simpson et al. showed that sub-millisecond mixing times for nanoliter droplets were possible through high speed collisions in unconfined environments (Simpson, et al. 1983, Simpson, et al. 1986). Nilsson et al. transported and collided droplet pairs on an exposed super-hydrophobic surface using gas nozzle for enhanced mixing studies (Nilsson and Rothstein 2012). Liu et al. used a gaseous cross-flow to intensify mixing in forming droplets for nano-particle preparation (Liu et al. 2010). What makes this work novel and

unique is that it combines many of the salient features above into a single device. A high-speed gaseous flow creates and transports discrete droplets at speeds near 1m/s. Droplet collisions are employed to yield sub-millisecond mixing times for 100 nL droplet volumes. This inertial mixing technique extracts the kinetic energy carried by each droplet prior to impact and viscously dissipates the excess energy through internal volumetric rearrangement that rapidly reduces the effective diffusion length.

3.1 Experimental setup

The quality and confidence of any result obtained by experiment is greatly sensitive to the measurement techniques and equipment employed. Starting from the ground up, a custom microfluidic test bed has been designed for experimental investigation of multiphase flows, particularly high speed gas-liquid droplet flows, with unparalleled precision. Hardware diagrams of the gas and liquid flow control is shown in Figure 28. Figure 29 illustrates how the camera, lasers, and solenoid valves are synchronized. The power, data, and signal transmission for the setup is shown in Figure 30. The item numbers referenced in the text below correspond to the item numbers listed in the hardware diagrams. Actual photos of the setup are shown in Figure 31.

The test bed is capable of providing gas flow control from 10^{-8} to 10^{-6} m^3/s with 10^{-9} m^3/s precision (0.5 to 100 sccm with 0.1 sccm) and liquid delivery pressures from 1.4 to 140 kPa with 0.1kPa stability (0.2 – 20 psi +/- 0.01 psi). This is accomplished using a voltage-controlled pressure regulator (Proportion-Air QPV1, item #5) with pressure transducer feedback control. Flow rates are measured using thermal mass flow sensors (Sierra Smart-Trak2, item #7). For tests where air is used as the continuous phase, facility supplied compressed air (item #1) is first dried in a desiccant chamber (item #2) and cleaned using 0.2μm filters (item #3). A rough pressure regulator (item #4) is used to reduce the facility pressure before routing the air flow into a delivery manifold. Individual and multiple air streams are activated using the voltage-controlled pressure regulators (item #5).

Liquid flow control is provided by a custom pressurized liquid reservoir (item #6) and fast switching solenoid valve (Parker - Series 3, item #8). This arrangement was designed for droplet generation purposes where the feature of utmost importance is flow stability. The conventional workhorse for microfluidic liquid delivery is a constant displacement pump driven by digital encoder motor. These types of pumps are inherently unstable in terms of pressure response. For gas-liquid droplet generation, there is no viscous continuous phase to dampen these instabilities and the effects become amplified. The result is unpredictable droplet sizes and unsteady generation rates that show multiple frequency contents. The solenoid valve can be used with frequencies between 0.05 to 40Hz and duty cycles from 5 to 100%. The resulting liquid flow rate can then be delivered with precision by changing the reservoir pressure, switching frequency, and duty cycle, thereby providing complete control over liquid delivery rates. Furthermore, the valve is capable of a single-shot driving pulse for droplet-on-demand operation. The liquid solenoid valves were powered using a 24V DC power supply. A delay generator (Stanford Research DG645) was provided the driving frequency and opening pulse width of the solenoid at TTL levels. A Darlington transistor, with 12V at the collector, pulse TTL at the base, and solenoid at emitter, was used for switching the 800mA solenoid load. For test where only single shot operation is needed, the solenoid is activated using only a switching relay. A schematic of the liquid solenoid control circuit is shown in Figure 29. Development of this liquid delivery system was invaluable for the droplet detachment and mixing results to follow.

Visualization of droplet dynamics is provided by an inverted microscope (Nikon Ti-U) with a high-speed camera (Photron SA-5). The camera runs a 1024x1024 CMOS sensor with 20μm square pixels and is capable of frame rates in excess of 1Mfps at reduced spatial resolution. Image exposure is limited by the image frame rate, but can be as low as 3μs. The exposure time is ultimately determined by the amount of light available. When imaging in white light mode, such as that used for droplet detachment studies, the camera exposure can be arbitrarily small. A white light source is insufficient, however, for mixing diagnostics. For mixing experiments, a high repetition 532nm

Nd:YAG laser is employed (Quantronix Hawk Duo). This is a dual cavity laser and capable of 40 kHz operation. The pulse width of the laser depends on repetition rate but is near 100ns. In order to synchronize the laser pulse with the camera imaging rate and exposure, a delay generator is used (Stanford Research DG645) as the master clock. Since the camera frame rate is twice the frequency of the laser, a frequency dividing circuit was built and interfaced between the delay generator and each laser cavity. The driving current needed to trigger each laser is provided by a 5V DC power supply and routed through a Darlington transistor array with the frequency divided signal at the emitter terminal. A schematic of the synchronization circuit is shown in Figure 29.

All pressure regulators, transducers, and flow meters were powered using dedicated 24V DC power modules and activated through dedicated relay switches inside a data logger/switch unit (Agilent 34970A). The data logger also monitors flow rate and pressure data for the gas and liquid streams. The gas pressure regulators are controlled using a 4 channel DC power supply (HP 6627A). All power and data transmission cables are shielded and grounded and an Amphenol bulk-head connectors umbilical the test setup to the power and control equipment. A dedicated host computer running Labview™ provides user control and data visualization through a custom *VI*. GPIB data protocol is used for communication between host computer and instrumentation. A schematic of power, signal, and data transmission used for control and measurement is shown in Figure 30.

The spatial resolution of this experimental setup is determined by the microscope objective used for magnification, the physical size of the camera imaging sensor, and the exposure time used to capture the images. The microscope objective used for these experiments provides an in-plane and out-of-plane spatial resolution of 0.67 and 3.4μm, respectively. The physical size of each pixel on the imaging sensor is 20μm, which, at 20x magnification, provides an in-plane spatial resolution of 1μm. The exposure time controls how long the imaging sensor is gathering intensity data for each image. As the exposure duration is increased, the image intensity increases proportionally but highly

dynamic events become blurred and difficult to resolve. The in-plane spatial resolution is therefore the product of the anticipated system velocity and exposure duration. For example, capturing a particle traveling at 1m/s with an exposure of 1μs provides an in-plane spatial resolution of 1μm. The resulting in-plane spatial resolution of the measurement system is the maximum of these three sources. For the results presented in the following section, the in-plane spatial resolution was undoubtedly limited by the camera pixel size and ranged from 1 to 2μm depending on the objective magnification used. The short pulse width of the laser can resolve droplet velocities in the 10m/s range before exceeding the camera pixel size. The temporal resolution of this measurement system is determined by the laser repetition rate, which is limited to 40 kHz. The resulting temporal resolution is therefore 25μs.

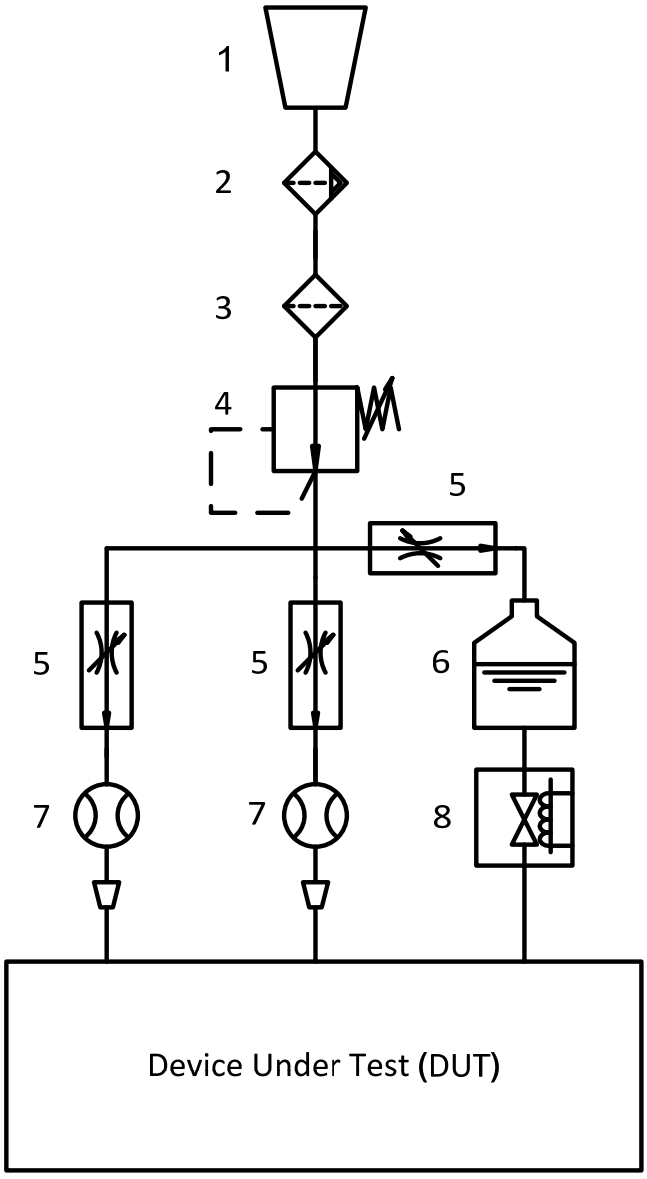

Figure 28. Schematic of hardware and instruments for gas and liquid flow control: facility compressed air supply (1), desiccant dryer (2), sub-micron particulate filter (3), rough pressure regulator (4), pressure regulators with transducer feedback control (5), sealed liquid reservoir containing reactants to be mixed (6), mass flow sensors (7), miniature inert solenoid valve (8), and microfluidic device under test (DUT).

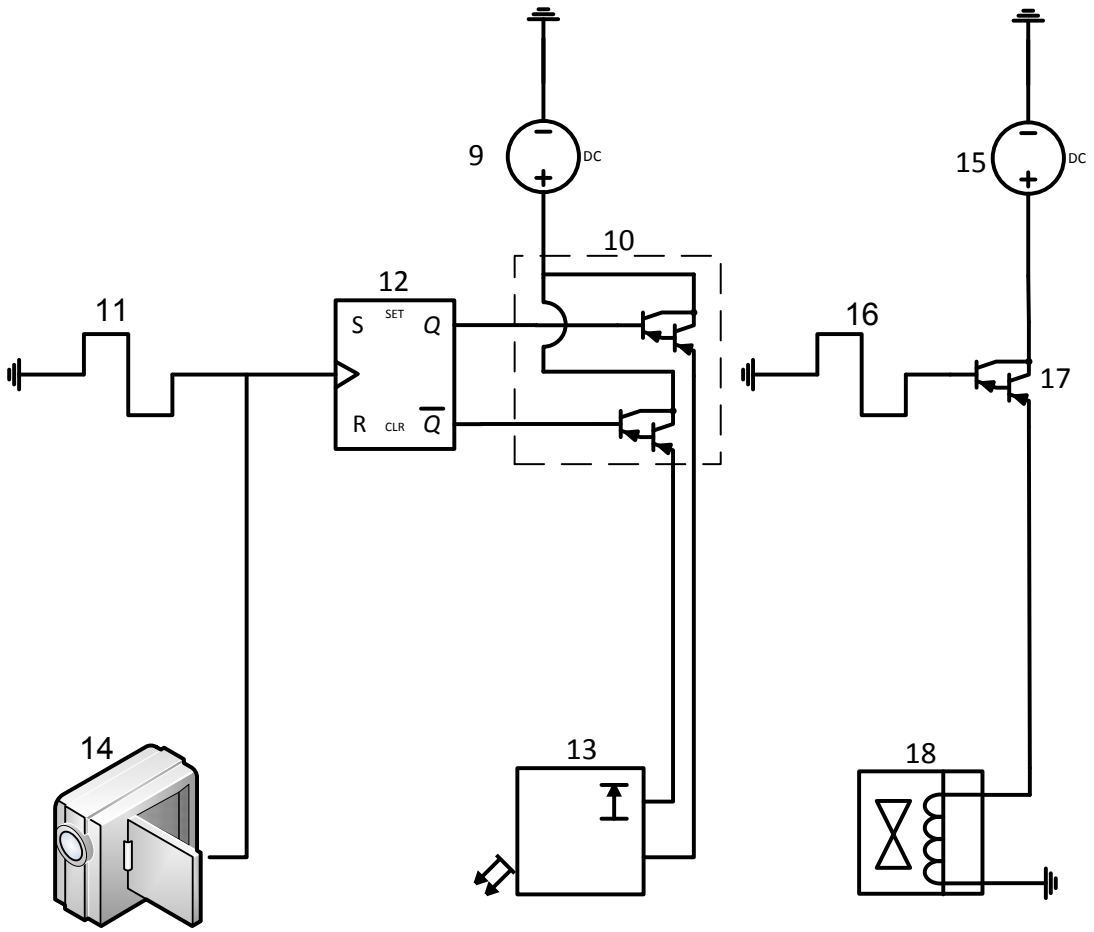

Figure 29. Schematic showing synchronization of camera and laser for image acquisition and triggering of liquid solenoid valve: 5V DC power supply (9), Darlington transitor array (10), delay generator for camera (11), logic gate used as a frequency divider (12), dual-cavity pulse Nd:YAG laser (13), CMOS camera (14), 12V DC power supply (15), delay generator or oscillating circuit for liquid solenoid (16), Darlington transistor (17), liquid solenoid valve (18).

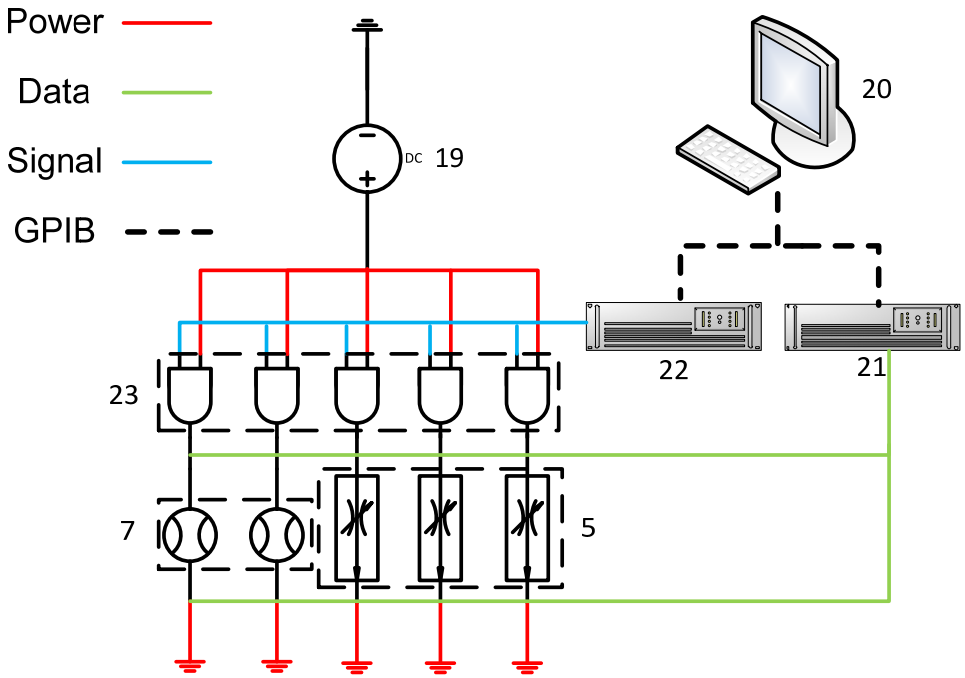

Figure 30. Schematic of power, data, and signal transmission for the microfluidic test bed: 24V DC (19), host computer (20), data logger (21), controllable power supply (22), and switching relays (23).

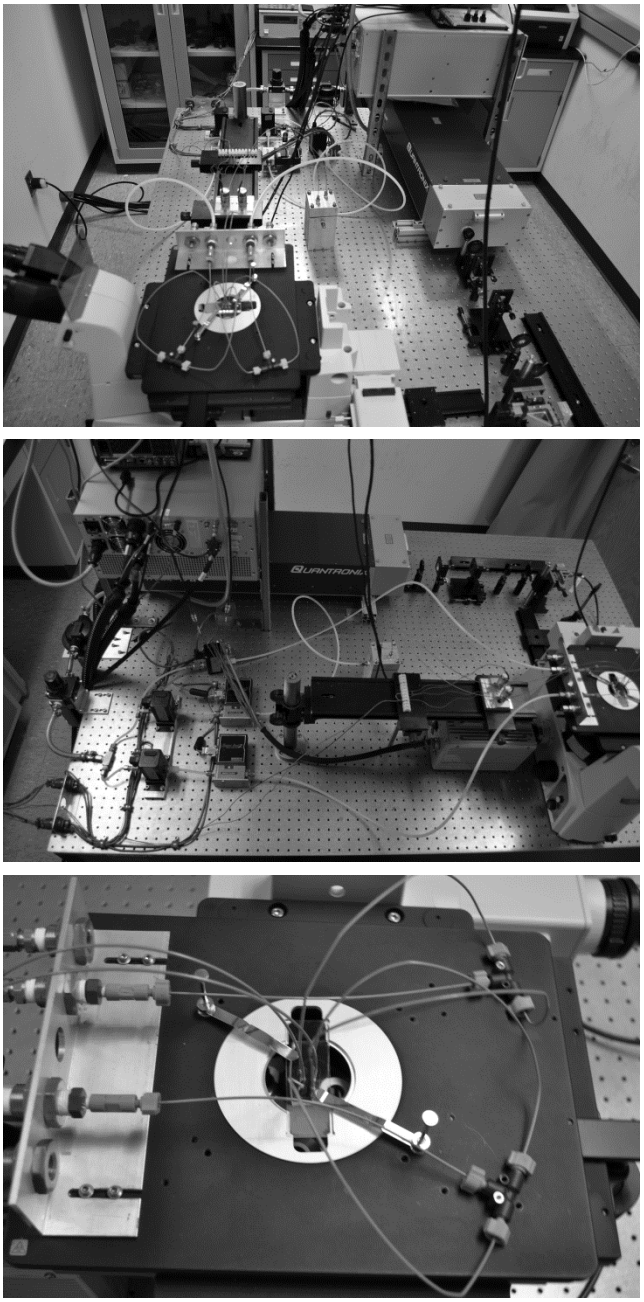

Figure 31. Photos of microfluidic test bed showing inverted microscope, laser and beam conditioning optics, gas and liquid delivery hardware, and pressure and flow transducers all secured to a floated optical table. The lower photo shows the droplet collision mixing device secured to microscope stage with gas and liquid tubing installed.

3.2 Device Fabrication

The micro-fabrication process is based on conventional, 2D soft lithography techniques using polydimethylsiloxane (PDMS) as the substrate material. The process flow shown in Figure 34 below depicts the major fabrication steps. The process begins by creating a negative mold of the microchannel geometry on a standard 4" diameter, 500μm thick silicon substrate using photolithography. The wafer is cleaned and prepared using standard cleaning procedures. A negative near UV resist (SU8-2050 MicroChem Corp.) is spin coated onto the wafer to a thickness dictated by the microchannel depth. The coated coated wafer is then baked to remove the solvents in the resist. Once cured, the wafer is placed in a Karl Suss MA6 mask aligner and exposed to 392nm radiation through a mask containing the microchannel image. Since the smallest feature size on the microchannel is typically 20μm, a photo-plotted, 7mil film mask is used as an alternative to a chromium mask. The exposed wafer is then developed using the appropriate developer solution and baked at the prescribed temperature and duration.

Following the photolithography process, the resist-coated wafer is treated with trichlorosilane in a reduced pressure environment for approximately 4 hours. This process renders the silicon surface hydrophobic and facilitates mold release. The PDMS solution is prepared using Sylgard 184 silicone elastomer base mixed with a curing agent at a 5 to 1 weight ratio. Unlike the 10 to 1 ratio recommended by the manufacture, the increase curing agent produces finished devices that are significantly more rigid. The PDMS solution is poured onto silicon mold and the assembly is placed in a vacuum desiccator to remove trapped air bubbles and promote solvent vaporization. The assembly is then placed on a hot plate in ambient surroundings and baked at 65^{o}C for approximately 3-6 hours. Once cured, the PDMS is peeled from the silicon substrate.

The available real estate on a 4" silicon wafer allows a number of devices to be created in a single soft lithography process. Each device is cut from the PDMS mold and prepared for fluid and gas porting. A 2mm diameter belt-hole puncher is used to core the PDMS device at each gas and fluid inlet and outlet. The core is removed using tweezers.

Each device is then cleaned with methanol and prepared for bonding. A 1"x3" standard microscope slide is spin coated with a ~5μm thick layer of PDMS using a 10 to 1 weight ratio. The glass slide provides a rigid substrate to support each device to and allows bottom up visualization using an inverted microscope. The uncured slides are placed in the vacuum desiccator for 1 hour and then placed on a hot plate at 55^{o}C. Before the PDMS is fully cured, a clean device is carefully placed on its surface. The combination of different mixing ratios promotes diffusion between the device and substrate resulting in a permanent bond that is stronger most other PDMS bonding technique. Pressures in excess of 20psi have been introduced into these devices without failure.

3.3 Description of Operation

Referring to the simplified schematic in Figure 32, continuous liquid streams are introduced at two locations denoted by as the "*Liquid Injection"* sites. Each liquid stream is discretized into droplets by a high speed gaseous flow at the "*Detachment"* sites. The gas flow accelerates and transports two opposing droplets to the *Collision Zone*. The droplets collide, coalesce, and mix before being removed at the *Product Removal* site. During the collision, the kinetic energy of each droplet is viscously dissipated through complex particle motions and bulk volumetric rearrangement. The result is near millisecond mixing for nanoliter sized droplets.

A number of collision geometries were investigated before the Y-type junction was selected. When a droplet approaches the junction, the effective flow area increases resulting in reduced drag force. The droplet becomes pinned at the apex by surface tension and will remain there until the gas drag force overcomes the surface tension force. Once a collision occurs, the surface area of the newly coalesced droplet nearly doubles and surface tension is now unable to keep the larger droplet pinned at the apex. The mixed droplet is removed and the junction is readied for the next droplet pair. This is shown in the series of experimental images in Figure 33. A single droplet is pinned at the apex and a second droplet approaches from the lower left. Shortly following the collision,

the new droplet detaches and exits the collision zone. Droplet pinning at the apex is relaxes the collision timing such that droplets that are detaching out of phase are still collide and mix. This process is invaluable for studying mixing dynamics as the probability of a collision is greatly increased.

3.4 Summary of Research Accomplishments

- Developed a microfluidic test bed capable of providing and controlling multiple gas and liquid feeds with enhanced stabilities.
- Gas delivery system is capable of providing flow rates from 10^{-8} to 10^{-6} m^3/s with 10^{-9} m^3/s precision.
- Fluid delivery system is capable of injecting multiple liquid streams with driving pressures from 1.4 to 140 kPa with 0.1kPa stability.
- Designed, built, and tested a new mixing device that uses a high *Reynolds* number gaseous flow for droplet generation and transport and uses droplet collisions for fast mixing rates.
- Discovered how to use surface tension to pin a single droplet at a Y-junction to provide a collision target for an opposing droplet. This technique significantly increases the probability of droplet collisions and greatly simplifies timing issues.
- Developed a fabrication technique that improves bonding integrity. The technique uses modified material mixture ratios and partially-cured bonding PDMS to PDMS bonding. The result is a significantly more rigid elastomeric device that can with stand operating pressures 10 fold greater than traditional methods.

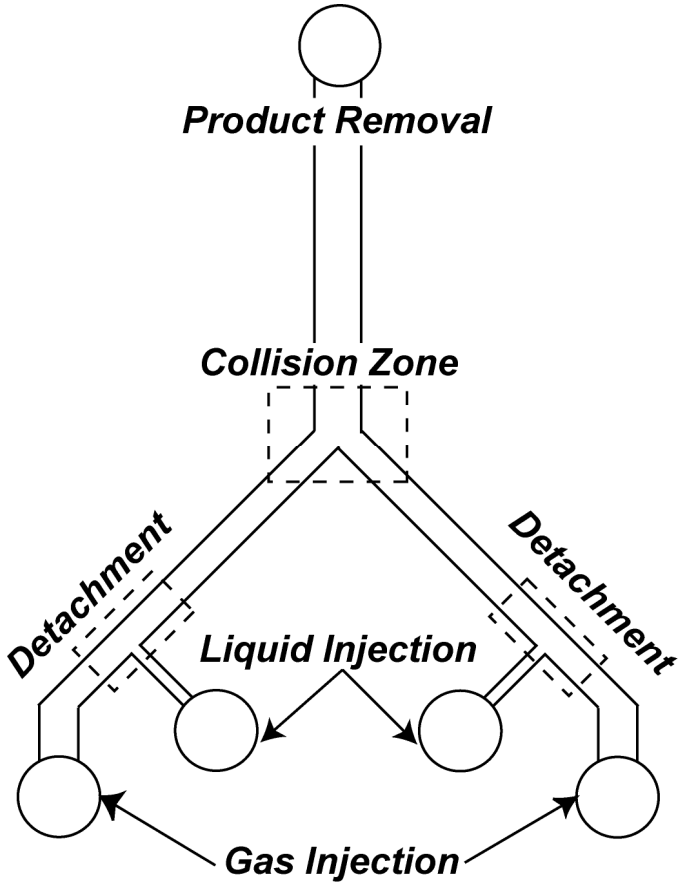

Figure 32. Simplified schematic of the inertial mixing device. A high speed gas flow is introduced at the *Gas Injection* site and liquid is introduced at the *Liquid Injection* site. The liquid stream is discretized into droplets by the gas flow at the *Detachment* site. Droplets are transported by the gas flow to the *Collision Zone* where two opposing droplets collide, coalesce, and mix. The mixed droplet is removed from the device at the *Device Removal* site.

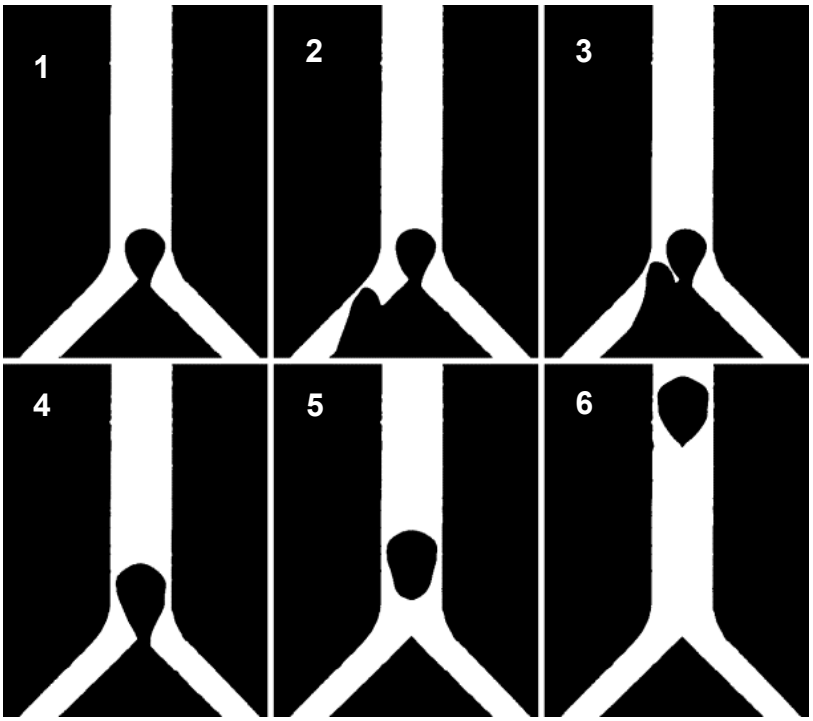

Figure 33. Series of high speed images showing the droplet pinning, collision, and removal process: single droplet is pinned at the Y-junction apex (1), opposing droplet enters frame from lower left (2, 3), droplets collide, coalesce, and mix (4), and droplet is unpinned and removed from collision zone (5, 6). Note: the grayscale images have been converted to binary images to improve contrast.

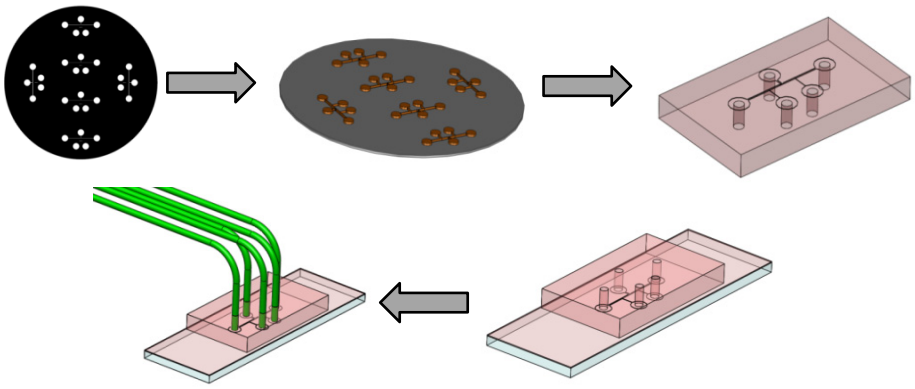

Figure 34. Process flow for PDMS soft lithography: mask CAD design, photolithography, molding, bonding, and fluid and gas port integration.

CHAPTER 4

SINGLE-FLUOROPHORE LASER INDUCED FLUORESCENCE FOR MIXING DIAGNOSTICS

The difficulty in quantifying the extent or degree of mixing is that there is no unifying theory that clearly distinguishes a "fully mixed" condition. Some (Ottino 1989, 1990, Dutta and Chevray 1994, 1994, Ottino and Wiggins 2004) have applied a Hamiltonian perspective to chaotic mixing that describes well mixed conditions if every particle explores the mixing domain while losing track of each other. This idea of particle divergence is the foundation of chaotic mixing, a concept first pioneered by Aref (1984). This purely dynamical approach to mixing is well suited for low Reynolds number, high Peclet number flows, where the inertial terms are neglected in the momentum transport equation, all transient effects are piecewise steady, and mass transport by diffusion is neglected. Chemists describe well mixed conditions by the degree in which a chemical reaction takes place, since a reaction cannot proceed unless there are molecular interactions between the reactants (Kling and Mewes 2010). This requires molecular scale proximity. The turbulence community predicts mixed conditions based on the homogenization of a scalar field, such as concentration or temperature (Dimotakis et al. 1983, Koochesfahani and Dimotakis 1986, Dimotakis 2005). If homogenization is poor at the large scale, mixing at the molecular scale will be highly localized and largely poor throughout the volume. If homogenization is complete at sub-system length scales, mixed conditions at the molecular scale, although not guaranteed, may be safely assumed. A mixing system displaying fast homogenization rates at these intermediate, sub-system length scales therefore provides molecularly mixed conditions faster than a similarly scaled system displaying slow homogenization rates. Thus, quantifying the extent of mixing based on tracer homogenization provides an important metric in mixing system design and a benchmark for system performance.

In the sections to follow, an optical diagnostic technique is presented that employs single-fluorophore Laser Induced Fluorescence (LIF), meaningful mixing statistics, and custom image processing to quantify and visualize the extent of mixing in confined droplet collisions. A review of the current state-of-the-art in mixing diagnostics is presented first to show the inadequacy of available diagnostic techniques when applied to high-speed droplet mixing. LIF fundamentals are then briefly reviewed to highlight the salient features of using fluorescence signals for mixing diagnostics. Spatial mixing statistics are then reviewed and a new metric is introduced that captures the effective length scale reduction provided by convective rearrangement. The optical diagnostic topic concludes by discussing two subtle yet critical image processing techniques for intensity corrections and droplet volume tracking.

4.1 Review of Mixing Diagnostics

The fast time scales, small length scales, and largely Lagrangian nature of advanced droplet mixing techniques makes optical diagnostics the obvious choice for understanding, characterizing, and quantifying mixing. Within this tool box, three major techniques have been successfully demonstrated: infrared absorption (IR), spontaneous Raman scattering (SRS), and LIF. IR techniques measure the wavelength and intensity of mid-infrared (2.5-50μm) light absorbed by a sample. Energy provided by the light source excites molecular vibrations to higher energy levels resulting in absorption bands that are characteristic of specific types of chemical bonds. SRS is an inelastic radiative scattering process that operates on the short lived "virtual" states and subsequent Raman shift. Both IR and SRS provide molecular fingerprints of chemical species present in the investigation region such that the local concentration, and hence degree of mixing, is resolved. LIF is also an inelastic radiative process but is based on the absorption and subsequent emission of a photon following quantum energy state interactions. By controlling environmental conditions and using spectral filtering, the LIF signal is

proportional to participating specie concentration and mixing is inferred based on the intensity of the received signal.

The advantage and limitation of each method rests on the process being investigated. Both IR and SRS suffer from small collision cross-sections and therefore produce low signal intensities unless high power lasers are used. Furthermore, IR has the disadvantage of line of sight averaging where the received signal is axially integrated. SRS requires a high degree of laser rejection in order to separate the weak, inelastically scattered Raman light from the intensely scattered Rayleigh light that lies close to the laser line (Schrader et al. 1991). Additionally, IR and SRS are a point or line based process and a special setup is required to acquire information in two dimensions (Masca et al. 2006, Jendrzok et al. 2010). LIF, on the other hand, readily provides intensity information across a plane and, depending on the optical systems used, only weakly integrates the third dimension. Compared to IR and SRS, LIF provides a significantly greater collision cross section such that the excitation energy required for a detectable signal is significantly less and in many cases a conventional white light source is sufficient. The difficulty in discerning mixing information based on LIF intensity measurements is that the fluorescent emission signal may be highly dependent on environmental conditions, such as temperature and pressure; mixture conditions, such as pH; and excitation source stability, such as temporal and spatial non-uniformities. These variables attenuate and skew the concentration-dependent signal such that mixing information is lost or misleading. However, for investigating mixing in microfluidic devices, LIF remains the most suitable method given the small length and time scales and ease of system integration.

LIF has heritage in many diverse science and engineering applications. Initial success as a laser dye was quickly advanced to a method for studying molecular collisions and quantifying molecular concentrations with detection efficiencies comparable to mass spectrometers at that time (Kinsey 1977). Over the past four decades, LIF has evolved into an invaluable optical diagnostic tool. It has allowed investigation of complex structures not possible using other visualization techniques, such as mixture composition

in reacting and non-reacting shear layers (Koochesfahani and Dimotakis 1986), turbulent jets (Dimotakis, et al. 1983), and combustion processes (Matsumoto et al. 1999). LIF allows spatial resolutions greater than the diffraction limit of light in microscopy systems through Förster Resonance Energy Transfer (FRET) and, as a result, has opened up new opportunities in microbiology previously unachievable (Quercioli 2011). The often complex dependence of fluorescent intensity to mixture composition and environmental conditions has allowed LIF measurements of temperature (Anderson et al. 1998, Coppeta and Rogers 1998, Lavieille et al. 2001, David et al. 2006), pressure (Hiller and Hanson 1988), pH levels (Bellerose and Rogers 1994, Coppeta and Rogers 1998), film thickness (Coppeta et al. 1996, Hidrovo and Hart 2001), velocity distribution functions (Jacobs et al. 2007), and molecular level mixing (Bellerose and Rogers 1994, Faes and Glasmacher 2010, Kling and Mewes 2010). The LIF application applied here is the time resolved microscopy visualization of the spatial concentration field for quantifying mixing. The focus is on passive mixing, where the flow is unaffected by the scalar field yielding *Level 1* type mixing (Dimotakis 2005).

4.2 Technique Fundamentals

Since the emphasis of this section is using LIF to extract mixing information in colliding droplets, only a brief, top-level account of the salient features of the LIF process is provided. The reader is referred to Arbeloa (1998, 2005) for highly detailed photo-physical and chemical descriptions and Quercioli (2011) for a comprehensive review of fluorescence and its applications in modern microscopy. Fluorescence occurs when a specific type of molecule, called a fluorophore, is excited by a photon and undergoes inelastic rotational and vibrational losses before emitting a photon of longer wavelength and returning to the ground state. Photon emission can be reduced, entirely suppressed, or spectrally altered through non-radiative quenching processes. Such processes include imposed chemical reactions (Ware 1962, Knight, et al. 1998, Kling and Mewes 2010), self-quenching due to collisions with like molecules (MacDonald 1990) or concentration-

dependent bathochromic shift in the fluorescent band (Arbeloa, et al. 2005). For the diagnostic technique presented here, no chemical reactions are imposed or considered and only the self-quenching process is recognized as a possible path for fluorescent attenuation.

As light propagates through a participating medium its intensity decays with distance. The rate of decay is dependent on the spectral properties of the incident light and absorption properties of the participating medium. Water, for instance, preferentially absorbs longer wavelength red light to a greater degree than shorter wavelength blue light. In the case of a fluorescing substance, the absorbed shorter wavelength intensity is released as longer wavelength fluorescence. However, the process is inelastic and only a fraction of the absorbed excitation energy is emitted as fluorescence. The quantum yield of the process is the ratio of emitted fluorescence intensity to absorbed excitation intensity. To help illustrate this process, consider the control volume shown in Figure 35 consisting of a fluorescing fluid of infinite height and depth but finite length x. As the excitation light propagates through the volume, there is a decrease in intensity with distance due to specie absorption. The decrease in the excitation intensity I_{Ex}, is manifested as an increase in fluorescent intensity I_{Em}, the ratio of which is related to the quantum efficiency, Ψ, of the process:

$$\frac{I_{Em,Out} - I_{Em,In}}{I_{Ex,Out} - I_{Ex,In}} = -\frac{dI_{Em}}{dI_{Ex}} = \Psi \qquad \textbf{11}$$

The change in excitation intensity is related to the concentration c and extinction coefficient ε of the absorbing specie and decays exponentially with distance x into the participating medium. The ratio of the excitation intensity at some distance x, $I_{Ex,x}$, to the incident intensity at $x = 0$, $I_{Ex,0,}$ is expressed by Lambert-Beer's law:

$$\frac{I_{Ex,x}}{I_{Ex,0}} = \exp(-\varepsilon c x) \qquad \textbf{12}$$

For an aqueous solution with constant extinction coefficient, the change in intensity is determined by:

$$dI_{Ex,x} = -\varepsilon I_{Ex,0} \exp(-\varepsilon c x)(c dx + x dc) \quad \textbf{13}$$

If the physical length is maintained constant at an interrogation depth l, the change in intensity is determined only by the fluorophore concentration:

$$dI_{Ex} = -I_{Ex,0} \varepsilon l \exp(-\varepsilon c l) dc \quad \textbf{14}$$

Cast in these terms, the concentration is appropriately non-dimensionalized by a characteristic system concentration $c_{ch} = 1/\varepsilon l$:

$$dI_{Ex} = -I_{Ex,0} \frac{1}{c_{ch}} \exp\left(\frac{c}{c_{ch}}\right) dc = -I_{Ex,0} \exp(-c^*) dc^* \quad \textbf{15}$$

The ratio of the actual concentration to the characteristic system concentration, c^*, is traditionally labeled as the optical thickness of the system. When the optical thickness is much less than unity, optically thin conditions exist and the change in intensity is approximately linear with concentration. An optical thickness much greater than unity provides optically thick conditions and changes in intensity are non-linear with concentration. Substituting Equation 45 into Equation 41 and integrating gives the following for the fluorescent emission intensity as a function of c^*:

$$I_{Em} = \Psi I_{Ex,0} \left[1 - \exp(-c^*)\right] \quad \textbf{16}$$

Equation 6 is now linearized with respect to c^* to provide a direct link between fluorophore emission and concentration for constant incident excitation intensity:

$$c^* = -\ln\left(1 - \frac{I_{Em}}{\Psi I_{Ex,0}}\right) \quad \textbf{17}$$

Equation 47 provides a spatial concentration map for each captured image and a snap shot of mixing progress. Mixing is determined complete when the droplet intensity, and

hence concentration, is uniform throughout. The absolute concentration, which can be determined by careful calibration of Equation 47, is unimportant in establishing the state of mixedness.

To test the applicability of Equation 46, a 230μm deep microchannel containing different concentrations of Pyrromethene 556 dissolved in distilled water was imaged. This fluorophore was selected for its spectral properties, photo-stability, excellent water solubility, and non-existent tendency to diffuse into the PDMS substrate. Other dyes considered, such as the Rhodamine family, diffuse into the channel walls and increase the background noise level. Data in the literature indicates a quantum yield of 0.73 and an extinction coefficient of $7.2 \times 10^4 cm^{-1}/M$ (Shah et al. 1990). Using these properties and the optical interrogation depth, the change in fluorescent intensity with concentration is predicted using Equation 46. The plot in Figure 36 compares analytical predictions to measured experimental data. There is acceptable agreement up to $c^* \sim 2$. Past this value, higher order effects that are not captured by the simple analytical model can no longer be neglected. Furthermore, the signal must be monotonic in order to infer relative concentration distributions. This sets an upper limit on the maximum droplet optical thickness at $c^* \sim 2$.

Using digitized images to quantify mixing demands that the captured LIF signals are representative of the tracer concentration field. Generating an accurate fluorophore concentration map requires separation of the fluorescent emission from the fluorescent excitation as wells as any background noise present in the experimental system. The absorption-emission spectrums of the most common scientific fluorophores are similar in shape but display different Stokes shift lengths (color shift) and excitation and emission spectra broadening. Most commonly available fluorophores display a region where the absorption and emission bands overlap, as shown in Figure 37 for Pyrromethene 556 (Exciton). In this region, the emission signal is re-absorbed and subsequently re-emitted and does not follow the behavior described by Equation 46. Signals from this wavelength range should not be included in intensity statistics. Note that the maximum absorption

and emission peaks lie in or very close to the overlap region such that operating near these maxima is not always possible. For such conditions, it is recommendable to excite at a shorter wavelength than maximum absorption, especially if the Stokes shift is comparably narrow and there is severe spectra overlap (Borlinghaus 2011).

Proper selection of filters and mirrors ensures that the captured signal has not been attenuated by the reabsorption-emission process or generated by sources within the experimental setup. This is accomplished using a carefully specified optical assembly housed inside an epi-fluorescence inverted microscope (Nikon Ti-U). The key components for LIF microscopy are excitation, dichroic, and emission filters which are usually combined into a single block or cube. Referring to the schematic shown in Figure 38, the 50nm narrow band pass excitation filter transmits only absorption wavelengths between 450 – 490 nm from the white light source. This ensures that only wavelengths in the non-overlapping absorption band are transmitted. The dichroic mirror reflects all incoming light up to 495nm. The excitation light fills the back aperture of the microscope objective and illuminates the sample. The fluorescent emission, reflected excitation, and background light are subsequently routed back through the objective. The dichroic mirror transmits all light greater than 495nm and the emission filter transmits light between 525 – 575nm. The filtered signals are captured and recorded on a high speed complementary metal-oxide-semiconductor (CMOS) camera (Photron SA5, 1024x1024 pixel array, 20μm/pixel) that is coupled directly to a microscope optical port. Fluorescence excitation is provided a 200W metal-halide light (Prior Scientific Lumen 200), when using Pyrromethene, or a 120W dual-cavity 532nm laser, when using Rhodamine. An extra-long working distance Plan Fluor objective with a 0.40 numerical aperture and 20x magnification was used for optical magnification.

The images captured with this experimental setup represent a two dimensional slice of the droplet volume with a thickness equal to the 3.4μm out-of-plane resolution. Fluorescent emission originating outside of the focus depth is essentially averaged by each pixel and information about out-of-plane intensity gradients is consequently lost.

Since the focusing depth is related to the square of the numerical aperture, decreasing the numerical aperture from 0.4 to 0.2 would increase the focusing depth to 13.6μm. If a highly three dimensional flow field is expected, additional steps must be taken to either increase the depth of focus or repeat the imaging process at different channel depths.

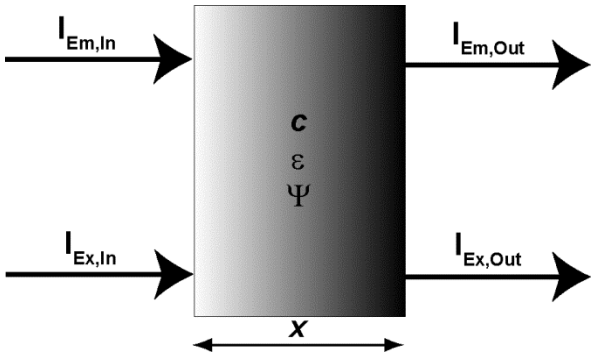

Figure 35. Control volume used to relate changes in excitation and fluorescent intensity to the participating medium absorption properties.

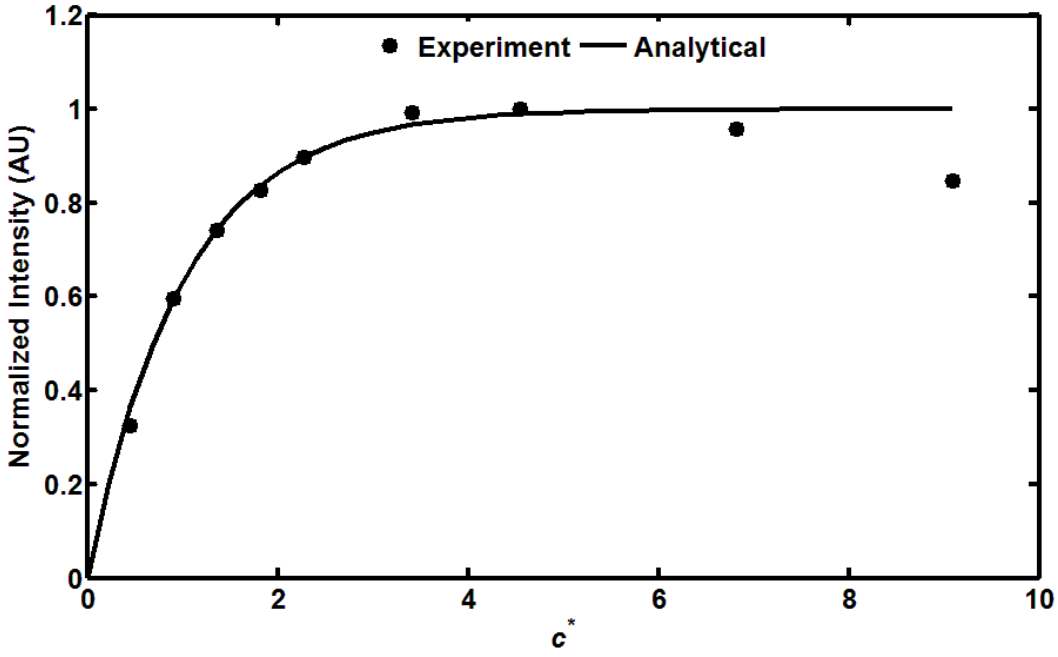

Figure 36. A comparison of experimental data (points) and analytical prediction (line) of Pyrromethene 556 fluorescent emission. Experimental data agrees well up to $c^* \sim 2$, after which higher order effects not included in the simple analytical model begin to take effect.

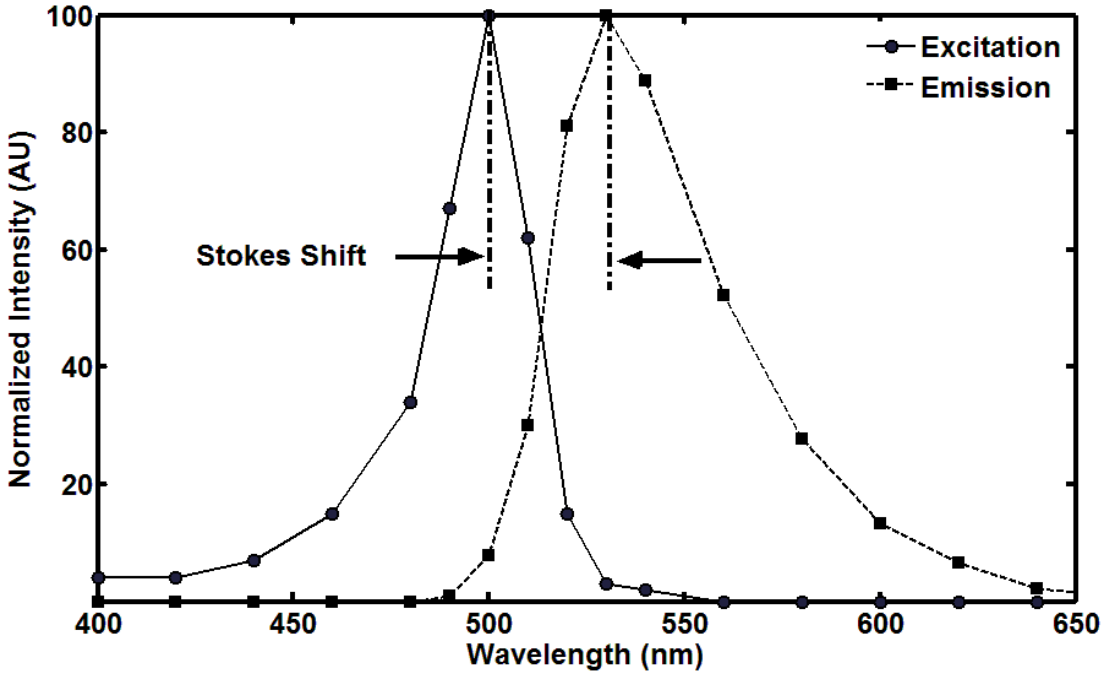

Figure 37. Excitation and emission spectrum for Pyrromethene 556 (Exciton 2011). The Stokes shift is the difference between maximum emission (540nm) and maximum absorption (495nm) wavelengths and is responsible for the visually-discernible blue to green color change characteristic.

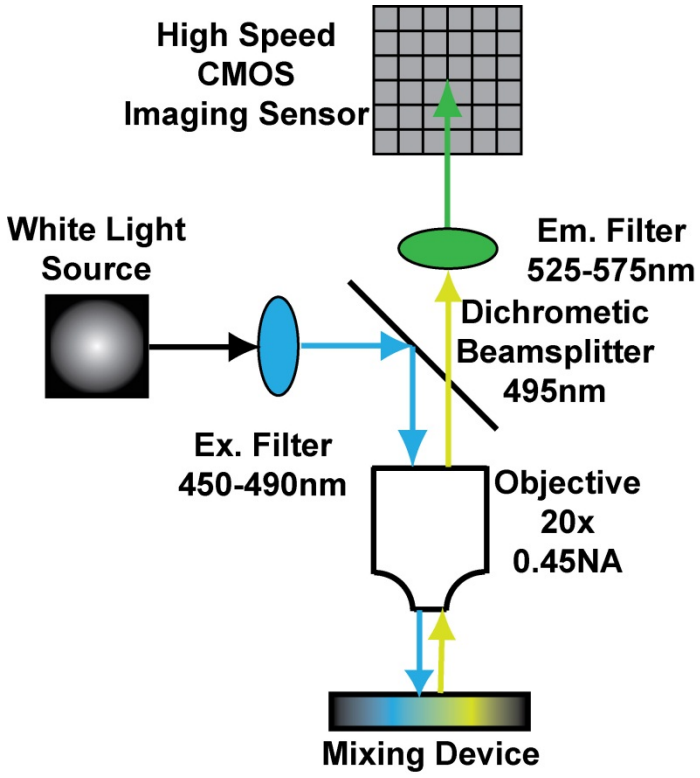

Figure 38. Epi-fluorescent filter setup configuration for the Pyrromethene 556 LIF mixing measurements. A 200W white light source is attenuated using a 470/20nm band pass filter. The light is reflected by a 495nm dichroic mirror, fills the back aperture of a 20x objective, and illuminates the sample. Fluorescent emission passes back through the objective, the dichroic mirror, and a 550/25nm band pass filter before being recorded on a high speed CMOS array.

4.3 Spatial Intensity Statistics

Using intensity statistics to assess the homogenization of a scalar field requires an acute understanding of what the calculated statistics represent in terms of the convective-diffusive dynamics that result following droplet collisions. This understanding is facilitated by considering the simple set of images in Figure 39, each a square array of unit length. The pixel intensity values range from 1 (white) to 0 (black) with a 256 discrete intensity values (8 bit images). Using the first image in the upper left corner as the initial state of a captured intensity field, two distinct processes can occur: pure convective rearrangement (top row, left to right) or pure diffusion (top row, top to

bottom). Convective motion rearranges the contents while maintaining the same discrete intensity values, much like shaking black and white marbles in a can. The images along the top row represent 2, 4, 16, and 64 spatial divisions, respectively. Pure diffusion maintains the same arrangement but smears the intensity values at the interfaces. Starting from the top row of images, each lower image has been spatially averaged 10^1, 10^3, and 10^4 times, respectively. Actual mixing is a combination of convective and diffusive motion acting in parallel. As shown in the Theoretical Modeling section, fluid properties (*Schmidt* number) and flow regime (*Reynolds* and *Peclet* number) determine the dominance of one path over the other. Visual observation reveals a "more mixed" field as compared to the initial state regardless of the path taken. It is the objective of the selected statistics to quantify this visual change in the intensity of segregation (diffusion) and length scale of segregation (convection).

The intensity of segregation is captured by comparing the mean intensity to each point in the mixing domain, where small differences imply less intense segregation. The expected value μ of a continuous planar intensity distribution I is:

$$\mu = \frac{\int_A I dA}{A} \qquad \textbf{18}$$

For the images in Figure 39, the expected value is 0.5 for each image regardless of the mixing path taken (convective or diffusive). The average intensity for a closed, linear system, much like the average concentration, is a conserved quantity.

The intensity of segregation provides a measure of how the spatial intensity values deviate from the expected value. For miscible mixing, it is a valuable metric for determining the dispersion of the intensity field. The intensity of segregation is found through the standard deviation of the intensity field I:

$$\sigma = \left[\frac{\int_A (I-\mu)^2 \, dA}{A} \right]^{\frac{1}{2}} \qquad \textbf{19}$$

Since the intensity of segregation is essentially a measuring stick for variability, it is important to place this measurement in context with the system being investigated. The standard deviation alone is meaningless without knowledge of the expected value. For instance, a standard deviation of 0.5 for a sample mean of 50 indicates little variability compared to a system with a sample mean of 1. Another complication in using Equation 49 directly is the dependence of the standard deviation to the magnitude of the intensity values. If results are obtained using an exposure of 10μs and compared to results using an exposure of 1μs, the standard deviation would differ even though the actual mixing may be unchanged. This is due to the larger intensity values obtained for slower exposures. Normalizing the intensity of segregation by the mean value remedies both these issues.

The normalized intensity of segregation is an excellent metric for purely diffusive processes, such as that shown in the column of images where the initially black and white distribution is smeared to a greater degree of gray at the interfaces. The plot in Figure 40 shows how the normalized standard deviation, σ/μ, decreases as the extent of diffusion is increased from an initial convective distribution along to the top row. Two important points are learned from this simple exercise. First, the intensity of segregation is not affected by how the contents of the mixing domain are arranged. Once the number of black and white marbles in a can is fixed, the intensity of segregation remains constant regardless of how vigorously the can is shaken. This means this statistic is insensitive to highly inertial mixing and irrelevant for immiscible mixing. The caveat here is that once the spatial resolution of the measurement system is exceeded, the intensity of segregation will behave as though diffusion is present. For instance, if the spatial resolution is the size of two marbles, the captured pixel intensity would be the average of the two marble intensities. Second, starting a diffusion process from a much more rearranged state significantly reduces the intensity of segregation for the same number of diffusive

averages. This is due to the number of interfaces available for diffusion. The intensity of segregation decreases by nearly two decades for the image with 64 divisions while changes are negligible for the image with only 2 divisions for the same number of diffusive averages. This highlights the role of convective transport in droplet mixing where small convective timescales yield reduced mixing times.

In order to capture the convective rearrangement process, a statistic is needed that concerns the local intensity distribution. This is visually conveyed by the average number of identifiable interfaces, with more interfaces being indicative of a greater potential for mixing. These interfaces can be expressed mathematically by the magnitude of the local intensity field divergence and averaged over the entire field:

$$\Phi = \frac{\int_A |\nabla I| dA}{A} \qquad \textbf{20}$$

For 2D digitized images, the quantity of interest is the magnitude of the gradient in the x and y direction at each pixel location. The partial differential equations are readily computed using a second order accurate, finite differencing scheme with appropriate padding at the image boundaries. Note that this statistic is keenly similar to a localized standard deviation where the expected value is computed based on a localized pixel subdomain, as opposed to the entire mixing domain.

The lower plot in Figure 40 shows how the average intensity gradient changes with increasing convective rearrangement. For a purely convective mixing path (top row, left to right), the average gradient increases with increasing number of divisions. The change is negligible, however, for a purely diffusive process that begins highly segregated, such as that given by the first two columns of images (2 and 4 divisions). If diffusion begins from a more rearranged state, the average gradient decreases by 2-3 decades (16 and 64 divisions). These results show that convective and diffusive action has opposite effects on the average intensity gradient. Indeed, it is the role of convection and diffusion to create and smear gradients, respectively. A potentially hazardous interpretation of the average

gradient is that a decreasing trend must signify diffusive action. Indeed, the average gradient continues to grow with increasing convective rearrangement but only until the length scale of each pixel is larger than the actual distance over which the gradient occurs. Even in the absence of diffusion, the average gradient will decrease once the spatial resolution of the measurement system is exceeded.

In order to examine convective mixing processes in greater detail, a statistic is needed that is sensitive to the reduction in mixing length scales. For the simple checkerboard images, the effective length scale is obvious but there is no accepted statistic that succinctly provides what our eyes easily distinguish. Given a fixed imaging area, the effective mixing length decreases from increases from the largest resolvable length scale (image size) to the smallest resolvable length scale (one pixel in this case). By computing the intensity of segregation on an image sub-domain and integrating throughout the mixing domain, an effective length scale is identified.

Consider again a planar intensity field *I=I(x,y)*, where $x \in [0, X]$ and $y \in [0, Y]$. The average intensity of a subdomain of size S^2 is:

$$\mu_S(S, x, y) = \frac{\int_y^{y+S} \int_x^{x+S} I(x, y)\,dx\,dy}{S^2} \qquad \textbf{21}$$

The intensity of segregation between all subdomains of size S^2 and the expected value of the field is:

$$\sigma_S(S) = \left[\frac{\int_0^{Y-S} \int_0^{X-S} \left(\mu_S(S,x,y) - \mu\right)^2 dx\,dy}{(X-S)(Y-S)} \right]^{\frac{1}{2}} \qquad \textbf{22}$$

As the size *S* of each subdomain is increased, the intensity of segregation σ_S becomes insensitive to further changes once the length scale of the intensity distribution is reached.

This process is easily extended to a 2D intensity field by including the additional spatial integral and readily discretized for digital images.

For the checkerboard images shown in Figure 39, the mixing length scale is given by the black and white checkerboards. It is expected, therefore, the σ_S becomes invariant to further increases in S once this length scale is reached. The plot in Figure 41 illustrates these trends, where this process is performed for the top row of images (no diffusion) in Figure 39. For consistency, σ_S is normalization with the expected value μ. Inspection of σ_S for the four images reveals three important trends. First, σ_S is equal to the intensity of segregation at $S = 0$. Second, once S exceeds scale of intensity differences, there is no appreciable change σ_S. This identifies the effective mixing length of the system and, unlike the intensity of segregation and average intensity gradient, provides a measure of the length scale of mixing. Finally, the asymptotic value of σ_S as S approaches the size of the mixing domain provides a measure of the true intensity of segregation for highly convective processes. Recall that the intensity of segregation σ is only sensitive to diffusive processes. Conversely, σ_S is largely insensitive to diffusive mixing. The plot in Figure 43 computes σ_S for the 4x4 checkerboard pattern for 0, 10, 100, and 1000 diffusive averages. It is only when the interfaces are substantially smeared that σ_S shows appreciable changes.

It is evident based on these simple cases that the standard deviation captures diffusive mixing well but does not recognize spatial rearrangement. This missing metric is provided by the average local gradient which recognizes stirring contributions. Because mixing in most processes of interest are a combination of convective and diffusive paths, using only a single statistic does not provide a complete picture of the mixing event. These two statistics together provide a window into the simultaneous process of convective-diffusive mixing.

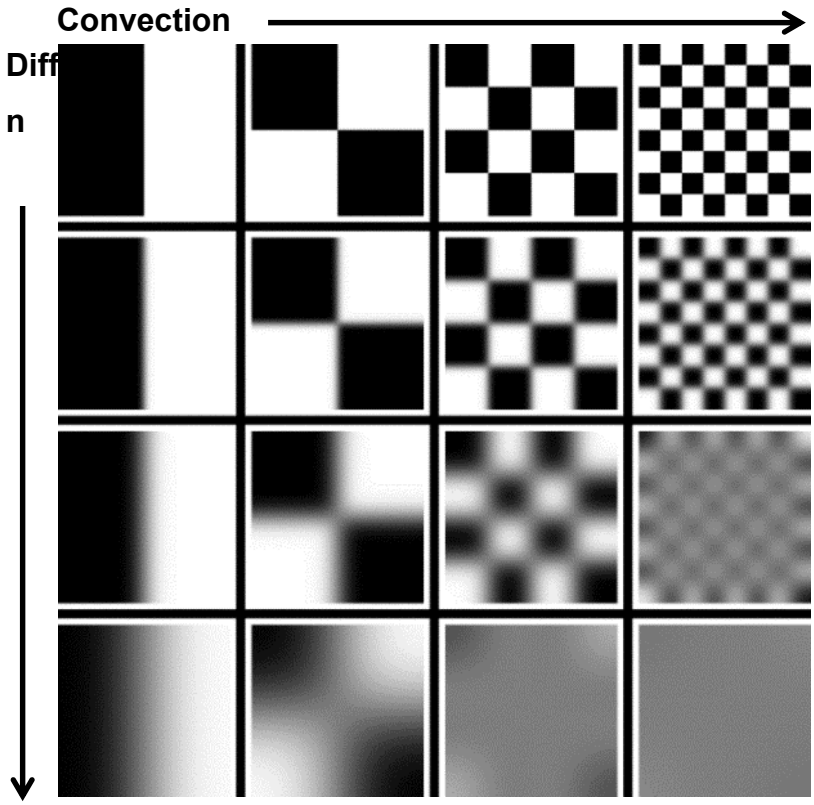

Figure 39. A series of simple gray-scale images that illustrate the role of convection and diffusion in mixing. Each of the 16 images is a 400x400 pixel array. Starting from the initial distribution in the upper left corner, the pixels can be convectively rearranged by 2^2, 2^4, and 2^6 times (upper row) or diffusively averaged 10^1, 10^3, and 10^4 times (left column). The remaining three columns represent the same diffusive mixing but starting from a more convectively rearranged state.

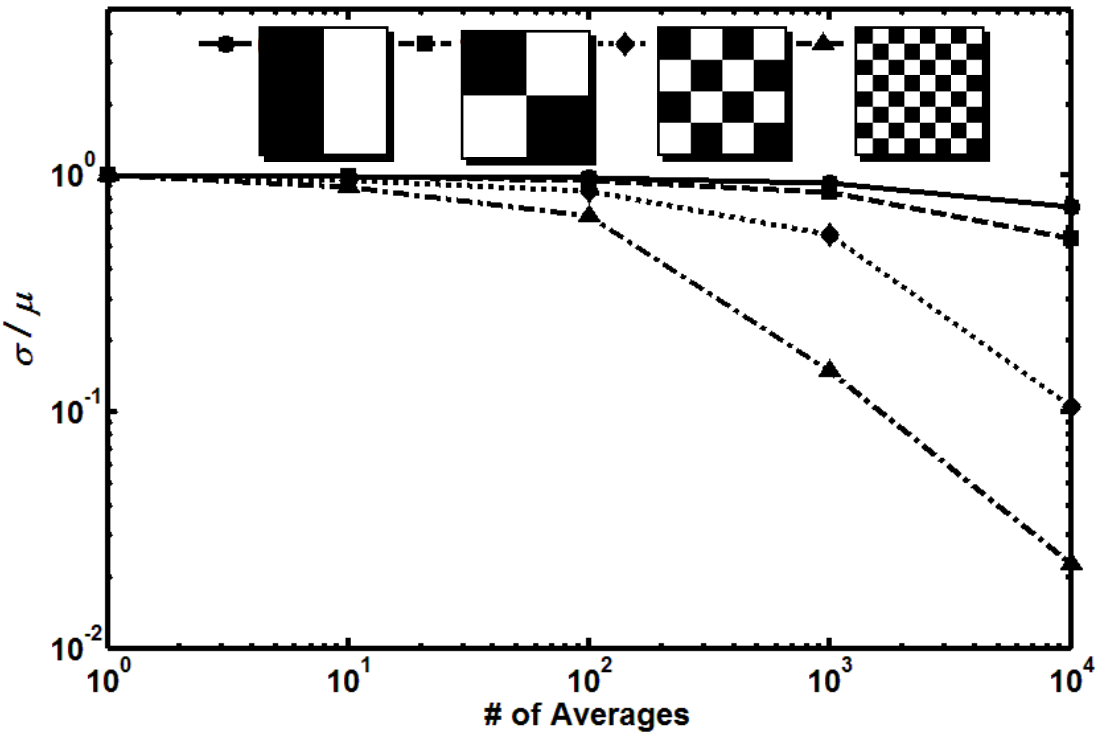

Figure 40. This plot shows how the normalized intensity of segregation is affected by the degree of diffusive averages for the top row of images shown in Figure 39. Note that the intensity of segregation begins at the same value regardless of the amount of convective rearrangement.

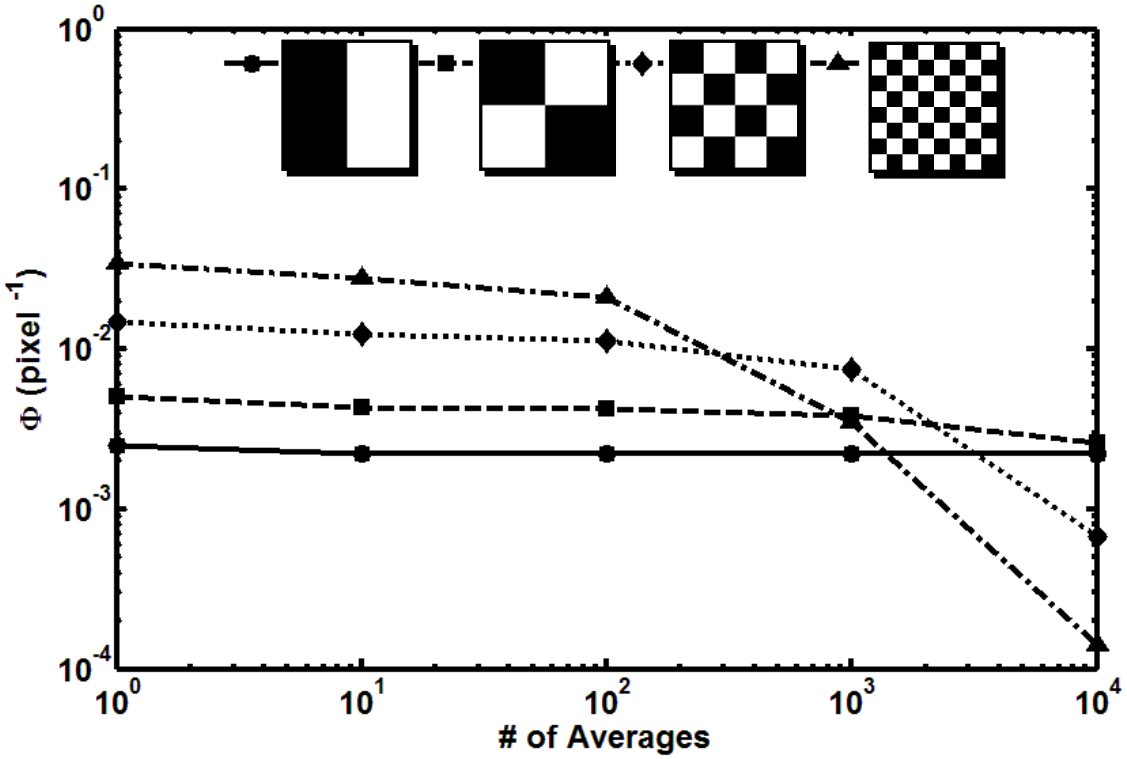

Figure 41. This plot shows how the average intensity gradient is affected by the degree of diffusive averages for the images shown in Figure 39. Unlike the intensity of segregation, the average intensity gradient is very sensitive to convective rearrangement but remains relatively unchanged for diffusive mixing until a high degree of homogenization is reached.

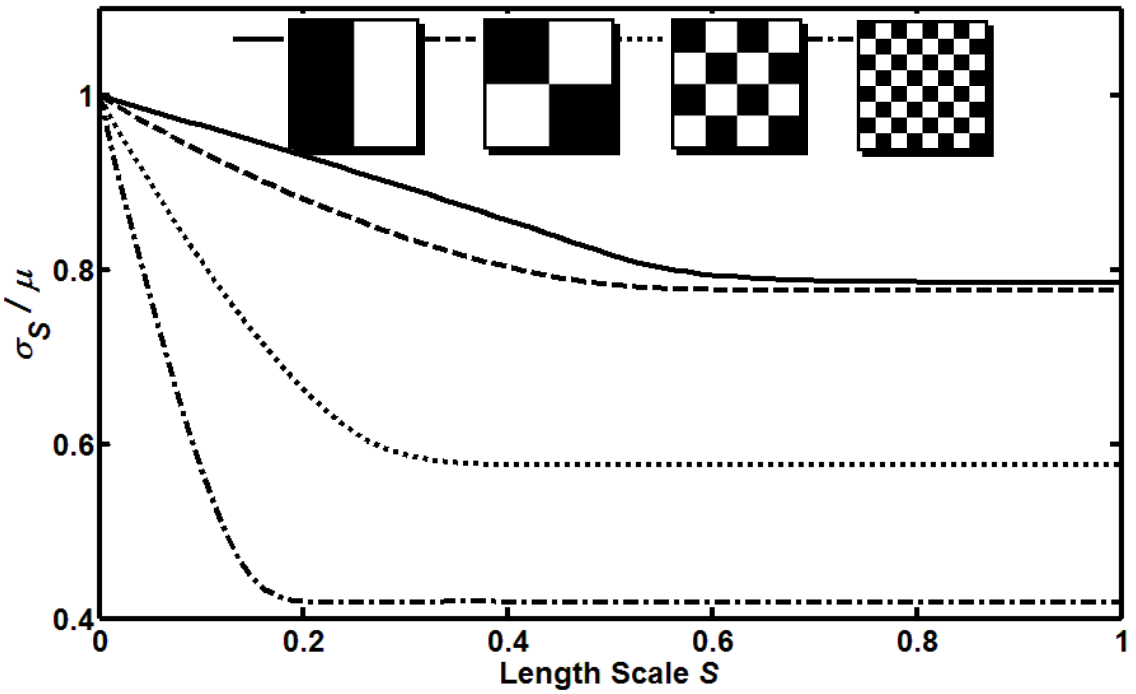

Figure 42. This plot shows how the normalized scale of segregation changes with increasing convective rearrangement, corresponding to the top row of images in Figure 39. As the length scale *S* reaches the size of the black and white squares, the scale of segregation becomes invariant in further changes in *S* and captures the effective length scale for mixing.

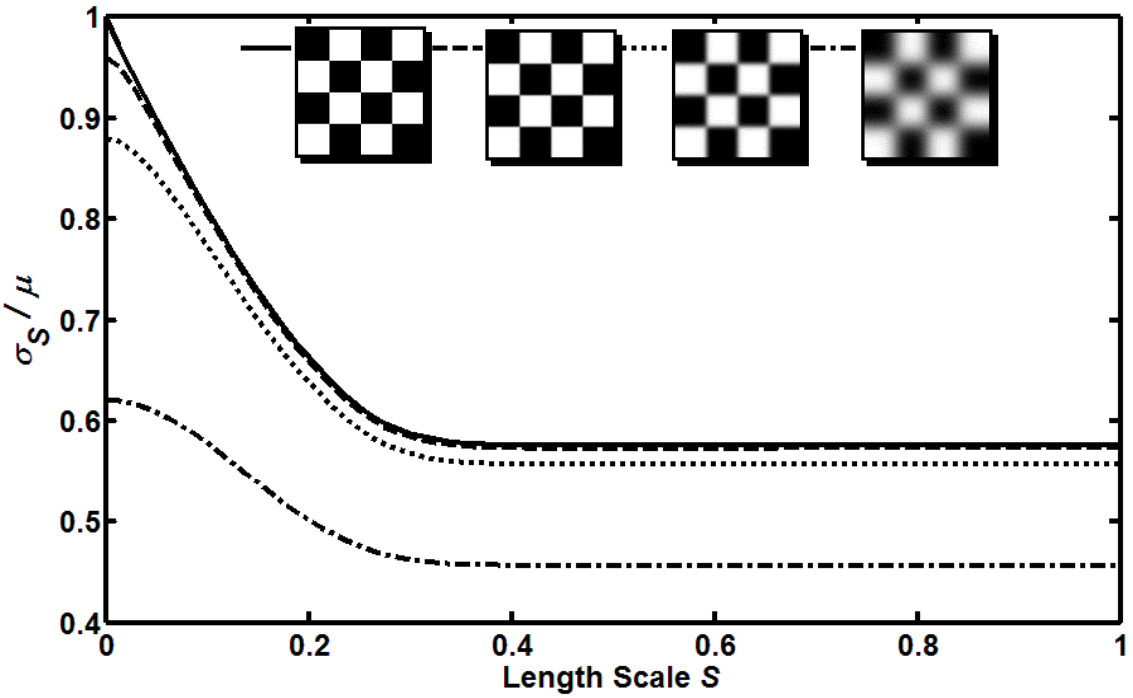

Figure 43. This plot shows how the scale of segregation is affected by diffusive processes as the length scale S is changed. Diffusion influences the starting value but the resulting mixing length remains largely unaffected.

4.4 Image Processing

Another challenge in using intensity field statistics to quantify mixing is intensity attenuation due to non-uniform spatial illumination and intensity bias due to background noise. The laser used for excitation follows a Gaussian intensity distribution that peaks in the center and exponentially decreases in the radial direction. This means that if a solution of uniform fluorophore concentration is imaged, the intensity field shares the same Gaussian distribution. This yields a finite intensity of segregation that is not indicative of the completely mixed condition. This is remedied by taking images of uniform concentration fields during each experiment and using this profile images to flatten the mixing images. The intensity bias is estimated by taking a number of images without the excitation source. The images are averaged for each pixel and subtracted from each mixing image. This is an important step when CMOS sensors are used since

each pixel has a unique noise signature. Unlike a CCD camera which routes all pixel information through the same analog-to-digital converter, each pixel on a CMOS sensor has an analog-to-digital converter.

4.5 Volume Tracking

One of the challenges in applying these statistics to droplet mixing is identification of the droplet volumes, which do not fill the entire image frame and translate across the frame throughout the mixing event. Locating each droplet prior to collision requires that both droplets emit a detectable signal while maintaining sufficient intensity difference to make the statistics meaningful. This is overcome by using fluorophore concentrations (optical thicknesses) that are an order of magnitude different between the two droplets prior to collision. The captured frames are exported in tagged image format (TIFF) at 12bit resolution (4,096 intensity levels) and converted to double precision values between 0 and 1. A custom image processing code is executed in MATLAB™ to spatially identify the droplet volumes for each frame. The locating algorithm is based on thresholding of the local intensity spatial gradient to identify droplet boundaries. Once identified, shape filling numerical technique is used to fill in droplet volumes. This process produces a binary region of interest (ROI) mask that is used for confining the mixing statistics to the liquid droplet volumes only. The pairs of images in Figure 44 illustrate the binary ROI process for an actual mixing event and highlight the volume tracking process. A single droplet of high fluorophore concentration (high intensity) is perched at the apex of a Y-junction (image pair 1). A second droplet of lower fluorophore concentration (low intensity) approaches from the lower right (image pair 2) and collides with the first droplet (image pair 3). Mixing takes place within the coalescing droplet (image pair 4). Note the presence of a counter-rotating vortex that is generated as a result of the collision.

4.6 Summary of Research Accomplishments

- Used wide-field microscopy, pulsed laser illumination, differential fluorescence, and high speed imagery to capture instantaneous droplet concentration fields before, during, and following confined collisions.
- This optical diagnostic system capable of 1μm and 20μs spatial and temporal resolution, respectively
- Unlike point-wise or time averaged mixing measurements, this technique provides a 2D snapshot of mixing and captures dynamics previously unavailable.
- Developed statistical metrics that separate the roles of convection and diffusion in confined droplet collision mixing.
- Developed image processing algorithms that accurately identify and track droplet volumes throughout the mixing event. This is critical for producing the governing mixing statistics.
- A paper outlining this work is schedule for publication in *Experiments in Fluids*, paper #136

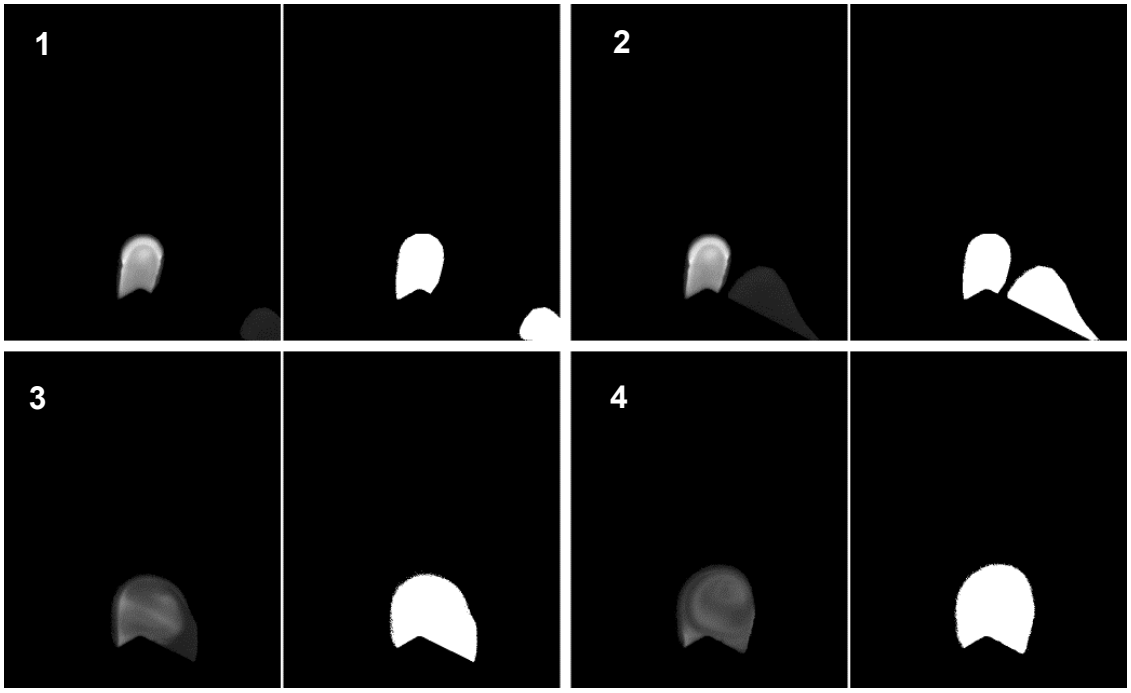

Figure 44. A series of images of an actual mixing event that illustrates the image processing technique used to identify each droplet volume. Each raw image (left) is accompanied by the corresponding binary image (right) that shows the droplets in white and clearly identifies the droplet volumes throughout the mixing event. The image sequence shows a droplet perched at the Y-junction apex while second droplet is approaching from lower right (1), the moment just prior to collision (2), the moment just after collision indicating intensity gradient development (3), and the mixing dynamics 1ms after collision showing the formation of a single vortex with counter-clockwise rotation (4).

CHAPTER 5

DROPLET MIXING

This chapter covers the droplet mixing results obtained using the experimental setup and optical diagnostic procedure previously described. A theoretical model is first described that predicts droplet mixing time based on relevant geometrical and hydrodynamic conditions. Mixing results obtained across a decade of *Reynolds* and *Peclet* numbers are then presented and comparisons are made with the theoretical model. Finally, attempts are made to bridge the differences between model and experiment.

5.1 Theoretical Modeling

In order to predict the potential benefit of convective transport in droplet mixing, a simple theoretical model is proposed that captures the relevant geometric aspects, such as droplet aspect ratio, fluid properties, such as mass diffusivity, and flow hydrodynamics, such as average droplet speed. Consider a rectangular microchannel of height H and depth W, as shown Figure 45, containing an ideal plug of two, immiscible fluids with mass diffusivity D. The physical length of the plugs is L and each is oriented such that the concentration interface is located normal or parallel to the channel axis (axial or radial). Initially, both species are equally distributed in the channel and a steady average droplet velocity U is imposed in the positive z-direction.

Assuming there are no concentration gradients in the y direction for either the axial or radial orientation, the convective-diffusive equation governing the time dependent scalar concentration field for this non-reacting system is:

$$\frac{\partial c}{\partial t} + v_z \frac{\partial c}{\partial z} = D\left(\frac{\partial^2 c}{\partial x^2} + \frac{\partial^2 c}{\partial z^2} \right) \qquad \textbf{23}$$

This equation is non-dimensionalized as follows:

$$c^* = \frac{c}{c_{Max}}, v^* = \frac{v_z}{U}, x^* = \frac{x}{H}, z^* = \frac{z}{L} \qquad \textbf{24}$$

Substituting values gives:

$$\frac{\partial c^*}{t} + \frac{U}{L}\left(v^* \frac{\partial c^*}{\partial z^*}\right) = D\left(\frac{1}{H^2}\frac{\partial^2 c^*}{\partial x^{*2}} + \frac{1}{L^2}\frac{\partial^2 c^*}{\partial z^{*2}}\right) \qquad \textbf{25}$$

Since each spatial derivative is of order unity, the coefficients appearing in front of each term provide the representative timescale for each process. Three regimes are readily identifiable: diffusion dominated mixing where the timescale for mass diffusion is much greater than the timescale for bulk convection; dispersive mixing where the timescale for mass diffusion is comparable to the timescale for bulk convection; and convection dominated mixing where the timescale for mass diffusion is negligible compared to the timescale for bulk convection. Under diffusion dominated mixing, the governing differential equation for the axial and radial arrangement shown in Figure 45 reduces to:

$$\frac{\partial c^*}{t} = \frac{D}{L^2}\frac{\partial^2 c^*}{\partial z^{*2}} \qquad \textbf{26}$$

$$\frac{\partial c^*}{t} = \frac{D}{H^2}\frac{\partial^2 c^*}{\partial z^{*2}} \qquad \textbf{27}$$

By imposing no mass transfer at the liquid/channel boundary and a completely segregated initial concentration distribution, solution to the equations above give a cosine series solution:

$$c^* = 0.5 + \sum_{n=1,Odd}^{\infty} (-1)^{\frac{n-1}{2}} \frac{2}{n\pi} \exp\left(-\frac{t}{L^2/D} n^2 \pi^2\right) \cos\left(n\pi z^*\right) \qquad \textbf{28}$$

$$c^* = 0.5 + \sum_{n=1,Odd}^{\infty} (-1)^{\frac{n-1}{2}} \frac{2}{n\pi} \exp\left(-\frac{t}{H^2/D} n^2 \pi^2 \right) \cos(n\pi x^*) \quad \textbf{29}$$

The time required for complete homogenization where every spatial location displays the same concentration is infinite. In order to arrive at a finite timescale, a condition is imposed that mixing is complete when the spatial concentration variance decays to some reasonable value. This condition can be expressed as follows:

$$\sigma(t) = \left[\frac{\int_0^S (c^* - 0.5)^2 \, ds}{S} \right]^{\frac{1}{2}} < 0.1 \quad \textbf{30}$$

Where the spatial direction s and length scale S correspond to z and L for axially arranged and x and H for radially arranged mixture. The listed value of 0.1 corresponds to the 90% mixed condition that is typically used in mixing analyses (Paul et al. 2004). Applying the variance condition in Equation 8 yields the following mixing times for axially and radially oriented mixtures, respectively:

$$t_{Mix} = 0.21 \frac{L^2}{D} \quad \textbf{31}$$

$$t_{Mix} = 0.21 \frac{H^2}{D} \quad \textbf{32}$$

As expected, the time required to mix is on the order of the diffusion time. Using a diffusivity of 10^{-10} m^2/s and a length scale of 100μm, the time required to achieve 90% mixture quality would be about 21 seconds. Such a long mixing time is impractical for microfluidic applications and exemplifies the need for improved mixing strategies.

By decreasing the convective timescale, the mixing time can be substantially reduced. Consider the conditions where the convective timescale is on the order of the diffusion timescale and the fluids are arranged axially. Sir Geoffrey Taylor showed that under these

conditions the effective diffusion coefficient for miscible liquids flowing slowly inside a circular tube of diameter *2R* is proportional to the Peclet (*Pe*) number (Taylor 1953):

$$D_{Eff} = D\left(1+\frac{1}{48}\left(\frac{UR}{D}\right)^2\right) = D\left(1+\frac{1}{48}Pe^2\right) \qquad \textbf{33}$$

These dispersion results are applicable for $4\frac{L}{R} > UR/D > 6.9$. Shortly after Taylor's seminal paper, Rutherford "Gus" Aris extended his analysis and applied it to a larger range of *Pe* numbers and for a general cross-section to yield (Aris 1956):

$$D_{Eff} = D\left(1+\kappa\left(\frac{U\frac{d}{2}}{D}\right)^2\right) \qquad \textbf{34}$$

Where κ is a constant dependent on the geometry of the channel and *e* is the channel eccentricity:

$$\kappa = \frac{1}{48}\frac{24-24e^2+5e^4}{24-12e^2} \qquad \textbf{35}$$

$$e = \left(1-\frac{b^2}{a^2}\right)^{\frac{1}{2}} \qquad \textbf{36}$$

For a circular tube, $e = 0$ and $\kappa = 1/48$, thereby giving Taylor's initial result. For high aspect ratio channels, $e \sim 1$ and κ is 5/12 times smaller as compared to a round cross-section. The diffusivity appearing in Equation 9 above is now replaced with the effective Taylor dispersion coefficient to yield the required mixing time:

$$t_{Mix} = 0.21\frac{L^2}{D_{Eff}} = 0.21\frac{L^2}{D\left[1+\frac{\kappa}{4}\left(\frac{UH}{D}\right)^2\right]} \sim \frac{L^2}{D}\frac{1}{Pe^2} \qquad \textbf{37}$$

This result shows that the mixing time is reduced as *Pe* increases and becomes proportional to Pe^{-2} for $Pe >> 1$. For a 100μm droplet of uniform aspect ratio droplet and a *Pe* number of 10, the time required to achieve 90% mixedness is about 11s.

Conversely, if the two fluids are radially orientation, diffusion and mass advection occur in orthogonal directions: diffusion in the transverse direction and bulk flow in the axial direction. Under such conditions, the Taylor diffusion coefficient derived above is no longer applicable and the time required to mix two fluids in this orientation is given by:

$$t_{Mix} = 0.21\frac{H^2}{D} \qquad \textbf{38}$$

A radially arranged droplet requires over 50% more time to achieve 90% mixedness as compared to an axially arranged droplet with a *Pe* of 10. The significance of this result is the amount of channel length required to meet this level of mixedness. For an average droplet velocity *U,* the channel length necessary is:

$$l_{Mix} = Ut_{Mix} = 0.21U\frac{H^2}{D} = 0.21H\ Pe \qquad \textbf{39}$$

Note that in this case the channel length increases with *Pe* number as opposed to an inverse relationship as provided by Taylor diffusion.

For flow conditions where the timescale for convective transport is much less than that for molecular diffusion, no direct solution to Equation 3 exists. An estimate of mixing time can be facilitated, however, through some simple scaling laws. When two immiscible fluids interact under highly inertial conditions, particle trajectories become chaotic and a non-reacting the concentration field undergoes continual stretching and folding operations that exponentially reduce the effective length for diffusion and consequently reduce the mixing time. As described by Aref, chaotic advection is the condition where any two particles released at some instance of time loses track of each other while sampling the entire fluid domain (Aref 1984). The result is a concentration

field that is continually stretched and folded such that the effective length for diffusion is exponentially reduced. Stroock et al. (Stroock, et al. 2002) investigated inertial mixing in a continuous flow mixing device and observed and this same behavior by generating flow in the transverse direction using raised geometric structures in microchannels. Using a fluorescent tracer and confocal microscope images, Stroock et al. experimentally confirmed what Ottino showed analytically (Ottino 1990) and what Jones produced numerically (Jones et al. 1989) as an exponential decrease in the effective striation length:

$$s = d\exp\left(-\frac{z}{\lambda}\right) \qquad \textbf{40}$$

In this relation, s is the striation length, d is the system length scale, λ is a constant dependent on channel geometry, and z is the spatial distance in the direction of flow. Highly inertial conditions imply that diffusion is negligible compared to convective transport. Under such conditions, mass diffusion only becomes important when the time required to diffuse across a striation length is on the order of the convective timescale. Although not intuitively obvious, there is no restriction on the initial orientation of the mixing liquids since such information is quickly lost under chaotic conditions. Applying Equation 8 to the mixing system shown in Figure 2, the mixing time is predicted as:

$$t_{Mix} \sim l_{Mix} U \qquad \textbf{41}$$

$$\frac{s^2}{D} \sim \frac{L}{U} \qquad \textbf{42}$$

$$\left(\frac{s}{H}\right)^2 \sim \frac{LD}{UH^2} \sim \frac{L}{H}\frac{1}{Pe} = \exp\left(-2\frac{l_{Mix}}{\lambda}\right) = \exp\left(-2\frac{Ut_{Mix}}{\lambda}\right) \qquad \textbf{43}$$

$$t_{Mix} = -2\frac{\lambda}{U}\ln\left(\frac{L}{H}\frac{1}{Pe}\right) = 2\left(\frac{\lambda}{L}\right)\left(\frac{L}{U}\right)\ln\left(\frac{H}{L}Pe\right) \qquad \textbf{44}$$

This important result shows that mixing time is proportional to the convective timescale, L/U, and channel geometric features, λ/L, while only mildly affected by the inverse of the droplet aspect ratio, H/L, and Pe. Thus, under inertial dominated mixing, the driving and limiting parameter for mixing is the convective timescale. This result foreshadows the experimental work to follow, where mixing is accelerated by droplet collisions occurring at sub-millisecond convective timescales.

Non-dimensionalizing the three preceding results by the mass diffusion timescale enables direct comparison of the effects of Pe number:

$$Diffusion: \tau = 0.21\left(\frac{L}{H}\right)^2 \quad \textbf{45}$$

$$Dispersion: \ \tau = 0.21\left(\frac{L}{H}\right)^2\left(1+\frac{\kappa}{4}Pe^2\right)^{-1} \quad \textbf{46}$$

$$Convection: \ \tau = 2\left(\frac{\lambda}{L}\right)Pe^{-1}\ln\left(\frac{H}{L}Pe\right) \quad \textbf{47}$$

These results are shown graphically in Figure 46 for a droplet aspect ratio and λ/L of 1. The important implications of modeling results are that dispersion is confined to a narrow Pe number region. The effects droplet aspect ratio is the same for diffusion dominated and dispersion dominated mixing. Convection dominated mixing is largely unaffected by droplet aspect ratio but the transition from dispersion to convection is delayed as the aspect ratio is increased.

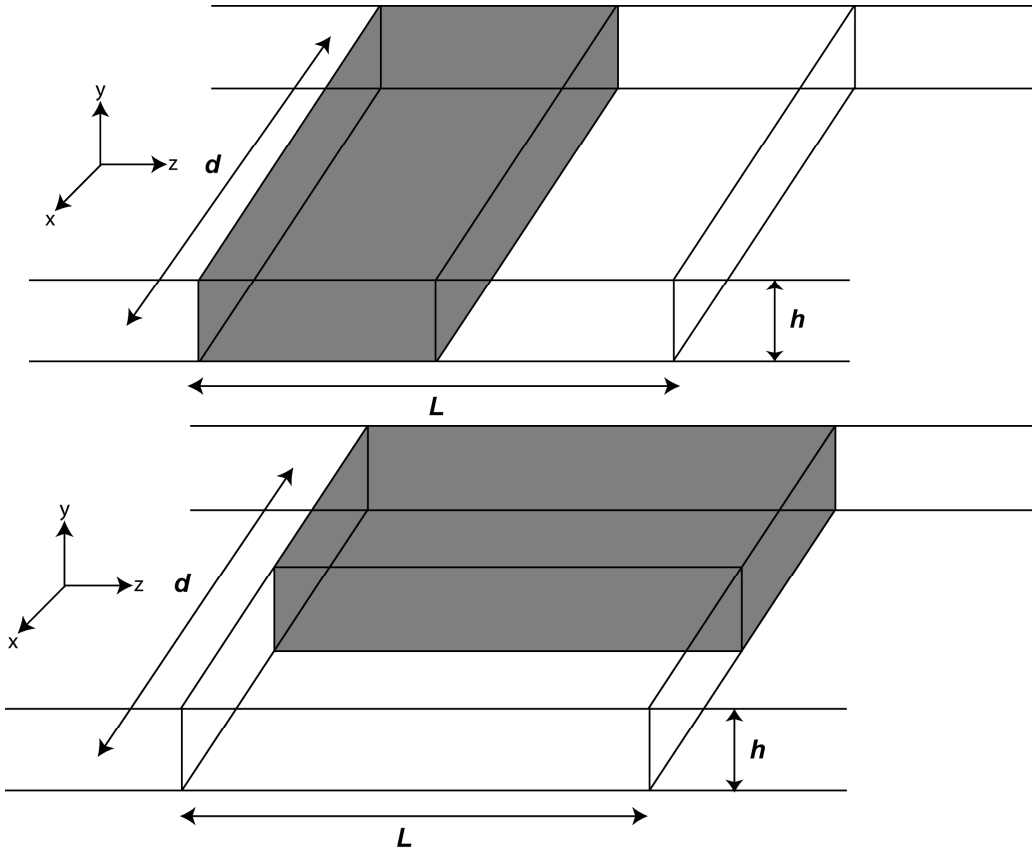

Figure 45. Control volume and fluid orientations (top: axial, bottom: radial) considered for the theoretical droplet mixing time predictions for miscible liquids of equal volume.

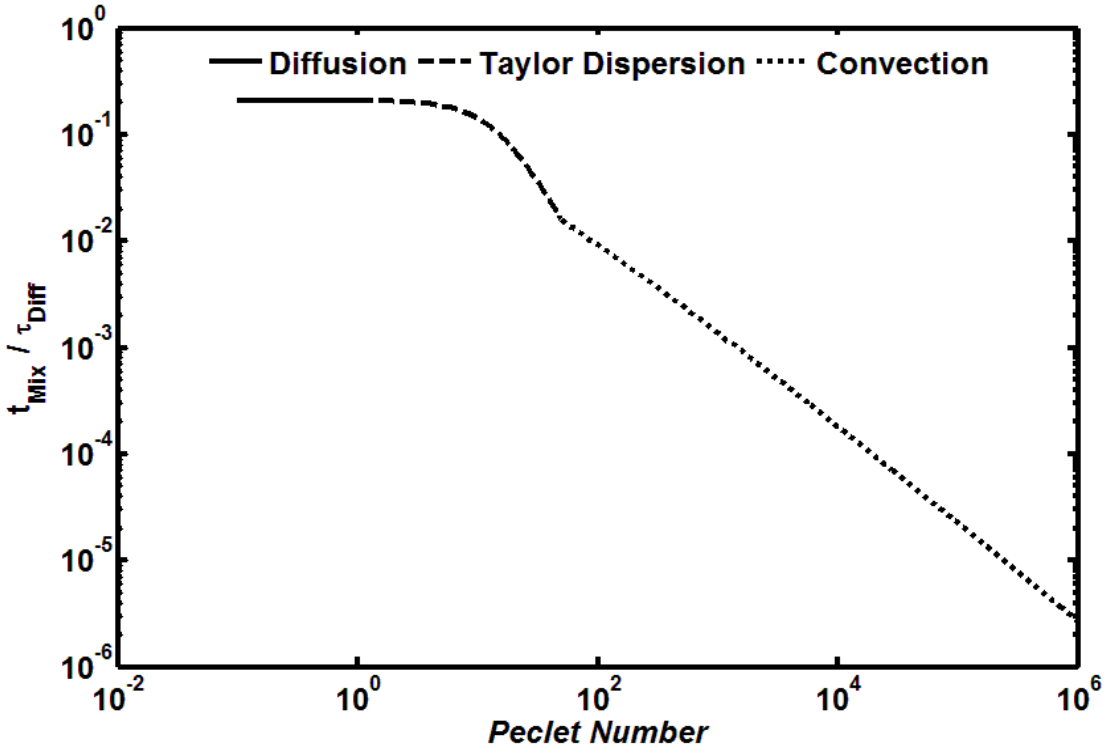

Figure 46. This plot shows modeling results of mixing time across six decades of *Pe* number for a droplet aspect ratio and λ/L of 1 and a radially arranged plug configuration. The mixing time has been non-dimensionalized by the mass diffusion timescale. Note that the region where dispersion is active covers a narrow *Pe* number range before succumbing to convective mixing.

5.2 Mixing Results

Mixing dynamics in colliding droplets are examined using the previously described optical diagnostic technique. Two droplets of high (0.8mg/mL, $c^* \sim 1.5$) and low (0.08mg/mL, $c^* \sim 0.15$) Pyrromethene 556 concentration are collided at a Y-junction. The two liquid streams from where the droplets originate are prepared using 0.2μm filtered, steam distilled water. Litmus measurements of each mixture prior to injection into the mixing device showed a common pH of 7. Uniform pH is important because fluorescent emission Pyrromethene dyes are sensitive to solution pH, particularly in acidic surroundings (Yariv and Reisfeld 1999). A common pH between the colliding

droplets ensures that changes in fluorescent emission are due only to changes in concentration. Channel geometry used for these experiments is captured by the CAD image in Figure 7. The 12bit (4,096 intensity levels) monochromatic images were captured using an exposure and frame rate of 25μs and 20,000fps, respectively, and converted to double precision intensity images for statistical analysis.

Of the many collisions cataloged, three representative cases are presented that highlight how mixing is influenced by droplet inertia. The *Re* numbers considered are 7, 31, and 74 with corresponding convective timescales of 2, 0.5, and 0.1ms. The viscous timescales remained relatively constant at 13, 17, and 8ms, respectively. These three cases are denoted as Collision 1 (low *Re* number, long convective timescale), Collision 2 (mid *Re* number, mid convective timescale), and Collision 3 (high *Re* number, short convective timescale). The length scales and velocity values used to formulate the collision *Re* number and convective and viscous timescales for each collision are established using the images just prior to droplet impact. The length scale for each droplet is determined based on the number of non-zero pixel values appearing in the binary ROI mask. A collision length scale is then calculated using the following expression:

$$L_{Collision} = 2\frac{L_{Droplet\ 1}L_{Droplet\ 2}}{L_{Droplet\ 1} + L_{Droplet\ 2}} \quad \textbf{48}$$

For two equally sized droplets, the collision length scale is equal to the individual droplet length scale. As any one of the length scales approaches infinity, the collision length scale approaches twice the value of the finite scale. Since the interest here is mixing due to droplet collisions, the collision length scale is the characteristic length of the mixing process. The length scales for these three cases varied by less than a factor of two. The collision velocity is determined by the relative velocity between the two droplets at the time of collision. Droplet velocity is determined by pixel displacement, pixel size, and image frame rate. The collision velocity ranged from 0.06 to 0.8m/s. Changes in the collision *Re* number and convective timescale are consequently due to changes in droplet

inertia as opposed to length scale differences. A summary of these collision parameters is provided in Table 1.

The mixing statistics given by Equation 19 and 20 are calculated for each image frame and are based only on the non-zero pixel locations appearing in the binary ROI mask. The mixing time listed in Table 1 is determined by the temporal trend of the normalized standard deviation of the droplet intensity field. In order to track the progress of mixing and clearly identify a mixing timescale, a mixing parameter η is derived that is based on the normalized standard deviation for each image frame and scaled by the initial and steady-state values:

$$\eta = \frac{\frac{\sigma}{\mu}_t - \frac{\sigma}{\mu}_\infty}{\frac{\sigma}{\mu}_0 - \frac{\sigma}{\mu}_\infty} \qquad \textbf{49}$$

The initial and steady-state values used to formulate η correspond to the last frame just prior to droplet impact and the last frame where σ/μ becomes invariant with time. Cast in these terms, this mixing parameter begins at unity and asymptotically approaches zero as mixing progresses. Dynamic mixing within the sub-second timescales considered is assumed complete when η reaches 0.1, or is within 90% of its steady-state value.

The time trace for σ/μ and η is shown in Figure 47 and Figure 48, respectively. Each case shows different mixing rates and steady state values. The intensity of segregation provides a measure of mixedness for each captured image frame. The statistic decreases from its maximum value just prior to collision and achieves a minimum value that remains relatively invariant under the timescales considered. The results show decreased intensity residuals for collisions occurring at higher relative velocities where increased rearrangement occurs. This is supported by inspection of the simple images shown in Figure 39 and resulting intensity of segregation shown in Figure 40. Note that, for a given number of diffusive averages, the intensity of segregation is significantly less if starting from a more rearranged state.

The decay rate is an indication of how quickly diffusion is homogenizing the concentration field. The rate is faster if diffusion begins from a more rearranged state since the number of interfaces is greatly increased. Collisions occurring at higher relative velocity produce greater volumetric rearrangement that is analogous to shaking a can of marbles with greater vigor. The kinetic energy carried by each droplet is viscously dissipated through complex velocity gradients within the liquid volume which help create concentration interfaces for mass diffusion. The length scale of the collision also plays an important role. When shaken at the same rate, a single marble is more likely to sample the entire can volume as compared to the same marble in a much larger can. This difference is captured by the convective timescale of the event. The ratio of actual mixing time to the convective timescale of the collision provides a convenient measure to distinguish the role of convective stirring in mixing. This ratio increased non-linearly with *Re* number from 2.5 for Collision 1 to 13.8 for Collision 3 as shown in Figure 49 and supports the trend of results previously obtained for a different collision geometry (Carroll and Hidrovo 2013).

The other mixing statistic of interest is the average local intensity gradient given by Equation 20. Recall that this statistic is an assessment of the diffusive interfaces available and larger values signify smaller local diffusion length scales and a greater potential for diffusive mixing. In order to compare the three collision cases, the average local gradient given by Equation 20 is modified to a reduced form:

$$\phi = \frac{\Phi_t - \Phi_\infty}{\Phi_0 - \Phi_\infty} \qquad \textbf{50}$$

Reducing the average gradient in this manner shows the number of interfaces that are created relative to the initial and final value. This is valuable information since one of the objectives of this diagnostic technique is to compare collisions at different inertial conditions and collision geometries. Collisions that produce large increases in concentration gradients should also display fast homogenization rates due to the reduced local diffusive length scales. Although the time and length scale at which each operate

are different, convective stirring and diffusion act in concert. Convection acts at the system level to create interfaces while diffusion acts at local level to smear these available interfaces. It is therefore expected that collisions involving short convective timescales will display larger initial changes in the average gradient statistic. Increases may be short lived, however, since a large number of available interfaces will activate diffusion and quickly reduce the statistic.

The time trace for the reduced average gradient given by Equation 50 is shown in Figure 50 for the three collision cases outlined in Table 1. Collisions occurring at higher velocity elicit significantly more dynamic behavior, characterized by repeated increases and decreases in local gradients. This is clear by comparing the benign increase and gradual decrease for Collision 1 to the abrupt increase and subsequent decrease for Collision 2. The initial increase is greatest for Collision 3, which occurred at the highest *Re* number and shortest convective timescale considered. The change in the average gradient was smallest for Collision 1 and implies that the creation of interfaces due to volumetric rearrangement was not as significant compared to collisions occurring at larger *Re* numbers. The response shown by Collision 3 may suggest three dimensional flow field interactions, where fluid originating from outside the out-of-plane direction is brought into and out of focus. Collisions occurring at large *Re* numbers should reveal complex 3D motion as the kinetic energy is dissipated but it is not certain if that is the case for Collision 3. If material is convected into and out of the field of view, the average concentration within the depth of field is not necessarily conserved quantity. Reviewing the average concentration trace for Collision 3 shows a maximum concentration residual of 5%, which occurs during the first millisecond of the collision event. Additional experiments are required to understand this behavior, such as relocating the image plane or using a lower numerical aperture objective and examining the resulting time traces for comparable hydrodynamic conditions.

Visualization remains invaluable for understanding mixing dynamics and resulting statistics. Applying a pseudo color map to the concentration field provides visual

confirmation of mixing progress and identifies dynamics not readily evident using grayscale images alone. The pseudo coloring technique applied here is based not on actual intensity but on the deviation between actual and mean intensity, thereby providing a visual assessment of the mixing residuals. The new pixel intensity based on mixing residual is given by:

$$I' = 1 - \left(I / \mu - 1 \right) \qquad \textbf{51}$$

A custom color-map is then applied that ranges from blue (locally unmixed) to red (locally mixed) and passes through the colors cyan, yellow, and orange. Furthermore, these images help highlight small differences in intensity more effectively than gray scale images. The images shown in Figure 51 through Figure 53 correspond to Collision 1 through 3 cases, respectively.

Comparison of the three collisions cases show greater homogenization as the Reynolds number is increased. Collision 3 is significantly redder than the other cases and supports the steady-state values for the standard deviations given in Figure 47. The images for the Collision 1 case show noticeable persistence of a concentration island located in the upper right portion of the droplet and there is little change in the concentration residuals after 5ms. Collision 2 also shows two distinct islands that are separated by a nearly vertical interface that becomes pinned to the Y-junction apex at 1.5ms. Convective motion for Collision 2 is confined to the right-most island while less mixing little takes place in the lower left portion of the droplet. Unlike to other two cases, Collision 3 shows extensive mixing throughout the droplet volume with no noticeable islands. The most interesting qualitative result that is shared by each collision case is the formation of a concentration "jet" that is released following the collision and is turned by the droplet boundaries. This is evident at 1ms for Collision 1 and 0.5ms for Collision 2. For the faster mixing collision, vortical motion is clearly visible and sustained throughout the mixing event and is responsible for the large average gradient statistic shown in Figure 50. Vortices effectively stir the droplet contents and provide an increased number

of concentration interfaces for diffusion to act leading to better homogenized droplet contents once the collision dynamics subside.

Table 1. Measured (length, velocity, mixing time) and calculated (Reynolds number, convective time scale) collision parameters for the three mixing events.

Mixing Event	Collision Length (μm)	Collision Velocity (m/s)	Reynolds Number	Convective Time (ms)	Mixing Time (ms)
Collision 1	115 +/- 1	0.06 +/- 0.001	7 +/- 0.7	1.99 +/- 0.04	5.05 +/- 0.85
Collision 2	129 +/- 3	0.24 +/- 0.006	31 +/- 3	0.53 +/- 0.02	4.10 +/- 0.25
Collision 3	89 +/- 11	0.83 +/- 0.10	74 +/- 6	0.11 +/- 0.02	1.50 +/- 0.55

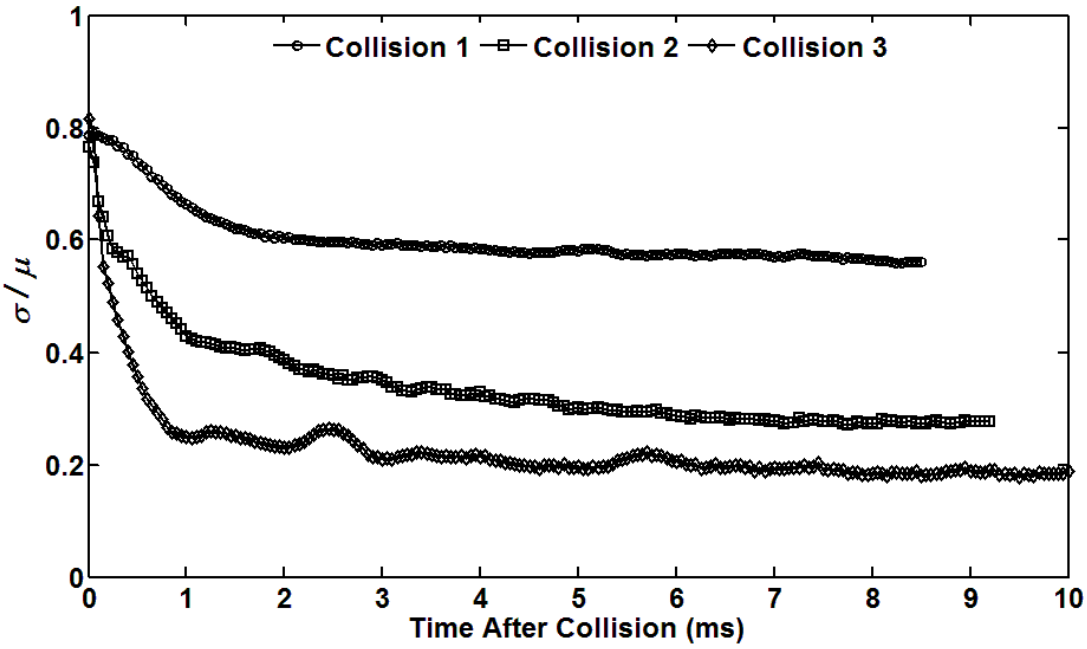

Figure 47. Temporal changes in normalized standard deviation of the intensity field given by Equation 12 for the three collision cases described in Table 1. Time begins at the last frame just prior to droplet collision. The data shows collisions with short convective timescales produce lower standard deviations of the concentration field. A smaller ending standard deviation implies better mixed conditions.

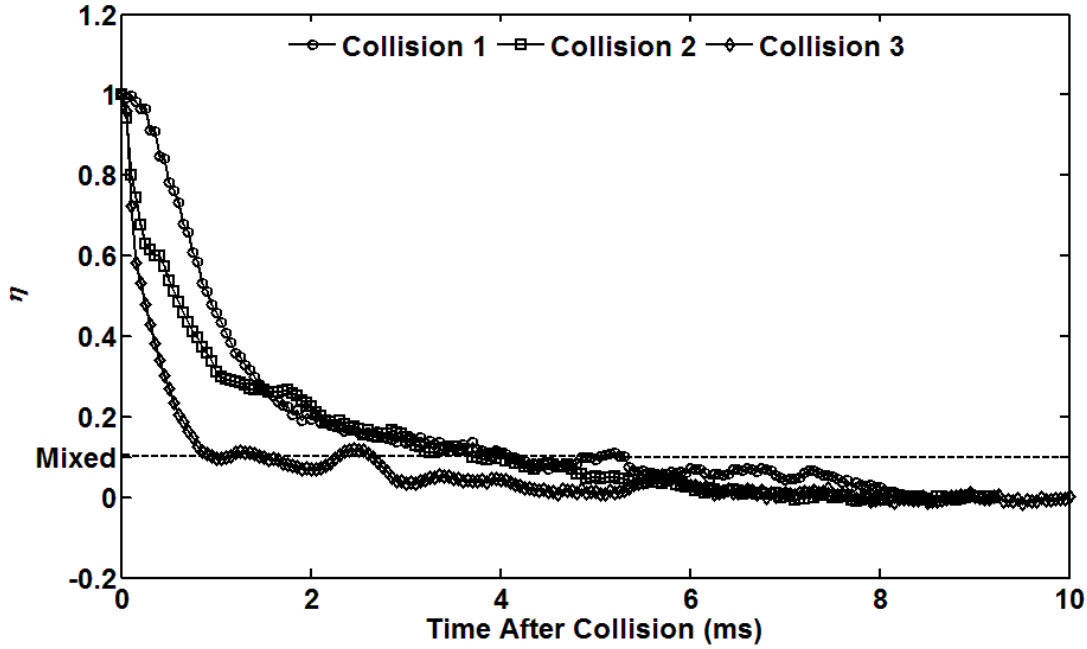

Figure 48. Temporal changes in the mixing parameter η given by Equation 16 for the three collision cases outlined in Table 1. Time begins at the last frame just prior to droplet collision and mixing is assumed complete when the mixing parameter reaches 0.1, as indicated by the dashed line. The data shows that homogenization of the concentration field occurs faster for collisions with shorter convective timescales.

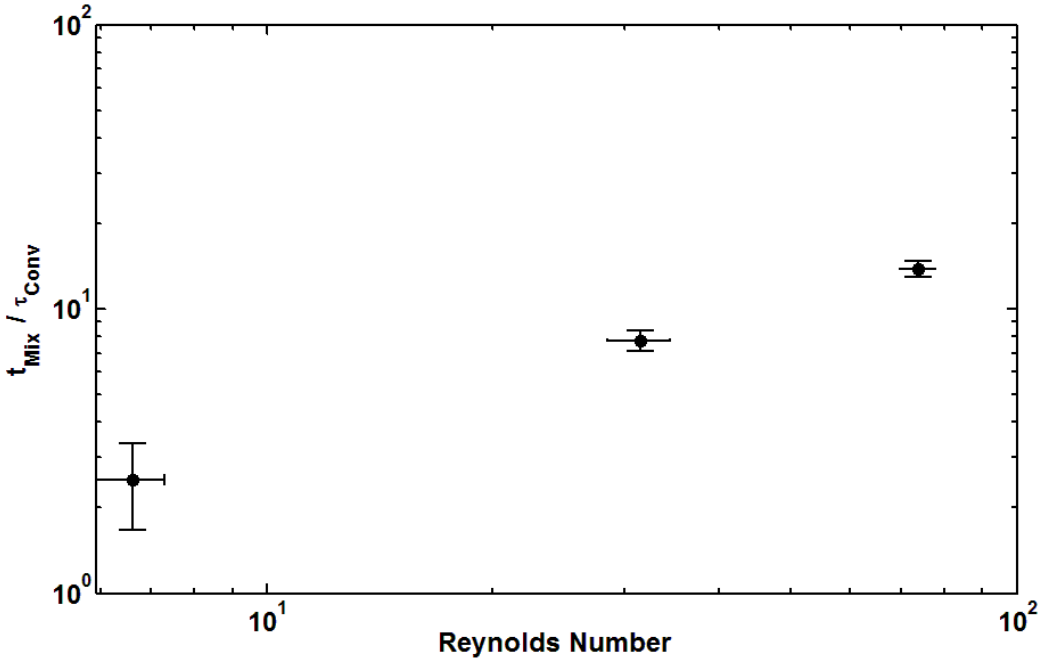

Figure 49. Ratio of actual mixing time to the convective timescale for the three collision cases described in Table 1 versus the Reynolds number for the collision. Error bars are based on the spatial and temporal resolution of each collision case.

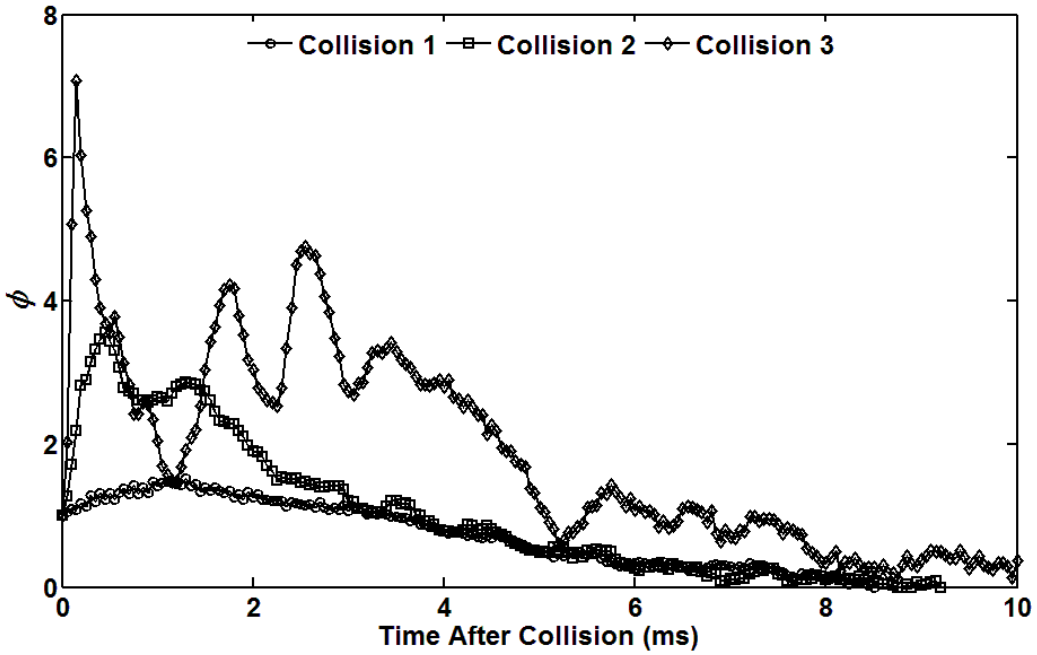

Figure 50. Temporal changes in the reduced average intensity gradient parameter ϕ given by Equation 17. Collisions occuring at higher relative velocity, such as Collision 3, are subject to greater volumetric rearrangement as indicated by the more dynamic time trace – larger gradients are being generated by convection and smeared by diffusion.

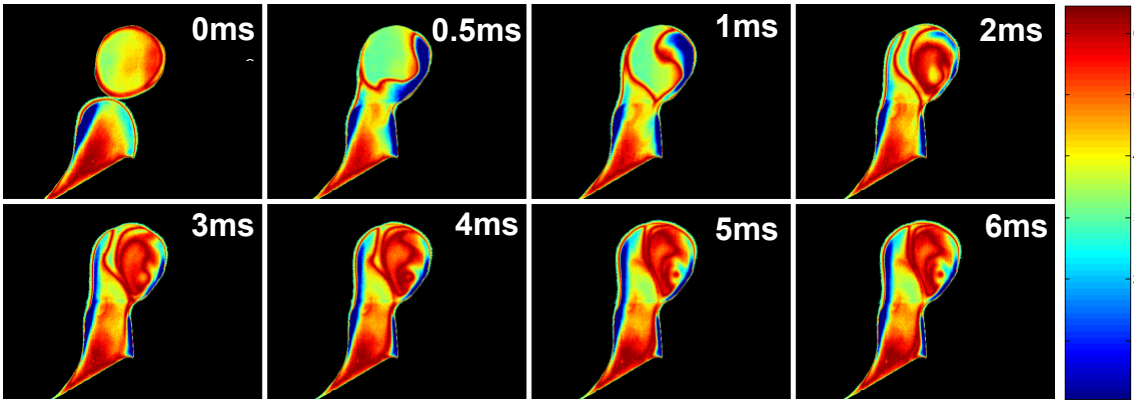

Figure 51. Colored images of the Collision 1 mixing event (Re = 7, τ_{Conv} = 2ms) that have been pseudo-colored based on mixing residuals (difference between actual intensity and intensity when fully mixed) where red indicates locally mixed while blue indicates locally unmixed. Note the presence of islands that are not actively participating in the mixing process. The majority of active mixing takes place along the upper boundaries of the coalesced droplet.

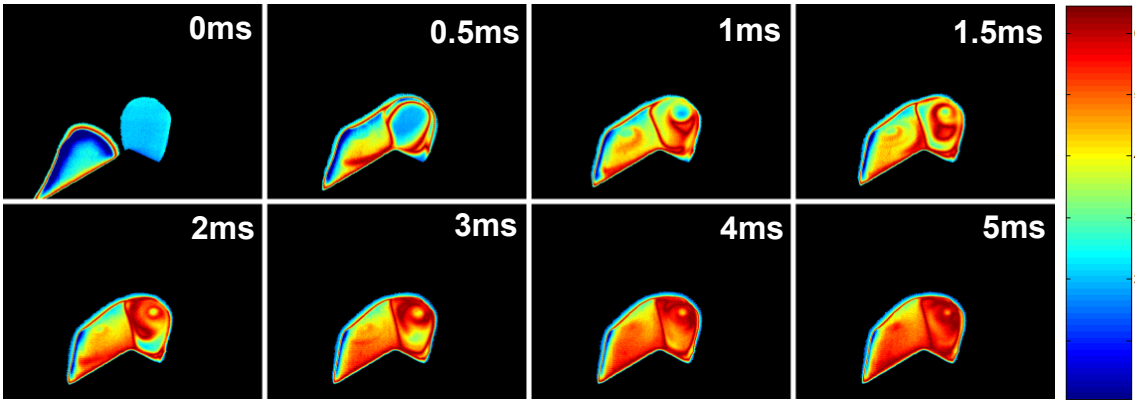

Figure 52. Colored images of the Collision 2 mixing event (*Re* = 31, τ_{Conv} = 0.5ms) that have been pseudo-colored based on mixing residuals (difference between actual intensity and intensity when fully mixed) where red indicates locally mixed while blue indicates locally unmixed. A single vortex develops in the upper right portion of the droplet around 1ms. Although the volume in the immediate vicinity of the vortex is well stirred around 4ms, the left-most region remains largely unmixed.

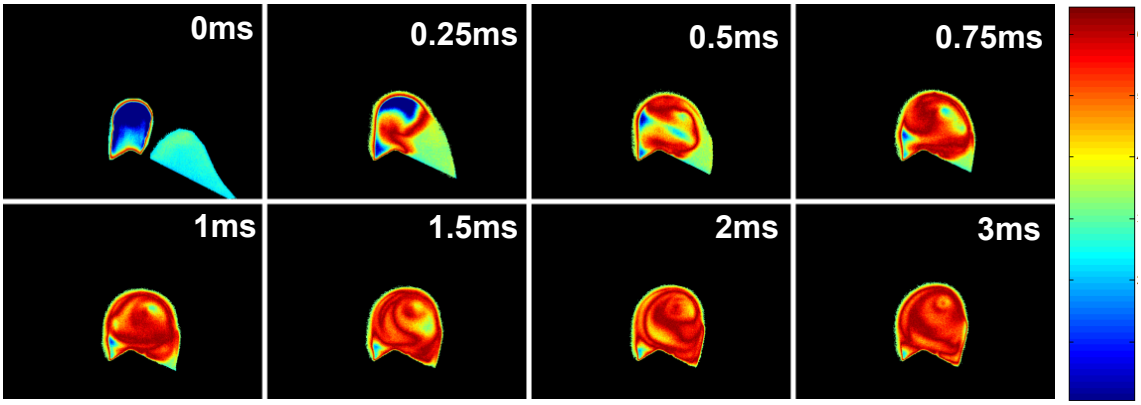

Figure 53. Colored images of the Collision 3 mixing event (*Re* = 74, τ_{Conv} = 0.1ms) that have been pseudo-colored based on mixing residuals (difference between actual intensity and intensity when fully mixed) where red indicates locally mixed while blue indicates locally unmixed. Note the development of a single vortex at the center of the droplet around 1ms that effectively stirs the droplet contents.

5.3 Comparison to Theoretical Model

To gauge the validity of these results, as well as all results to date, comparisons are made with the modeling predictions. The range of collision *Pe* numbers obtained by experiment ranged from $2.5x10^3$ to $3x10^5$ and therefore only convection dominated modeling predictions are used for comparison. The plot in Figure 54 shows the experimental data overlaid with the model prediction. The mixing time has been non-dimensionalized by the mass diffusion timescale and the results indicate a Pe^{-1} relationship. The data is best fit using a λ/L ratio of 0.25, which is significantly smaller than that shown for continuous flow systems using herringbone textured channels (Stroock, et al. 2002). The large range of measured mixing times for a given *Pe* number, especially past 10^5, suggests a trend between the degree of mixedness and the measured mixing time. Collisions that gave longer mixing times for a given *Pe* number resulted in better mixedness. This is confirmed by the pseudo color images that are inset in Figure 54. Collisions above the modeling prediction show little mixing residuals while those below model prediction show areas that remain unmixed. There are also collision parameters that are not captured by the simple model, such as surface tension considerations and asymmetric the boundary interactions. Additional data is needed to populate collision results in the 10^3 to 10^4 *Pe* number ranges to confirm the Pe^{-1} dependence throughout the convection dominated regime.

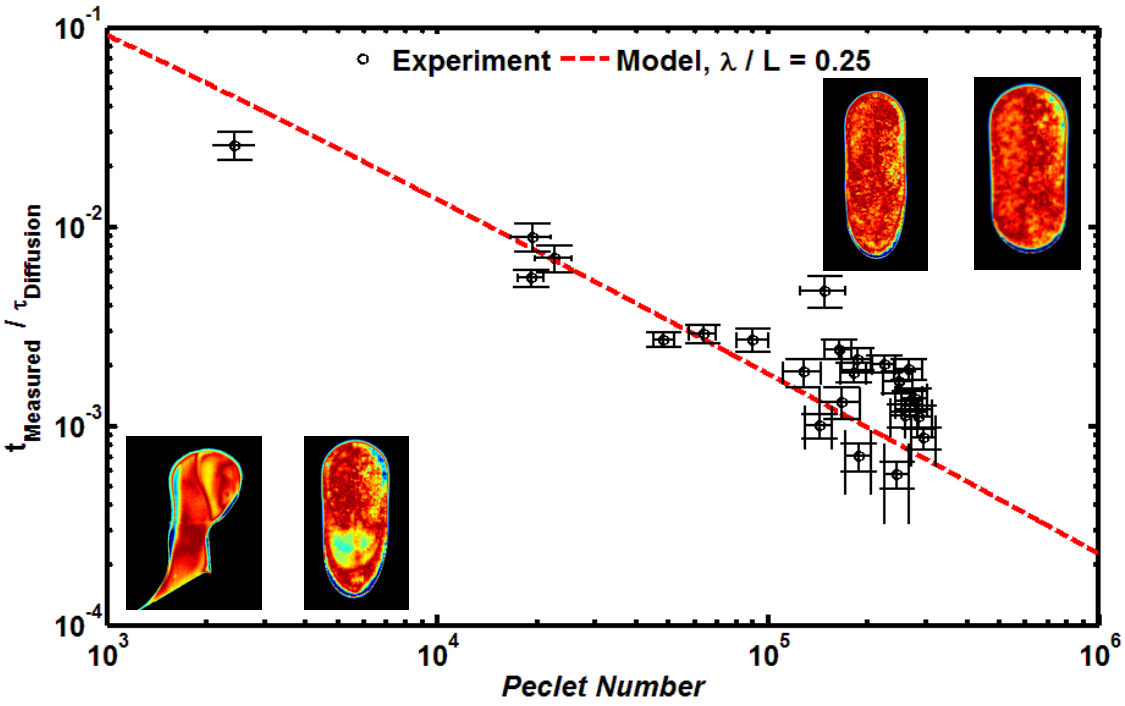

Figure 54. Plot showing experimental droplet mixing data and modeling prediction across the range of *Peclet* numbers considered. Mixing events that are at or below model predictions show poor mixedness as compared to mixing events above the model prediction. The pseudo-color inserts show the mixing residuals for two cases above and below the model prediction.

5.4 Summary of Research Accomplishments

- Collided discrete droplets at speeds near 1m/s in a confined gaseous microflow. Never before have droplet collisions and coalescence at these speeds been recorded and published.
- Visualized and quantified mixing dynamics in confined droplet collisions.
- Droplet mixing results obtained across a decade of *Re* and *Pe* show direct link between the convective timescale of the collision and the resulting mixing time.
- Comparison of experimental and analytical model results show the same trends but the model generally underestimates the mixing time.
- A paper outlining these results has been published in *Heat Transfer Engineering* (Carroll and Hidrovo 2012).

CHAPTER 6

CONCLUSION AND RECOMMENDATIONS

This manuscript focused on three major efforts: generating droplets in a gaseous microflow, colliding and mixing droplets in a gaseous microflow, and developing an optical diagnostic technique capable of quantifying mixing in confined droplet collisions. This work was motivated by the need to mix two droplets rapidly in a microchannel and the inability of existing mixing methodologies at meeting this demand. Although largely application driven, the mixing dynamics that result from a controlled droplet collision are of fundamental importance. Rapid mixing is the primary technique for understanding the mechanism and quantifying the rate constant for chemical reactions. Some of the most interesting and telling reactions occur with reaction rates greater than 10^3 s^{-1} and necessitates sub-millisecond mixing times. This work has shown that a micromixer based on inertial droplet collision provides millisecond mixing times for nano-liter sized droplets, an accomplishment that to date has only been achieved for droplets volumes two orders of magnitude less.

Prerequisite to orchestrating droplets collisions is the ability to generate droplets of predictable size and frequency using a gaseous microflow. Experimental data on two-phase gas-liquid droplet generation is surprisingly deficient, possibly due to the difficulty in discretizing liquids into controllable volumes in the presence of a high *Reynolds* number gas flow. This work has demonstrated mono-dispersed droplet generation using gas *Reynolds* numbers in excess of 200. The key feature leading to this success is the gas and liquid flow stability provided by a newly developed microfluidic test bench. The experimental setup has provided characterization of detached droplet aspect ratios across a decade of gas *Reynolds* numbers and different channel aspect ratios. Data analysis identified a transition from pressure dominated detachment to inertial detachment near a gas *Reynolds* number of 100. The result is that droplets generated under inertial

conditions are smaller and of nearly uniform aspect ratio as opposed to the elongated slugs produced when pressure forces dominate.

Quantify mixing in microchannel droplet flows is a formidable task. The difficulty is compounded further when highly dynamic events such as droplet collisions are investigated. The inability of existing measurement techniques at fulfilling this need stimulated development of a diagnostic framework that combines wide-field microscopy, laser-induced fluorescence, high speed image acquisition, and unique image processing operations that provide a meaningful statistical interpretation of the mixing process. Two governing statistics are proposed that separate the inherently simultaneous action of mass diffusion and convective rearrangement following a collision.

The diagnostic technique was used to measure droplet collision mixing times across a decade of *Reynolds* and *Peclet* numbers. Results identified a direct link between the mixing and convective timescales that, when non-dimensionalized by the mass diffusion timescale, gives an inverse *Peclet* number relationship. The implications of these results are that doubling the collision velocity reduces the mixing time by a factor of two. Likewise, reductions in droplet size yield similar behavior. Combining these results with the characteristics of inertial droplet generation identifies a synergy between creating, colliding, and mixing droplets in a gaseous microflow.

There are still many questions unanswered and issues unresolved. The most critical of which are the three dimensional effects of mixing that are not revealed using a two dimensional slice of the mixing volume. Care was taken to position the field of view near the center of the microchannel for each experiment. It is not clear how imaging at depths not along the centerline will influence the intensity of segregation and scale of segregation results. Mixing near the channel boundaries will likely show reduced mixedness as compared to regions near the center of the droplet. It remains unclear if mixing results follow the same trend when imaged off the droplet center. There are also issues of non-uniform intensity distributions that are not removed during image processing operations. These include intensity variations due to attenuation at droplet

boundaries and spatial non-uniformities due to the laser excitation source. Although efforts were made to reduce these disturbances using image processing techniques, their effect on the resulting statistics cannot be discredited. Ratiometric techniques offered by dual-fluorescence diagnostic systems may strongly mitigate these effects. The trade-off that must be considered are reduced field of view, shorter imaging durations, and significantly more complex spectral filtering operations. Lastly, the exact limitations of droplet collision mixing remain uncertain. Collision velocities near 1m/s have occurred without subsequent breakup and suggest that further increases in collision velocity are achievable while still ensuring coalescence. A collision velocity of 10m/s will reduce mixing time to 500μs and provide the sub-millisecond mixing required by the next generation microfluidic devices.

REFERENCES

Anderson P, Bath A, Groger W, Lulf HW, Meijer G, Meulen JJt (1998) Laser-Induced Fluorescence with Tunable Excimer Lasers as a Possible Method for Instantaneous Temperature Field Measurements at High Pressures: Checks with Atmospheric Flame. Applied Optics 27:365-378

Anna SL, Bontoux N, Stone HA (2003) Formation of dispersions using ``flow focusing'' in microchannels. Applied Physics Letters 82:364-366

Anna SL, Mayer HC (2006) Microscale Tipstreaming in a Microfluidic Flow Focusing Device. Physics of Fluids 18

Arbeloa FL, Arbeloa TL, Arbeloa IL, Moreno IG, Costela A, Sastre R, Amat-Guerri F (1998) Photophysical and Lasing Properties of Pyrromethene 567 Dye in Liquid Solution. Chemical Physics 236:331-341

Arbeloa FL, Banuelos J, Martinez V, Arbeloa T, Arbeloa IL (2005) Structural, Photophysical and Lasing Properties of Pyrromethene Dyes. International Reviews in Physical Chemistry 24:339-374

Aref H (1984) Stirring by Chaotic Advection. Journal of Fluid Mechanics 143:1-21 DOI 10.1017/S0022112084001233

Aris R (1956) On the dispersion of a solute in a fluid flowing through a tube. Proceedings of the Royal Society of London Series A Mathematical and Physical Sciences 235:67-77

Bellerose JA, Rogers CB (1994) Measuring Mixing and Local pH Through Laser Induced Fluorescence. Laser Anemometry 191:217-220

Bogy DB (1979) Drop Formation in a Circular Liquid Jet. Ann Re Fluid Mech 11:207-228

Borlinghaus R (2011) The White Confocal: Continuous Spectral Tuning in Excitation and Emission. In: Optical Fluorescence Microscopy. (ed Diaspro, A), pp. 37-54, New York: Springer

Brouzes E, Medkova M, Savenelli N, Marran D, Twardowski M, Hutchison JB, Rothberg JM, Link DR, Perrimon N, Samuels ML (2009) Droplet microfluidic technology for single-cell high-throughput screening. Proceedings of the National Academy of Sciences 106:14195-14200 DOI 10.1073/pnas.0903542106

Bui A, Zhu Y (Year) Numerical Study of Droplet Generation in a Complex Micro-Channel. In: 16th Australasian Fluid Mechanics Conference, Gold Coast, Australia, December 2-7, 2007

Carroll B, Hidrovo C (2012) Experimental Investigation of Inertial Mixing in Colliding Droplets. Heat Transfer Engineering DOI 10.1080/01457632.2013.703087

Carroll B, Hidrovo C (2013) Experimental Investigation of Inertial Mixing in Colliding Droplets Heat Transfer Engineering 34

Christopher G, Anna S (2007) Microfluidic Methods for Generating Continous Droplet Streams. Journal of Physics D: Applied Physics 40:319-336

Coppeta J, Rogers C (1998) Dual Emission Laser Induced Fluorescence for Direct Planar Scalar Behavior Measurements. Experiments in Fluids 25:1-15 DOI 10.1007/s003480050202

Coppeta J, Rogers C, Philipossian A, Kaufman FB (1996) Characterizing Slurry Flow During CMP Using Laser Induced Fluorescence. In: Workshop on Chemical Mechanical Polishing, Lake Placid, NY

David M, Fogg D, Hidrovo C, Flynn R, Goodson K (2006) Development and Calibration of a Two-Dye Fluorescence System for Use in Two-Phase Micro Flow Thermometry.

Dimotakis PE (2005) Turbulent Mixing. Annual Review of Fluid Mechanics 37:329-356 DOI 10.1146/annurev.fluid.36.050802.122015

Dimotakis PE, Miake-Lye RC, Papantoniou DA (1983) Structure and dynamics of round turbulent jets. Physics of Fluids 26:3185-3192

Dutta P, Chevray R (1994) Inertial Effects in Chaotic Mixing with Diffusion. J Fluid Mech 285:1-16

Eggers J, Villermaux E (2008) Physics of liquid jets. Reports on Progress in Physics 71:036601

Exciton (2011)

Faes M, Glasmacher B (2010) Anlaysis of Macro and Micromixing in Laminar Stirred Mixing Vessels Using Laser Optical and Numerical Methods. In: Macro and Micro Mixing: Analysis, Simulation and Numerical Calculation. eds Bockhorn, H, Peukert, W, Mewes, D and Warnecke, HJ), pp. 55-67: Springer

Ganan-Calvo AM (1998) Generation of Steady Liquid Microthreads and Micron-Sized Monodisperse Sprays in Gas Streams. Physical Review Letters 80:285-288

Ganan-Calvo AM (2008) Unconditional jetting. Physical Review E 78:026304

Ganan-Calvo AM, Barrero A (1999) A novel pneumatic technique to generate steady capillary microjets. Journal of Aerosol Science 30:117-125

Garstecki P, Fuerstman MJ, Stone HA, Whitesides GM (2006) Formation of droplets and bubbles in a microfluidic T-junction-scaling and mechanism of break-up. Lab Chip 6:437-446 DOI 10.1039/b510841a

Graaf Avd, Steegmans M, Sman Rvd, Schroen C, Boom R (2005) Droplet Formation in a T-Shaped Microchannel Junction: A Model System for Membrane Emulsification. Colloids and Surfaces A: Physiochemical Engineering Aspects 266:106-116

Graaf Svd, Nisisako T, Schroen C, Sman Rvd, Boom R (2006) Lattice Boltzmann Simulations of Droplet Formation in a T-Shaped Microchannel. Langmuir 22:4144-4152

Gradl J, Peukert W (2010) Characterization of Micro Mixing for Precipitation of Nanoparticles in a T-Mixer. In: Macro and Micro Mixing: Analysis, Simulation and Numerical Calculation. eds Bockhorn, H, Peukert, W, Mewes, D and Warnecke, HJ): Springer

Herrada MA, Ga, ntilde, aacute, n-Calvo AM, Ojeda-Monge A, Bluth B, Riesco-Chueca P (2008) Liquid flow focused by a gas: Jetting, dripping, and recirculation. Physical Review E 78:036323

Hertzog DE, Michalet X, Jager M, Kong X, Santiago JG, Weiss S, Bakajin O (2004) Femtomole Mixer for Microsecond Kinetic Studies of Protein Folding. Anal Chem 76:7169-7178 DOI 10.1021/ac048661s

Hidrovo CH, Hart DP (2001) Emission Reabsorption Laser Induced Fluorescence (ERLIF) Film Thickness Measurement. Measurement Science & Technology 12:467-477

Hidrovo CH, Wang FM, Steinbrenner JE, Lee ES, Vigneron S, Cheng CH, Eaton JK, Goodson KE, Asme (2005) Water slug detachment in two-phase hydrophobic microchannel flows.

Hiller B, Hanson RK (1988) Simultaneous Planar Measurements of Velocity and Pressure Fields in Fas Flows Using Laser-Induced Fluorescence. Appl Opt 27:33-48

Jacobs B, Gekelman W, Pribyl P, Barnes M, Kilgore M (2007) Laser-Induced Fluorescence Measurements in an Inductively Coupled Plasma Reactor. Applied Physics Letters 91:161505-161503

Jendrzok B, Pauls C, Kob HJ, Lucas K (2010) Time-Resolved Measurement of Concentrations in Mixing Processes Using Raman Spectroscopy. In: Micro and Macro Mixing: Analysis, Simulation and Numerical Calculation. eds Bockhorn, H, Peukert, W, Mewes, D and Warnecke, HJ), pp. 39-53: Springer

Jeong W-C, Lim J-M, Choi J-H, Kim JH, Lee Y-J, Kim S-H, Lee G, Kim J-D, Yi G-R, Yang S-M Controlled Generation of Submicron Emulsion Droplets via Highly Stable Tip-streaming Mode in Microfluidic Devices. Lab on a Chip

Jones SW, Thomas OM, Aref H (1989) Chaotic advection by laminar flow in a twisted pipe. Journal of Fluid Mechanics 209:335-357 DOI doi:10.1017/S0022112089003137

Jose B, Cubaud T (2012) Droplet arrangement and coalescence in diverging/converging microchannels. Microfluidics and Nanofluidics 12:687-696 DOI 10.1007/s10404-011-0909-z

Kinsey JL (1977) Laser-Induced Fluorescence. Ann Rev Phys Chem 28:349-372

Kling K, Mewes D (2010) Measurements of Macro and Micro-scale Mixing by Two-Color Laser Induced Fluorescence. In: Macro and Micro Mixing: Analysis, Simulation and Numerical Calculation. eds Bockhorn, H, Peukert, W, Mewes, D and Warnecke, HJ), pp. 55-67: Springer

Knight JB, Vishwanath A, Brody JP, Austin RH (1998) Hydrodynamic Focusing on a Silicon Chip: Mixing Nanoliters in Microseconds. Physical Review Letters 80:3863-3866

Koochesfahani MM, Dimotakis PE (1986) Mixing and Chemical Reactions in a Turbulent Liquid Mixing Layer. Journal of Fluid Mechanics 170:83-112 DOI 10.1017/S0022112086000812

Lavieille P, Lemoine F, Lavergne G, Lebouché M (2001) Evaporating and Combusting Droplet Temperature Measurements Using Two-Color Laser-Induced Fluorescence. Experiments in Fluids 31:45-55 DOI 10.1007/s003480000257

Lefebvre AH (1989) Atomization and Sprays. Hemisphere Publishing,

Lefebvre AH, Chin J (Year) Some Comments on the Characterization of Drop-Size Distributions in Sprays. In: Proc 3rd Int Conf Liquid Atomisation ans Spray Systems, London, England

Link DR, Anna SL, Weitz DA, Stone HA (2004) Geometrically Mediated Breakup of Drops in Microfluidic Devices. Physical Review Letters 92:054503

Liu H, Zhang Y (2009) Droplet Formation in a T-Shaped Microfluidic Junction. Journal of Applied Physics 106

Liu Z, Huang Y, Jin Y, Cheng Y (2010) Mixing Intensification by Chaotic Advection Inside Droplets for Controlled Nanoparticle Preparation. Microfluidics and Nanofluidics 9:773-786 DOI 10.1007/s10404-010-0593-4

MacDonald RI (1990) Characteristics of Self-Quenching of the Fluorescence of Lipid-Conjugated Rhodamine in Membranes. Journal of Biological Chemistry 265:13533-13539

Mao X, Juluri B, Lapsley M, Stratton Z, Huang T (2010) Milliseconds Microfluidic Chaotic Bubble Mixer. Microfluidics and Nanofluidics 8:139-144 DOI 10.1007/s10404-009-0496-4

Masca SI, Rodriguez-Mendieta IR, Friel CT, Radford SE, Smith DA (2006) Detailed Evaluation of the Performance of Microfluidic T Mixers Using Fluorescence and Ultraviolet Resonance Raman Spectroscopy. Review of Scientific Instruments 77:055105-055105-055109

Matsumoto K, Fujii T, Suzuki K, Segawa D, Kadota T (1999) Laser Induced Fluorecence for the Non-Intrusive Diagnostics of a Fuel Droplet Buring Under Microgravity in a Drop Shaft. Measurement Science and Technology 10:853-858

Nguyen N-T (2008) Micromixers Fundamentals, Design and Fabrication. William Andrew Inc., Norwich

Nilsson MA, Rothstein JP (2012) The effect of contact angle hysteresis on droplet coalescence and mixing. Journal of Colloid and Interface Science 363:646-654

Ottino J (1989) The Kinematics of Mixing: Stretching, Chaos, and Transport. Cambridge University Press, Cambridge, England

Ottino JM (1990) Mixing, Chaotic Advection, and Turbulence. Annual Review of Fluid Mechanics 22:207-253

Ottino JM (1994) Mixing and Chemical Reactions a Tutorial. Chemical Engineering Science 49:4005-4027

Ottino JM, Wiggins S (2004) Introduction: Mixing in Microfluidics. Philos Trans R Soc London, A 362:923-935

Park HY, Kim SA, Korlach J, Rhoades E, Kwok LW, Zipfel WR, Waxham MN, Webb WW, Pollack L (2007) Conformational Changes of Calmodulin Upon Ca2+ Binding Studied with a Microfluidic Mixer. Proc Nat Acad of Science USA 105:542-547

Paul EL, Atiemo-Obeng VA, Kresta SM (2004) Handbook of Industrial Mixing - Science and Practice: John Wiley & Sons, Inc

Piorek BD, Lee SJ, Santiago JG, Moskovits M, Banerjee S, Meinhart CD Free-surface microfluidic control of surface-enhanced Raman spectroscopy for the optimized detection of airborne molecules. Proc Natl Acad Sci U S A 2007 Nov 27;104(48):18898-901 Epub 2007 Nov 19

Plateau J (1873) Experimental and Theoretical Statistics of Liquids Subject to Molecular Forces Only.

Quercioli F (2011) Fundamentals of Optical Microscopy. In: Optical Fluorescence Microscopy. (ed Diaspro, A), pp. 1-36, New York: Springer

Rayleigh L (1878) On the Instability of Jets. Proc Longon Math Soc 10

Rayleigh L (1879) On the Capillary Phenomena of Jets. Proceeding of the Royal Society of London 29:71-97

Rizkalla AA, Lefebvre AH (1975) The Influence of Air and Liquid Properties on Airblast Atomization. Journal of Fluids Engineering 97:316-320

Robinson T, Manning HB, Dunsby C, Neil MAA, Baldwin GS, deMello AJ, French PM (2010) Investigating Fast Enzyme-DNA Kinetics Using Multidimensional Fluorescence Imaging and Microfluidics. In: Proc SPIE, San Francisco, CA

Savart F (1833) Ann Chim Phys 54:54-87

Schrader B, Hoffmann A, Keller S (1991) Near-Infrared Fourier Transform Raman Spectroscopy: Facing Absorption and Background. Spectrochimica Acta Part A: Molecular Spectroscopy 47:1135-1148

Shah M, Thangaraj K, Soong M-L, Wolford LT, Boyer JH, Politzer IR, Pavlopoulos TG (1990) Pyrromethene–BF2 Complexes as Laser Dyes. Heteroatom Chemistry 1:389-399 DOI 10.1002/hc.520010507

Simonnet C, Groisman A (2005) Chaotic Mixing in a Steady Flow in a Microchannel. Physical Review Letters 94

Simpson SF, Kincaid JR, Holler FJ (1983) Microdroplet Mixing for Rapid Reaction Kinetics with Raman Spectrometric Detection. Analytical Chemistry 55:1420-1422 DOI 10.1021/ac00259a054

Simpson SF, Kincaid JR, Holler FJ (1986) Development of a Microdroplet Mixing Technique for the Study of Rapid Reactions by Raman Spectroscopy. Analytical Chemistry 58:3163-3166 DOI 10.1021/ac00127a054

Song H, Bringer MR, Tice JD, Gerdts CJ, Ismagilov RF (2003) Experimental Test of Scaling of Mixing by Chaotic Advection in Droplets Moving Through Microfluidic Channels. Appl Phys Lett 83:4664-4666 DOI 10.1063/1.1630378

Song H, Chen DL, Ismagilov RF (2006) Reactions in Droplets in Microfluidic Channels. Angewandte Chemie International Edition 45:7336-7356 DOI 10.1002/anie.200601554

Song H, Ismagilov RF (2003) Millisecond Kinetics on a Microfluidic Chip Using Nanoliters of Reagents. J Am Chem Soc 125:14613-14619 DOI 10.1021/ja0354566

Stone HA, Leal LG (1990) The effects of surfactants on drop deformation and breakup. Journal of Fluid Mechanics 220:161-186 DOI doi:10.1017/S0022112090003226

Stroock AD, Dertinger SK, Ajdari A, Mezic I, Stone HA, Whitesides GM (2002) Chaotic Mixer for Microchannels. Science 295:647-651 DOI 10.1126/science.1066238

295/5555/647 [pii]

Takahashi S, Ching Y, Wang J, Rouseau DL (1995) Microsecond Generation of Oxygen-bound Cytochrome c Oxidase by Rapid Solution Mixing. The Journal of Biological Chemistry 270:8405-8407

Taylor G (1953) Dispersion of Soluble Matter in Solvent Flowing Slowly through a Tube. Proceedings of the Royal Society of London Series A Mathematical and Physical Sciences 219:186-203 DOI 10.1098/rspa.1953.0139

Tice JD, H. Song, et al. (2003) Formation of Droplets and Mixing in Multiphase Microfluidics at Low Values of the Reynolds and the Capillary Numbers. Langmuir 19:9127-9133

Tuckerman DB, Pease RFW (1981) High-performance heat sinking for VLSI. Electron Device Letters, IEEE 2:126-129

Wang J, Feng L, Ottino JM, Lueptow R (2008) Inertial Effects on Chaotic Advection and Mixing in a 2D Cavity Flow. Industrial & Engineering Chemistry Research 48:2436-2442 DOI 10.1021/ie800404d

Ware WR (1962) Oxygen Quenching of Fluorescence in Solution: An Experimental Study of the Diffusion Process. The Journal of Physical Chemistry 66:455-458 DOI 10.1021/j100809a020

Xia H, Wan S, Shu C, Chew Y (2005) Chaotic Micromixers Using Two-Layer Crossing Channels to Exhibit Fast Mixing at Low Reynolds Numbers. Lab on a Chip 5:748-755

Xiang Y, LaVan D (2009) Droplet Formation at Microfluidic T-junctions. Mater Res Soc Symp Proc 1139

Yariv E, Reisfeld R (1999) Laser Properties of Pyrromethene Dyes in Sol-Gel Glasses. Optical Materials 13:49-54

Zhang Z, Zhao P, Xiao G (2008) Focused-Enhanced Mixing in Microfluidic Channels. Biomicrofluidics 2:014101-014109